

Detailed records of Brunhes/Matuyama
geomagnetic polarity reversal

by Hirokuni ODA

A doctoral dissertation
submitted to Kyoto University

1994

Acknowledgments

I greatly appreciate Prof. Susumu Nishimura, Dr. Takahiro Tagami, Dr. Naoto Ishikawa, Dr. Akira Hayashida and Dr. Yoshitsugu Furukawa for their encouragements and critical comments on the study. I am grateful to Zongyang Liu, Haider Zaman, Koji Fukuma, Hisashi Suzuki, Hironao Shinjoe and other colleagues at Department of Geology and Mineralogy, Kyoto University for their discussions and other supports. Ulrike Körner devotedly helped me with the measurement of sensor response curves during the cruise of ODP Leg 139. Drs. Cathrine Constable and Robert Parker very kindly sent me their deconvolution program and was very helpful to my programming of deconvolution. I would like to express my hearty thanks to Dr. Hidetoshi Shibuya for his encouragements, discussions, supplies of pass-through data and samples of ODP Leg 124, and especially initial motivation to this study. I really appreciate Dr. Masayuki Torii for his continuous encouragements, critical comments and reviews of the manuscript. I extend special thanks to Noriko Hasebe for helping me with the preparation of the final manuscript.

The sample was supplied with the permission of the Ocean Drilling Program. This study was supported by the Grant-in-Aid for Specially Promoted Research No. 04216105 and the Grant-in-Aid for JSPS Fellows No. 1107 from Ministry of Education, Science, and Culture of Japan.

Abstract

High quality and high resolution record of Brunhes/Matuyama polarity transition was obtained from deep-sea sediments of ODP Leg 124 drilled in the Celebes and Sulu Seas. It has been shown recently that the transition records of young geomagnetic reversal from sediments show preferred longitudinal bands of VGP over the Americas and its antipode. The similarity in the distributions of preferred bands and physical properties in the lower mantle led to the speculation of lower mantle control on the VGP paths during geomagnetic reversals. However, due to non-uniform site distribution, the possibility that these bands are explained by preference of the site and VGP distribution $\pm 90^\circ$ away from the site can not be ruled out. There is another report that VGPs of transitional records from volcanic rocks of recent reversals make clusters over western Australia and southern part of South America. This idea is also challenged by compilation of large amount of transitional records from volcanic rocks.

A detailed description of a full polarity reversal is strongly required to solve these problems. Advanced piston core (APC) samples with high magnetization intensity and high sedimentation rate were recovered from ODP Leg 124. Pass-through measurements were conducted at intervals of 5 mm on APC samples across the Brunhes/Matuyama polarity transition for Holes 767B, 769A and 769B. Pass-through data need to be deconvolved to get higher spatial resolution and thus higher time resolution records. A new ABIC-minimizing deconvolution for ODP SQUID magnetometer was developed in Part I of this study to enhance the resolution of the magnetometer. The resolution has been shown to be enhanced from 11 cm of original response to 2 cm in maximum. The scheme was shown to be stable and was applied to the pass-through data from ODP Leg 124.

The results from the three holes are in good agreement, especially between two Holes of Site 769, 769A and 769B, which are about 100 m apart. VGP shows eastward swing to north Atlantic just after the equator crossing. Relatively stable intermediated VGP positions were recognized before and after the transition. The intermediate VGP positions after the reversal persisted for about 2000-3000 yr. These intermediate VGPs can be comparative to the sediment record of Brunhes/Matuyama boundary from the Boso Peninsula, Japan. The longitudinal distribution of transitional VGPs support the idea of preference of the site and VGP distribution $\pm 90^\circ$ away from the site. The relative intensity was also estimated and 4000 yr interval of low intensity zone across the reversal boundary was recognized.

CONTENTS

Acknowledgments

Abstract

General Introduction	1
Geomagnetic reversals and its relevance	
1. Geodynamo	2
2. Solar magnetic field	2
3. Core mantle interaction	3
4. Secular variation	4
5. Distribution of VGPs during geomagnetic reversals	4
6. Ocean Drilling Program and this study	5
References	6

Part I : Deconvolution of long-core paleomagnetic data of Ocean Drilling Program by ABIC minimization	10
Abstract	11
1. Introduction	12
2. Formulation	15
2.1. Equation of observation	15
2.2. Bayesian statistics	18
2.3. Akaike's Bayesian Information Criterion (ABIC)	20
2.4. Matrix calculation	22
2.5. Error and resolution	22
3. Applications	25
3.1. Description of measurement system	25
3.2. Synthetic data	25
3.3. Real data	30
3.3.1. Section 769B-7H6	33

3.3.2. Connect adjacent sections	39
4. Discussions	47
4.1. Stability and reliability of deconvolution	47
4.2. How to connect adjacent sections?	47
4.3. Noise source and resolution	48
5. Conclusions	51
References	53

Part II : High resolution paleomagnetic records of Brunhes/Matuyama
polarity transition from ODP Leg 124 (Celebes and Sulu Seas) 55

Abstract	56
1. Introduction	57
1.1 Transitional field study	57
1.2 Evolution of transition field models	58
1.3 Preferred longitudinal bands and clusters of VGP	59
1.4 This study	61
2. Geological setting and Sample descriptions	62
2.1 Celebes Sea (Site 767)	62
2.2. Sulu Sea	66
2.2.1 Site 768	66
2.2.2 Site 769	68
2.3. Core Orientation	71
2.4. Sedimentation rates	74
2.4.1. Revision of Pleistocene geomagnetic polarity timescale	74
2.4.2. Sedimentation rates of Sites 767, 768 and 769	76
3. Measurements	79
3.1. Measurements of archive half samples	79
3.2. Measurements of discrete samples	82
4. Results	83
4.1. Results of deconvolution	83

4.2. Rock magnetism	89
4.3. Paleomagnetic results	92
4.3.1. Hole 767B	98
4.3.2. Holes 769A and 769B	105
4.3.3. Hole 768B	113
5. Discussions	119
5.1. VGP paths of Brunhes/Matuyama polarity transition	119
5.2. Short reversal	125
5.3. Test for the preferred longitudinal bands	127
5.4. Relative intensity	130
6. Conclusions	134
References	135

General Introduction

Geomagnetic reversals and its relevance

1. Geodynamo

One of the last fundamental questions in Earth sciences is how the geomagnetic field is generated and is able to reverse its polarity. The numerical solution of the full nonlinear dynamo problem has so far only been obtained for two highly idealized models having limited geophysical relevance (Glatzmeier, 1984; Zhang and Busse, 1990) and reversing dynamos still seem some way off. However, there is a general agreement that the dynamo equations are sufficiently nonlinear to allow reversing solutions and that simple analogue equations, such as those of the coupled disk dynamo of Rikitake (1958), exhibit spontaneous and apparently random polarity reversals.

2. Solar magnetic field

Ideas on the geodynamo and its reversals are influenced by theories of the solar dynamo. The mechanisms of solar dynamo is better understood than the geodynamo, because the development of the solar magnetograph (Babcock and Babcock, 1955) permitted direct measurement of the weak general poloidal field of the Sun, the solar magnetic field reverses nearly periodically with the sunspot cycle of 11 years (Howard, 1974), and the shortage of the cycle enables us to get enough observational data of reversals with longer term variations (Eddy, 1977). The periodic behavior of the solar sunspots led to oscillatory solutions in terms of a dynamo wave mechanism which reproduces the Maunder "butterfly" diagram of sunspot density plotted against latitude and time (Parker, 1979). Solar field reversal is preceded by expulsion of toroidal flux through the surface with accompanying pairs of sunspots. Pairs of sunspots migrate toward the

equator and build up into a complete field inversion.

The dominance of the toroidal field on the Sun, produced by differential rotation in the solar convection zone, was adopted in early geodynamo models (Elsasser, 1946; Bullard and Gellman, 1954). The importance of sunspots and toroidal field expulsion prompted Cox (1975) and later Gubbins (1987) to associate secular variation similar to flux expulsion with build up to a reversal. The success of dynamo waves in explaining the migration of sunspots led Hagee and Olson (1987) to use them in an interpretation of long-term secular variation.

3. Core mantle interaction

Hide (1967) was first to point out the potential importance of core-mantle interactions for core motions and the geomagnetic field. Three principal mechanisms of coupling have been considered (e.g. Gubbins, 1994): topographic (the effect of bumps on the interface on fluid flow), electromagnetic (the coupling through the magnetic force of electric currents flowing in the mantle), and thermal (the response of core flows to lateral variations in heat transport across the interface). By incorporating core-mantle interaction into the dynamo theory the paleomagnetic observations can be linked with other geophysical data. Large-scale temperature anomalies on the surface impart a similarly large scale to the underlying convection (Zhang and Gubbins, 1993), facilitating numerical computations and making the rapidly rotating regime more accessible. The most compelling evidence for core-mantle interaction comes from the decade variations in the length of the day. This variations can only be explained by exchange of angular momentum between the mantle and core, and there is now quite convincing agreement between the

observed length of day and that calculated from flow of fluid in the core using angular momentum balance (Jackson et al., 1993) and a theory of electromagnetic coupling (Stewart, 1992).

4. Secular variation

Historical records of geomagnetic field appear to show confinement away from the Pacific Ocean with apparent blocking of the westward drift near the west coast of the Americas and vigorous activity in the South Atlantic and Indian Ocean regions (Bloxham and Gubbins, 1985). If the solid mantle controls the dynamics, then inferences from the last 400 years of historical observation will be a guide to longer-term changes and, possibly, to the paleomagnetic record and reversals, because the mantle has remained essentially static for several million years.

Constable (1992) suggested on the basis of the VGPs of volcanic rocks from 65 sampling sites over the past 5 Myr that the VGPs show preferred distribution in longitudes, which is similar to the preference of the VGPs during polarity transitions. Quidelleur et al. (1994) reanalyzed and updated the database, and concluded that the preference of VGP distribution seen in Constable's data can be attributed to the uneven distribution of sites and its far-sided VGP.

5. Distribution of VGPs during geomagnetic reversals

Recently long-lived preferred longitudinal bands of VGP paths of the geomagnetic field during polarity transitions have been focused (Tric et al., 1991; Clement, 1991) in relation with the core-mantle boundary conditions by Laj et al. (1991). Valet et al. (1992) rejected the idea of preferred longitudinal bands by chi-square test on the data base from sediment and volcanic records younger than 12 Ma. It

is pointed out that the preference of VGP longitude can also be explained by the preference of site longitude distribution and VGPs $\pm 90^\circ$ away from the sites.

The clustering of transitional VGPs over western Australia and southern part of South America are also reported on volcanic rock records of recent reversals (Hoffman, 1992; Brown et al., 1994). On the contrary, (Prévot and Camps, 1993) compiled 400 intermediate poles from 121 volcanic records of excursions and reversals less than 16 Ma old, which does not confirm VGP clusters and rejected the idea of lowermost mantle control on the transitional fields.

6. Ocean Drilling Program and this study

For better understanding of the mechanism of geomagnetic reversals, it is quite important to get the reliable and precise records of geomagnetic polarity transition field. The geographical distribution of the recording sites are not uniform and additional sites are strongly required for each polarity transition (e.g. McFadden, 1993). The distribution of volcanic rocks that have recorded geomagnetic polarity reversals is limited to the active hot spot area. Thus, sediments especially from deep-sea basins can be the most powerful recording media of geomagnetic field of polarity transitions.

Ocean Drilling Program (ODP) has extremely high potential for transitional field study in several aspects. First is its world wide operation which ensures the global distribution of the sites. Second is that the magnetic mineral in deep-sea sediment is less altered than sediments from land sections that may suffer from chemical change of interstitial water. Third is that the drilling by advanced hydraulic piston corer (APC) enables us to get deep-sea sediment samples without significant drilling disturbance down to 200 meters below

sea floor. This technique has enabled us to get high resolution records of polarity transition at the sites of high sedimentation rate. Fourth is the continuous paleomagnetic measurement just after the recovery of APC samples by a pass-through type SQUID magnetometer on ship. However, the sensor pick-up coils have wide half width of about 11 cm and the deconvolution scheme that enhances the resolution of the magnetometer has not yet been developed. In this study, a new ABIC minimizing deconvolution for ODP's SQUID magnetometer system is developed and investigated in Part I.

ODP Leg 124 was operated in deep sea basins of Celebes and Sulu Seas. Extremely high resolution paleomagnetic records were obtained, because the sedimentation rate is very high (up to 10 cm/kyr) and the concentration of magnetic mineral is very high due to volcanic activity surrounding the basins (Rangin and Silver, 1990). Pass-through measurements were conducted at intervals of 5 mm on ship for the sediments recording Pleistocene polarity reversals. The pass-through data of Brunhes/Matuyama polarity transition were obtained from Holes 767B, 768B, 769A and 769B. These pass-through data were analyzed by using ABIC-minimizing deconvolution developed in Part I of this study. The results from three Holes 767B, 769A and 769B show good agreement, especially between 769A and 769B. The details of geomagnetic field during the Brunhes/Matuyama polarity transition is discussed in Part II of this study.

The pass-through paleomagnetic data and susceptibility data used for the study were obtained on ODP Leg 124 by ship-board paleomagnetists, Drs. Hidetoshi Shibuya, Dean Merrill and Vindell Hsu. The paleomagnetic cube samples were also taken by them and brought back to Japan by Dr. Hidetoshi Shibuya. He measured six of them and I measured all other samples. I measured the standard response curves

for ODP SQUID system during the cruise of Leg 139 with the help of Ulrike Körner. I developed a Fortran Program of ABIC-minimizing deconvolution for pass-through paleomagnetic data of ODP. I analyzed the pass-through data by using this program and investigated the results of deconvolution combined with the paleomagnetic results of cube samples. Dr. Hidetoshi Shibuya inspired me to make use of ABIC and LDU decomposition in the deconvolution scheme.

References

- Babcock, H. W. and Babcock, H. D. (1955), The Sun's magnetic field 1952-1954, *Astrophys. J.*, **121**, 349-366, 1955.
- Bloxham, J. and D. Gubbins, The secular variation of the Earth's magnetic field, *Nature*, **317**, 777-781, 1985.
- Brown, L., J. Pickens and B. Singer, Matuyama-Brunhes transition recorded in lava flows of the Chilean Andes: Evidence for dipolar fields during reversals, *Geology*, **22**, 299-302, 1994.
- Bullard, E. C. and H. Gellman, Homogeneous dynamos, *Philos. Trans. R. Soc. London*, **A247**, 213-278, 1954.
- Clement, B. M., Geographical distribution of transitional VGPs : evidence for non-zonal equatorial symmetry during the Matuyama-Brunhes geomagnetic reversal, *Earth Planet. Sci. Lett.*, **104**, 48-58, 1991.
- Constable, C., Link between geomagnetic reversal paths and secular variation of the field over the past 5 Myr, *Nature*, **358**, 230-233, 1992.
- Cox, A. V., The frequency of geomagnetic reversals and the symmetry of the nondipole field, *Rev. Geophys.*, **13**, 35-51, 1975.
- Eddy, J. A., The Maunder minimum, *Science*, **192**, 1189-1202, 1976.
- Elsasser, W. M., Induction effects in terrestrial magnetism I, Theory,

- Phys. Rev.*, **69**, 106-116, 1946.
- Glatzmeier, G., Numerical simulations of stellar convective dynamos, I, The model and the method, *J. Comput. Phys.*, **55**, 461-484, 1984.
- Gubbins, D., Mechanism for geomagnetic polarity reversals, *Nature*, **326**, 167-169, 1987.
- Gubbins, D., Geomagnetic polarity reversals: A connection with secular variation and core-mantle interaction, *Reviews of Geophysics*, **32**, 61-83, 1994.
- Hagee, V. L. and P. Olson, Dynamo waves and paleomagnetic secular variation, *Geophys. J. R. Astron. Soc.*, **88**, 139-159, 1987.
- Haward, R., Studies of solar magnetic field, I. The average field strengths, *Solar Phys.*, **38**, 283-299, 1974.
- Hide, R., Motions of the Earth's core and mantle, and variations of the main geomagnetic field, *Science*, **157**, 55-56, 1967.
- Hoffman, K., Dipolar reversal states of the geomagnetic field and core-mantle dynamics, *Nature*, **359**, 789-794, 1992.
- Jackson, A., J. Bloxham and D. Gubbins, Time-dependent flow at the core surface and conservation of angular momentum in the coupled core-mantle system, in *Dynamics of the Earth's deep interior and Earth rotation*, Geophys. Monogr. Ser., **72**, pp. 97-107, ed. al., AGU, Washington, D. C., 1993.
- Laj, C., A. Mazaud, R. Weeks, M. Fuller and E. Herrero-Bervera, Geomagnetic reversal paths, *Nature*, **351**, 447, 1991.
- McFadden, P. L., C. E. Barton and R. T. Merrill, Do virtual geomagnetic pole follow preferred paths during geomagnetic reversals?, *Nature*, **361**, 342-344, 1993.
- Parker, E. N., *Cosmical magnetic fields, their origin and their activity*, Oxford, Clarendon, 1979.
- Prévoit, M. and P. Camps, Absence of preferred longitude sectors for

- poles from volcanic records of geomagnetic reversals, *Nature*, **366**, 53-56, 1993.
- Quidelleur, X., J.-P. Valet, V. Courtillot and G. Hulot, Long-term geometry of the geomagnetic field for the last five million years: An updated secular variation database, *Geophys. Res. Lett.*, **21**, 1639-1642, 1994.
- Rangin, C., E. A. Silver and M. T. von Breyman et al., *Proc. ODP, Init. Repts.*, **124**, 1990.
- Rikitake, T., Oscillations of a system of disk dynamos, *Proc. Cambridge Philos. Soc.*, **54**, 89-105, 1958.
- Stewart, D., Geomagnetic impulses and the electrical conductivity of the lower mantle, Ph. D. Thesis, Leeds Univ., Leeds, England, 1992.
- Tric, E., C. Laj, J.-P. Valet, P. Tucholka, M. Paterne and F. Guichard, The Blake geomagnetic event : transition geometry, dynamical characteristics and geomagnetic significance, *Earth Planet. Sci. Lett.*, **102**, 1-13, 1991.
- Valet, J.-P., P. Tucholka, V. Courtillot and L. Meynadier, Paleomagnetic constraints on the geometry of the geomagnetic field during reversals, *Nature*, **356**, 400-407, 1992.
- Zhang, K. and D. Gubbins, Convection in a rotating spherical fluid shell with an inhomogeneous temperature boundary condition at infinite Prandtl number, *J. Fluid Mech.*, **250**, 209-232, 1993.
- Zhang, K.-K. and F. H. Busse, Generation of magnetic fields by convection in a rotating spherical fluid shell of infinite Prandtl number, *Phys. Earth Planet. Inter.*, **59**, 208-222, 1990.

Part I: Deconvolution of long-core paleomagnetic data of
Ocean Drilling Program by ABIC minimization

Abstract

Deconvolution of long-core paleomagnetic data of Ocean Drilling Program (ODP) was developed based on the Bayesian statistics. The deep-sea sediments drilled by advanced hydraulic piston corer (APC) can be an important source of high quality paleomagnetic data. Pass-through measurements of APC samples by a cryogenic magnetometer on ODP's research vessel enable us to get paleomagnetic records continuously. Because the spacial resolution of pick-up coil is about 11 cm and deconvolution is necessary to enhance the resolution. The off-centered configuration of the measurement produces cross terms between x and z axes. The smoothly changing magnetization was modeled in 3-dimensional space with constraints parametrized by 2-norm of second derivative and was deconvolved as a smoothness constrained least squares method. The optimum smoothness was obtained by minimizing Akaike's Bayesian Information Criterion (ABIC) which is a measure of $-2 \log$ (maximum marginal likelihood).

The deconvolution was applied to the artificially produced pass-through data with a Gaussian noise. The amplitude of noise was estimated properly and the variation of longer half wave length than the critical resolution was restored. The deconvolution was also applied to the real pass-through data from two holes of ODP Leg 124 measured at intervals of 5mm. The deconvolution revealed fluctuations with maximum spacial resolution of about 2 cm. The magnetization of these two holes showed favorable agreement especially in declination across the reversal boundary.

1. Introduction

The Ocean Drilling Program (ODP) has long been using a pass-through cryogenic magnetometer as one of the routine measurements on 1.5 m-long samples at intervals of 10 cm. The ODP's paleomagnetic data obtained for advanced hydraulic piston core (APC) on board Joides Resolution is invaluable, because on-site measurements prevent samples from alteration and large cross section ($\pi \times 3.3 \text{ cm} \times 3.3 \text{ cm} / 2 = 17.1 \text{ cm}^2$) increase the sensitivity of measurements. The measurements at higher spatial resolution of higher sedimentation rate sediments enable us to get detailed records of secular variations, excursions and reversal transitional fields.

The signal picked up by the sensor pick-up coils of the magnetometer at a certain position comes from the magnetizations lying in the broad region of sensitivity of the pick-up coils. In order to obtain real remanent magnetization vectors of a long-core, the output of a pass-through magnetometer needs to be deconvolved. Deconvolution is achieved by an operation in frequency space as a division of the magnetometer output by the sensor response. As the sensor response function is usually smooth bell shaped curve and has low amplitude of higher frequency component, high frequency noise in the output signal can easily be exaggerated. Proper reduction of high frequency noise is necessary to get a meaningful solution of the magnetization.

The first attempt to deconvolve long-core paleomagnetic data was made by Dodson et al. (1974). They measured the magnetic remanence of a 1m-long core sample using the long-core cryogenic magnetometer, and deconvolved the data by low-pass-filtering in frequency space. The appropriate filter characteristics were determined subjectively by visual analysis on display.

Constable and Parker (1991) (C&P) developed an alternative deconvolution scheme using a smoothness-constrained least squares

method for long-core paleomagnetic data. They assumed that the magnetizations changed smoothly and expressed the data, the magnetization and the sensor response in terms of cubic spline functions. The smoothness of the magnetization was measured by a 2-norm of the second derivative, and the degree of smoothness was determined so that the fitting residual equals the observational error. The observational errors were estimated by looking at the root mean square value of measurements beyond the region of influence of the core magnetization. Their deconvolution scheme was quite successful, however, their scheme tends to be unstable by underestimation of the noise level.

Recently, Oda and Shibuya (1994) developed a new ABIC minimizing deconvolution scheme. They applied the scheme on the whole-core remanence data of a U-channel core measured at intervals of 5 mm, and get the magnetization consistent with the magnetization of thin sections measured separately on the same cores. Their deconvolution scheme is based on the smoothness-constrained least squares method and the optimum smoothness was determined by ABIC (A Bayesian Information Criterion; Akaike, 1980) minimization. ABIC minimization is a likelihood maximization on Bayes model, through which prior information of the model can be introduced objectively. ABIC minimization have already been applied successfully to several geophysical problems; tidal analysis (BAYTAP-G; Tamura et al., 1991), estimation of Bouguer reduction density (Murata, 1990), and smoothing paleomagnetic data (Tsunakawa, 1992).

All the formerly developed deconvolution were conducted on each magnetization vector component separately. Pass-through measurement of ODP on archive half samples are inserted in the lower half of the bore hole of the magnetometer. This off-centered configuration results in the appearance of cross term between along-core and direction vertical to the splitting plane. Thus, a new ABIC minimizing deconvolution was developed to treat three vector components simultaneously incorporating the cross

term. The newly developed deconvolution scheme was applied to the pass-through data of ODP Leg 124 measured at 5mm-interval and the synthesized data, and the results were investigated.

2. Formulation

2.1 Equation of observation

We assumed that the magnetization is composed of uniformly magnetized thin slices of constant thickness. Pass-through measurements on ODP's research vessel are conducted on archive-half core samples which were split from 1.5m-long whole-core samples. During paleomagnetic measurements, archive-half cores pass through in the lower half of the bore-hole (Fig. 1a). Due to this configuration, X component of magnetization appears in Z-axis pick-up coil, and Z component in X-axis (Fig. 1b).

Under the condition mentioned above, the equation of observation in a discrete form can be expressed by a matrix equation that connects magnetometer output, response function and magnetization as

$$\mathbf{d} = \mathbf{R}_0 \mathbf{m} + \mathbf{e} \quad (1)$$

Here \mathbf{d} denotes the whole-core remanence data, \mathbf{m} is the magnetization of the sample, \mathbf{R}_0 is a matrix whose columns are composed of the sensor responses, and \mathbf{e} is the noise in the whole-core data. Because the true response function \mathbf{R}_0 can not be known practically, this should be replaced by an empirical response \mathbf{R} . The error of the empirical response can be expressed as $\delta\mathbf{R} = \mathbf{R} - \mathbf{R}_0$ (e.g. Okamoto, 1992), and Eq. (1) can be rewritten as

$$\begin{aligned} \mathbf{d} &= (\mathbf{R} - \delta\mathbf{R})\mathbf{m} + \mathbf{e} \\ &= \mathbf{R}\mathbf{m} + \boldsymbol{\varepsilon}, \end{aligned} \quad (2)$$

where $\boldsymbol{\varepsilon} = -\delta\mathbf{R}\mathbf{m} + \mathbf{e}$ is an equivalent noise. As a result, error in the response function is included in $\boldsymbol{\varepsilon}$ and empirical response can be used in the following equations. This equation can be expressed by X, Y and Z

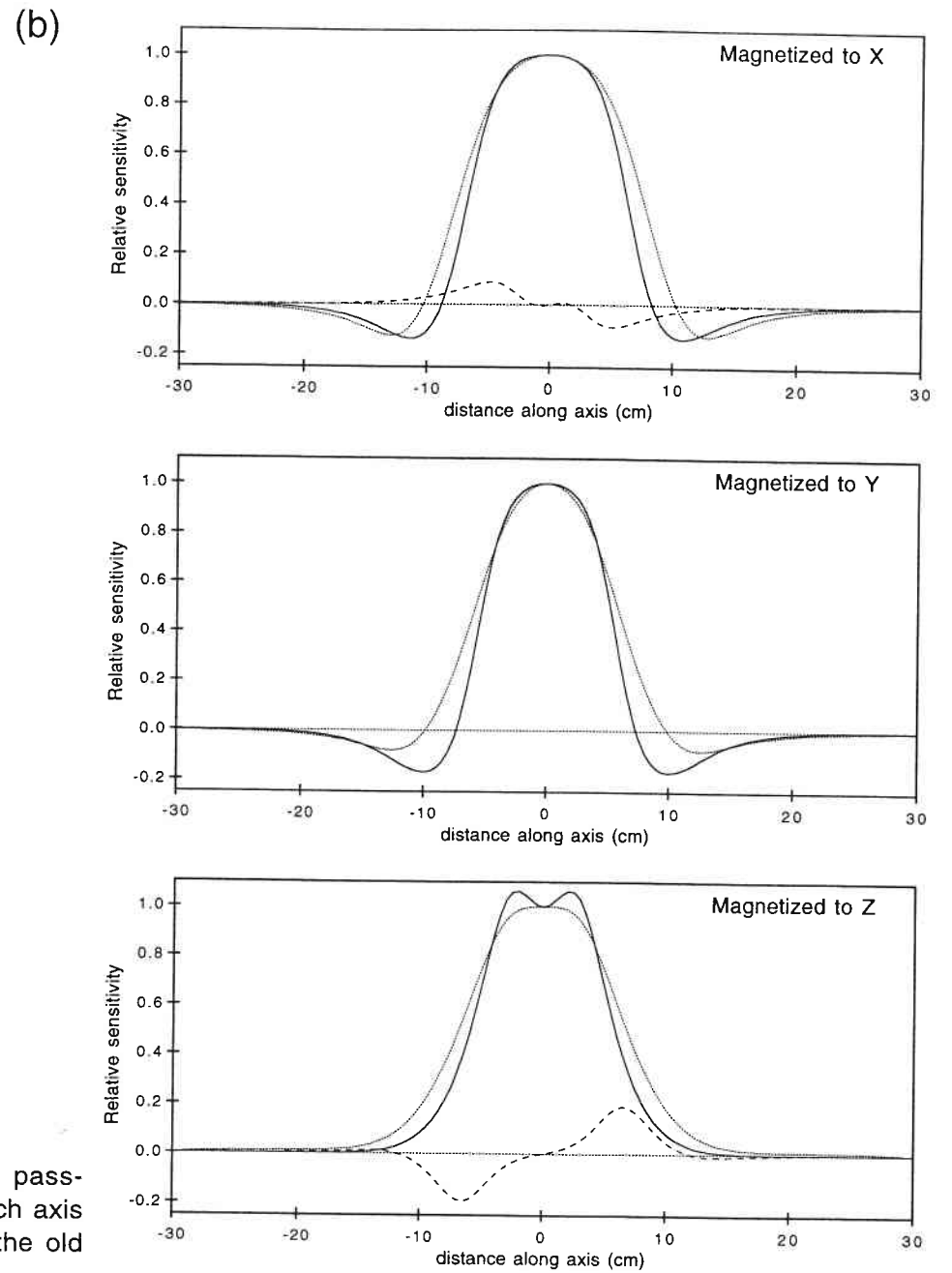
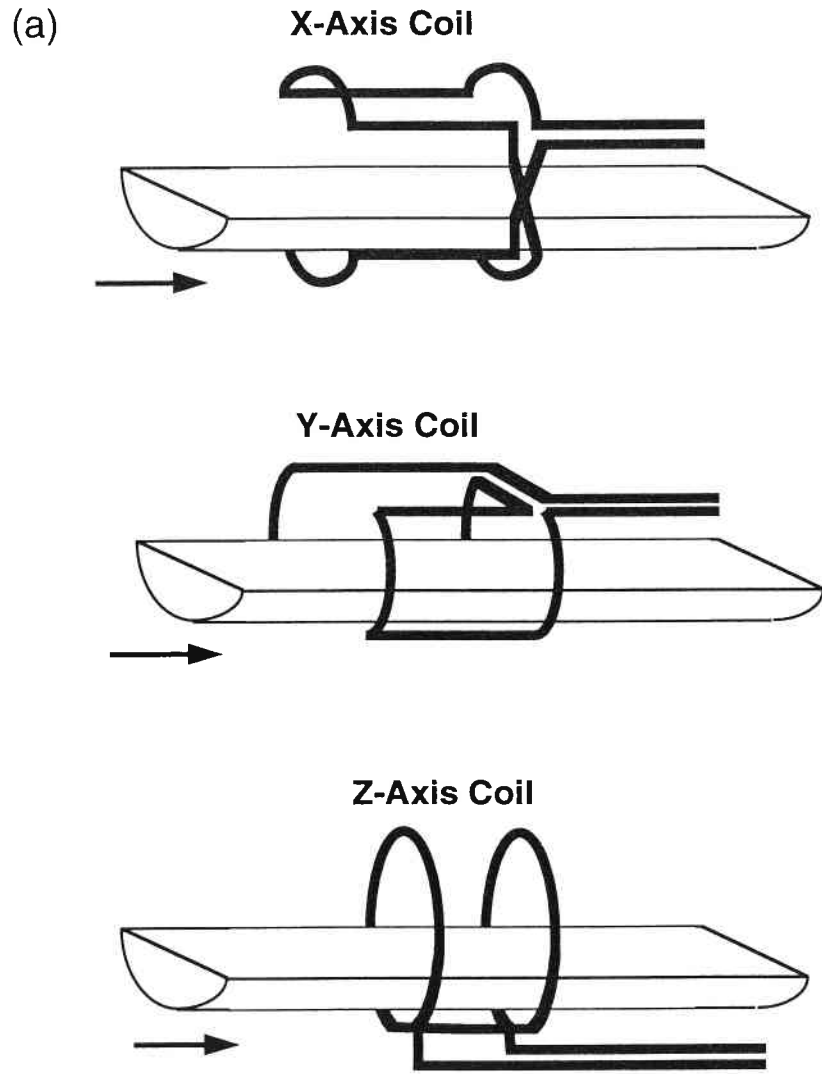


Fig. 1. (a) Configurations of Pick-up coils and archive half sample during pass-through measurement for X, Y and Z axes. (b) Sensor response curves for each axis (solid lines) and cross terms (broken lines) in X and Z axes, compared with the old response measured at the center of the bore-hole (dotted lines).

components explicitly as

$$\begin{bmatrix} \mathbf{d}_x \\ \mathbf{d}_y \\ \mathbf{d}_z \end{bmatrix} = \begin{bmatrix} \mathbf{R}_{xx} & \mathbf{0} & \mathbf{R}_{zx} \\ \mathbf{0} & \mathbf{R}_{yy} & \mathbf{0} \\ \mathbf{R}_{xz} & \mathbf{0} & \mathbf{R}_{zz} \end{bmatrix} \begin{bmatrix} \mathbf{m}_x \\ \mathbf{m}_y \\ \mathbf{m}_z \end{bmatrix} + \begin{bmatrix} \varepsilon_x \\ \varepsilon_y \\ \varepsilon_z \end{bmatrix}, \quad (3)$$

where each subscript on \mathbf{d} , \mathbf{m} , and ε , as x, y and z corresponds to X, Y and Z component, respectively. Subscripts on response matrix \mathbf{R} , as xx, zx, yy, xz and zz corresponds to X-component of magnetization to X-axis pick-up coil, Z to X, Y to Y, X to Z, and Z to Z, respectively. Each component of \mathbf{d} , \mathbf{m} , \mathbf{R} , and \mathbf{e} are expressed as

$$\mathbf{d}_i = \begin{pmatrix} d_{i1} \\ d_{i2} \\ \vdots \\ d_{iN} \end{pmatrix}, \quad \mathbf{m}_j = \begin{pmatrix} m_{j1} \\ m_{j2} \\ \vdots \\ m_{jM} \end{pmatrix}, \quad \mathbf{R}_{ji} = \begin{pmatrix} R_{ji-1} & \cdots & R_{ji-r} & \mathbf{0} \\ \vdots & & \ddots & \\ R_{ji0} & & & R_{ji-r} \\ \vdots & \ddots & & \vdots \\ \vdots & & \ddots & \vdots \\ \vdots & & & \vdots \\ R_{ji+r} & & & R_{ji0} \\ \vdots & & & \vdots \\ \mathbf{0} & R_{ji+r} & \cdots & R_{ji+1} \end{pmatrix}, \quad \mathbf{e}_i = \begin{pmatrix} \varepsilon_{i1} \\ \varepsilon_{i2} \\ \vdots \\ \varepsilon_{iN} \end{pmatrix}.$$

Here N is the total number of measured points, and M is the number of unit slices of the sample. " l " is the number of measured points beyond the sample, " r " is half the number of measured sensor response function, and

R_{i0} corresponds to the center of the sensor.

2.2 Bayesian statistics

We assumed that the noise in three axes are independent and can be expressed as a Gaussian noise of zero mean and variance v . The likelihood function of the whole-core data is given by

$$L(\mathbf{d}|\mathbf{m},v) = \left(\frac{1}{2\pi v}\right)^{3N} \exp\left\{-\frac{1}{2v} \|\mathbf{d} - \mathbf{Rm}\|^2\right\}, \quad (4)$$

where $\|\cdot\|^2$ represents Euclidian norm.

In order to reduce the instability of the solution, the magnetization is assumed to change smoothly along core. The smoothness of the magnetization can be measured by 2-norm of second order difference as

$$\sum_{j=1}^M \left\{ |m_{xj} - 2m_{xj-1} + m_{xj-2}|^2 + |m_{yj} - 2m_{yj-1} + m_{yj-2}|^2 + |m_{zj} - 2m_{zj-1} + m_{zj-2}|^2 \right\}$$

This can be presented simply by a matrix expression as

$$\|\mathbf{D}^* \mathbf{m}^*\|^2$$

$$\mathbf{D}^* = \begin{pmatrix} \mathbf{D}_1^* & \mathbf{0} & \mathbf{0} \\ \mathbf{0} & \mathbf{D}_1^* & \mathbf{0} \\ \mathbf{0} & \mathbf{0} & \mathbf{D}_1^* \end{pmatrix}, \quad \mathbf{D}_1^* = \begin{pmatrix} 1 & -2 & 1 & & \mathbf{0} \\ & \ddots & \ddots & \ddots & \\ \mathbf{0} & & 1 & -2 & 1 \end{pmatrix},$$

$$\mathbf{m}^* = (m_{x-1} \ m_{x0} \ \mathbf{m}_x^T \ m_{y-1} \ m_{y0} \ \mathbf{m}_y^T \ m_{z-1} \ m_{z0} \ \mathbf{m}_z^T)^T,$$

where \mathbf{D}^* denotes a matrix of second order difference composed of \mathbf{D}_1^* representing second-order differences for one component. \mathbf{m}^* is composed

of magnetization vector and six properly chosen parameters $m_{x,-1}$, $m_{x,0}$, $m_{y,-1}$, $m_{y,0}$, $m_{z,-1}$, and $m_{z,0}$. This can be transformed by using modified form of second-order difference matrix \mathbf{D} and vector \mathbf{z} to isolate newly introduced parameters from magnetization vector.

$$\|\mathbf{z} - \mathbf{D}\mathbf{m}\|^2$$

$$\mathbf{D} = \begin{pmatrix} \mathbf{D}_1 & \mathbf{0} & \mathbf{0} \\ \mathbf{0} & \mathbf{D}_1 & \mathbf{0} \\ \mathbf{0} & \mathbf{0} & \mathbf{D}_1 \end{pmatrix}, \mathbf{D}_1 = \begin{pmatrix} 1 & & & & & \\ -2 & 1 & & & & \\ 1 & -2 & 1 & & & \\ & \ddots & \ddots & \ddots & \ddots & \\ \mathbf{0} & & 1 & -2 & 1 & \end{pmatrix}$$

$$\mathbf{z} = (-m_{x,-1} + 2m_{x,0}, -m_{x,0}, 0, \dots, 0, -m_{y,-1} + 2m_{y,0}, -m_{y,0}, 0, \dots, 0, -m_{z,-1} + 2m_{z,0}, -m_{z,0}, 0, \dots, 0)^T$$

In order to express smoothly changing magnetization, the second-order difference is assumed to distribute as a Gaussian with zero mean and variance v/u^2 . By using a matrix expression above, the prior distribution of magnetization \mathbf{m} is given by

$$\pi(\mathbf{m}|v, u) = \left(\frac{u^2}{2\pi v}\right)^{\frac{3M}{2}} |\mathbf{D}^{-1}\mathbf{D}|^{\frac{1}{2}} \exp\left\{-\frac{u^2}{2v} \|\mathbf{z} - \mathbf{D}\mathbf{m}\|^2\right\}. \quad (5)$$

Here u is a hyper parameter that express the degree of smoothness, $|\mathbf{D}^{-1}\mathbf{D}|$ represents determinant of the matrix inside. Eq.(5) is normalized to give unity under integration to infinity.

According to the Bayes' theorem, the posterior distribution of the magnetization is constituted by the likelihood function and the prior distribution (Akaike, 1989) as

$$\begin{aligned}\pi_{\text{post}}(\mathbf{m}|\mathbf{d},v,u) &\propto L(\mathbf{d}|\mathbf{m},v) \pi(\mathbf{m}|v,u). \\ &= \left(\frac{1}{2\pi v}\right)^{\frac{3N}{2}} \left(\frac{u^2}{2\pi v}\right)^{\frac{3M}{2}} |\mathbf{D}^t \mathbf{D}|^{\frac{1}{2}} \exp\left(-\frac{\mathbf{S}}{2v}\right) d\mathbf{m},\end{aligned}\quad (6)$$

where

$$S = \|\mathbf{d} - \mathbf{Rm}\|^2 + u^2 \|\mathbf{z} - \mathbf{Dm}\|^2 \quad (7)$$

Minimization of S can be interpreted as a constrained least squares method, which is generally used for solving inverse problems (e.g. Tarantola, 1987; Dimri, 1992).

2.3 Akaike's Bayesian Information Criterion (ABIC)

A Bayesian Information Criterion (ABIC) was proposed by AKAIKE (1980) to determine optimum parameter for Bayes models, which is given by a log maximum marginal likelihood as

$$\begin{aligned}\text{ABIC} &= -2 \log \int \pi_{\text{post}}(\mathbf{m}|\mathbf{d}, v, u) d\mathbf{m}. \\ &\quad + 2 (\text{number of adjusted hyperparameters})\end{aligned}\quad (8)$$

By substituting Eq.(6) to Eq. (8) ABIC is calculated as

$$\begin{aligned}\text{ABIC} &= -2 \log \int \left(\frac{1}{2\pi v}\right)^{\frac{3N}{2}} \left(\frac{u^2}{2\pi v}\right)^{\frac{3M}{2}} |\mathbf{D}^t \mathbf{D}|^{\frac{1}{2}} \exp\left(-\frac{\mathbf{S}}{2v}\right) d\mathbf{m} + 2 \\ &= 3N \log 2\pi v - 3M \log u^2 - \log |\mathbf{D}^t \mathbf{D}| - 2 \log \int \left(\frac{1}{2\pi v}\right)^{\frac{3M}{2}} \exp\left(-\frac{\mathbf{S}}{2v}\right) d\mathbf{m} + 2\end{aligned}\quad (9)$$

Eq. (7) can be transformed by using

$$\mathbf{b} = \begin{bmatrix} \mathbf{d} \\ u\mathbf{z} \end{bmatrix} \text{ and } \mathbf{F} = \begin{bmatrix} \mathbf{R} \\ u\mathbf{D} \end{bmatrix}.$$

$$S = \|\mathbf{b} - \mathbf{F}\mathbf{m}\|^2 \quad (10)$$

where \mathbf{m}_0 is \mathbf{m} that minimizes S . As the best solution $\mathbf{F}\mathbf{m}_0$ is closer from \mathbf{b} than any other vector $\mathbf{F}\mathbf{m}$, S is decomposed to $\|\mathbf{b} - \mathbf{F}\mathbf{m}_0\|^2$ and $\|\mathbf{F}(\mathbf{m} - \mathbf{m}_0)\|^2$ as

$$\begin{aligned} S &= \|\mathbf{b} - \mathbf{F}\mathbf{m}_0\|^2 + \|\mathbf{F}(\mathbf{m} - \mathbf{m}_0)\|^2 \\ &= S^* + \|\mathbf{F}(\mathbf{m} - \mathbf{m}_0)\|^2 \end{aligned} \quad (11)$$

where $S^* = \|\mathbf{d} - \mathbf{R}\mathbf{m}_0\|^2 + u^2\|\mathbf{z} - \mathbf{D}\mathbf{m}_0\|^2$.

The integral in Eq. (9) can be calculated by substituting Eq. (10) and Eq. (11) successively as

$$\begin{aligned} -2\log \int \left(\frac{1}{2\pi v}\right)^{\frac{3M}{2}} \exp\left(-\frac{S}{2v}\right) d\mathbf{m} &= -2\log \int \left(\frac{1}{2\pi v}\right)^{\frac{3M}{2}} \exp\left(-\frac{S^*}{2v}\right) \exp\left\{-\frac{1}{2v} \|\mathbf{F}(\mathbf{m} - \mathbf{m}_0)\|^2\right\} d\mathbf{m} \\ &= \frac{S^*}{v} - 2\log \int \left(\frac{1}{2\pi v}\right)^{\frac{3M}{2}} \exp\left\{-\frac{1}{2v} \|\mathbf{F}(\mathbf{m} - \mathbf{m}_0)\|^2\right\} d\mathbf{m} \quad (12) \\ &= \frac{S^*}{v} + \log |\mathbf{F}^t \mathbf{F}| \end{aligned}$$

Again go back to Eq. (9) and substitute Eq. (12), then get

$$ABIC = 3N \log 2\pi v + \frac{S^*}{v} - 3M \log u^2 - \log |\mathbf{D}^t \mathbf{D}| + \log |\mathbf{F}^t \mathbf{F}| + 2 \quad (13)$$

By differentiating with respect to v we get v that minimizes ABIC as $v_{\min} = S^*/3N$. The final form of ABIC can be obtained by substituting v_{\min} to Eq. (12) as

$$ABIC = 3N \log \frac{2\pi S^*}{3N} + 3N - 3M \log u^2 - \log |\mathbf{D}^t \mathbf{D}| + \log |\mathbf{F}^t \mathbf{F}| + 2 \quad (14)$$

2.4 Matrix calculation

We can obtain \mathbf{m}_0 in Eq. (14) by basic matrix calculations. The parameters in \mathbf{z} are included in \mathbf{m}^* combined with \mathbf{m} , which can be minimized simultaneously. The formula is modified as

$$\begin{aligned} \|\mathbf{d} - \mathbf{R}\mathbf{m}_0\|^2 + u^2\|\mathbf{z} - \mathbf{D}\mathbf{m}_0\|^2 &= \|\mathbf{b} - \mathbf{F}\mathbf{m}_0\|^2 \\ &= \|\mathbf{b}^* - \mathbf{F}^*\mathbf{m}_0^*\|^2 \end{aligned} \quad (15)$$

where

$$\mathbf{b}^* = \begin{bmatrix} \mathbf{d} \\ 0 \\ \vdots \\ 0 \end{bmatrix}, \quad \mathbf{F}^* = \begin{bmatrix} \mathbf{R}^* \\ u\mathbf{D}^* \end{bmatrix},$$

$$\mathbf{R}^* = \begin{bmatrix} \mathbf{R}_{xx}^* & \mathbf{0} & \mathbf{R}_{zx}^* \\ \mathbf{0} & \mathbf{R}_{yy}^* & \mathbf{0} \\ \mathbf{R}_{xz}^* & \mathbf{0} & \mathbf{R}_{zz}^* \end{bmatrix}, \quad \mathbf{R}_{ji}^* = \begin{bmatrix} 0 & 0 \\ \vdots & \vdots \\ 0 & 0 \end{bmatrix} \mathbf{R}_{ji}^*,$$

Minimization of $\|\mathbf{b}^* - \mathbf{F}^*\mathbf{m}_0^*\|^2$ can be accomplished by solving $\mathbf{F}^{*T}\mathbf{b}^* = \mathbf{F}^{*T}\mathbf{F}^*\mathbf{m}_0^*$. Given $\mathbf{G} = \mathbf{F}^{*T}\mathbf{F}^*$, magnetization can be obtained by

$$\mathbf{m}_0^* = \mathbf{G}^{-1}\mathbf{F}^{*T}\mathbf{b}^* \quad (16)$$

\mathbf{G}^{-1} can be calculated by LDU decomposition using Modified Cholesky Method (Togawa, 1971) and \mathbf{m}_0^* was obtained by Eq. (16).

Minimum ABIC is searched in *Inuspace* by initially bracketing by Golden Section Search and subsequently converging by Brent's Method to tolerance of 0.1 which is enough for convergence in this case (Press et al., 1992).

2.5 Error and resolution

It can be shown that the magnetization distributes as Gaussian following the covariance matrix

$$\varepsilon^2 \mathbf{G}^{-1} \quad (17)$$

Let g_{ii} be the i th diagonal component of \mathbf{G}^{-1} , the estimated error of magnetization for i -th slice can be expressed by

$$\sigma_{mi} = \varepsilon \sqrt{g_{ii}} \quad (17')$$

where ε is the standard deviation of magnetometer output, which can be estimated from the residual of model and measurement. Factor 1.96 is multiplied to σ_{mi} to get 95% confidence limit for the magnetization. The non-diagonal component of covariance matrix means degree of dependence on the neighboring data points. The matrix components of x-axis are typically look like as Fig. 2a. The resolution of the data points can be defined as the width of zero crossing points. Resolution at the center of the core for x, y and z axes were calculated and the average value is defined as the resolution for the data. For a given response matrix and length of the core, resolution can be definitely calculated as a function of lnu (Fig. 2b).

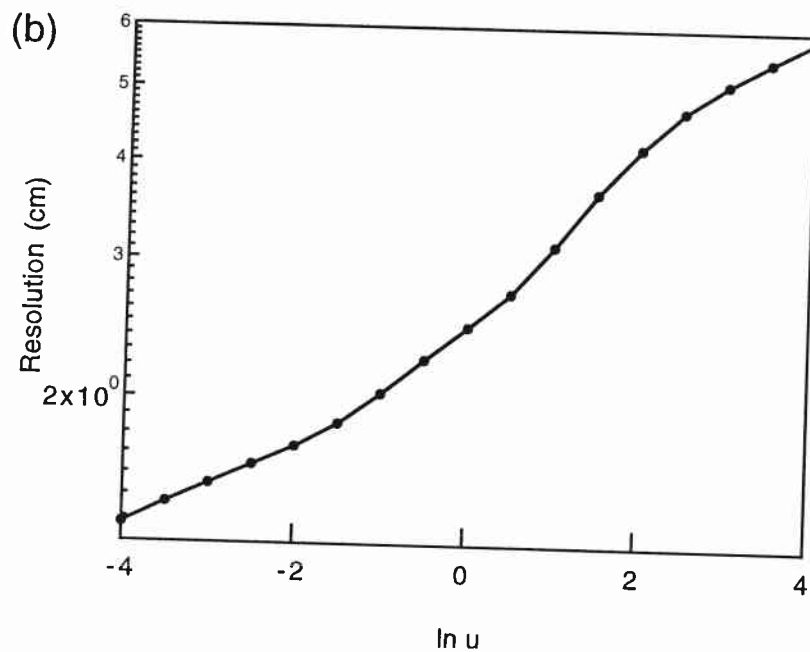
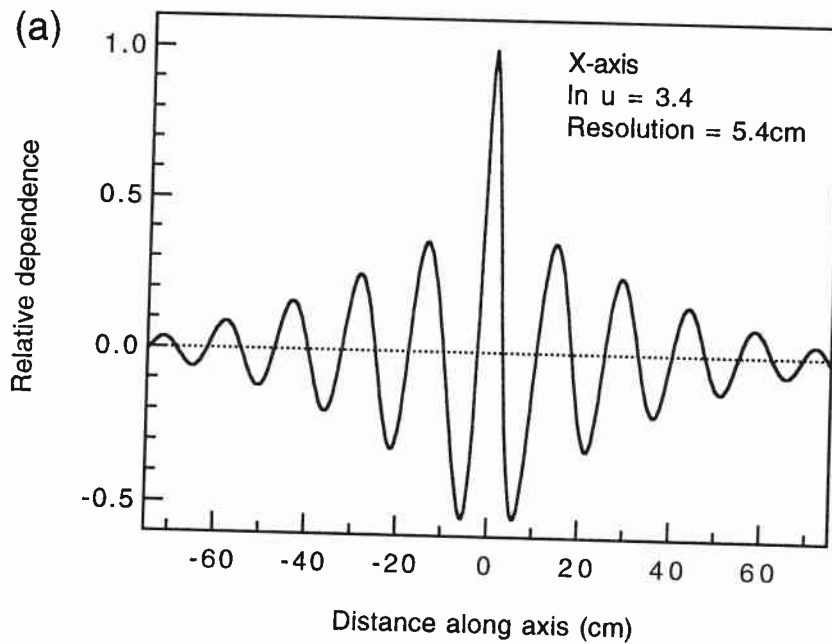


Fig. 2. (a) Kernel for the X-axis response function at $\ln u = 3.4$. The spatial resolution measured by zero crossings of the curve is 5.4 cm. (b) Plot of resolution versus $\ln u$ measured by zero crossings of the kernel.

3. Applications

3.1 Description of measurement system

Just after the drilling about 9.5m-long APC "Cores" are cut into 1.5m-long "Sections". These whole-round samples are sent to multi-sensor-track and are subsequently split into working and archive halves.

The archive halves are measured by using a pass-through type SQUID rock magnetometer (SRM) of 2G Enterprises (model 760R) on board Joides Resolution (Fig. 3). Samples are inserted in the bore hole of the magnetometer by a plastic container connected to a stepping motor with a polyurethane rope. The samples are demagnetized at several demagnetizing steps with an AF demagnetizer (model 2G600) in three axes in line with the cryogenic SRM. A FASTCOM4 multi-serial communication board was installed in the PC-AT compatible computer which controls the SRM, the demagnetizer, and the stepping motor that transports the core samples. The SQUID electronics of the SRM are operating at the 1X scale and using flux-counting mode. The X-axis component of SQUID magnetometer must be inverted to get vector components in sample frame (Core-north, Core-east, Down-core).

Sensor response curves were obtained by measurements on thin half-circle-shaped standard samples made of magnetic tape magnetized to X, Y, and Z axes. Measurements were conducted twice for each axis and were averaged to get sensor response curves (Fig. 1b). Note that the magnetization in X-axis is detected by Z-axis pick-up coil with peak amplitude of about 10% of X-axis amplitude and magnetization in Z-axis appear in X-axis coil as 20% of X-axis.

3.2 Synthetic data

In order to test the deconvolution scheme, synthetic magnetization was produced by the following equation,

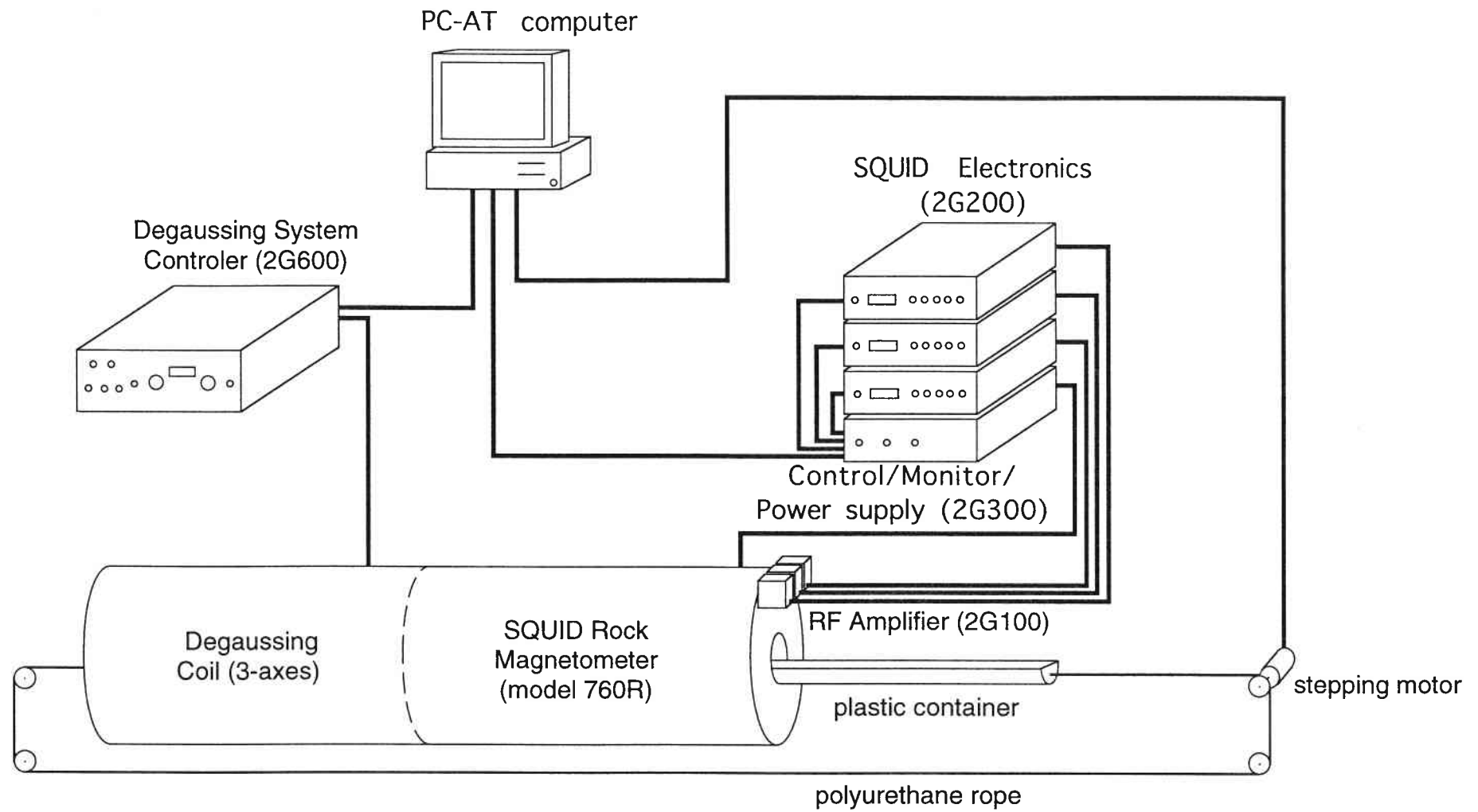


Fig. 3. Schematic diagram of pass-through measurement system of SQUID magnetometer on ODP's research vessel (Joides Resolution). See text for detailed explanation.

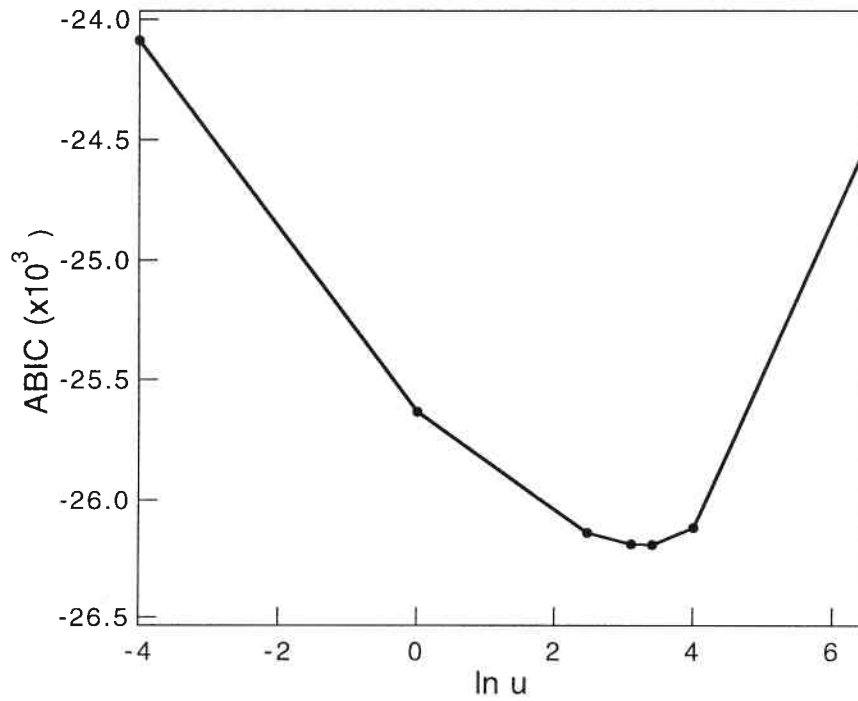


Fig. 4. ABIC values are plotted versus $\ln u$ values for the deconvolution of synthetic data with Gaussian noise of $S/N=51.6$. ABIC comes to minimum value of -26188 where $\ln u$ equals to 3.41 around the middle of a downward convex curve.

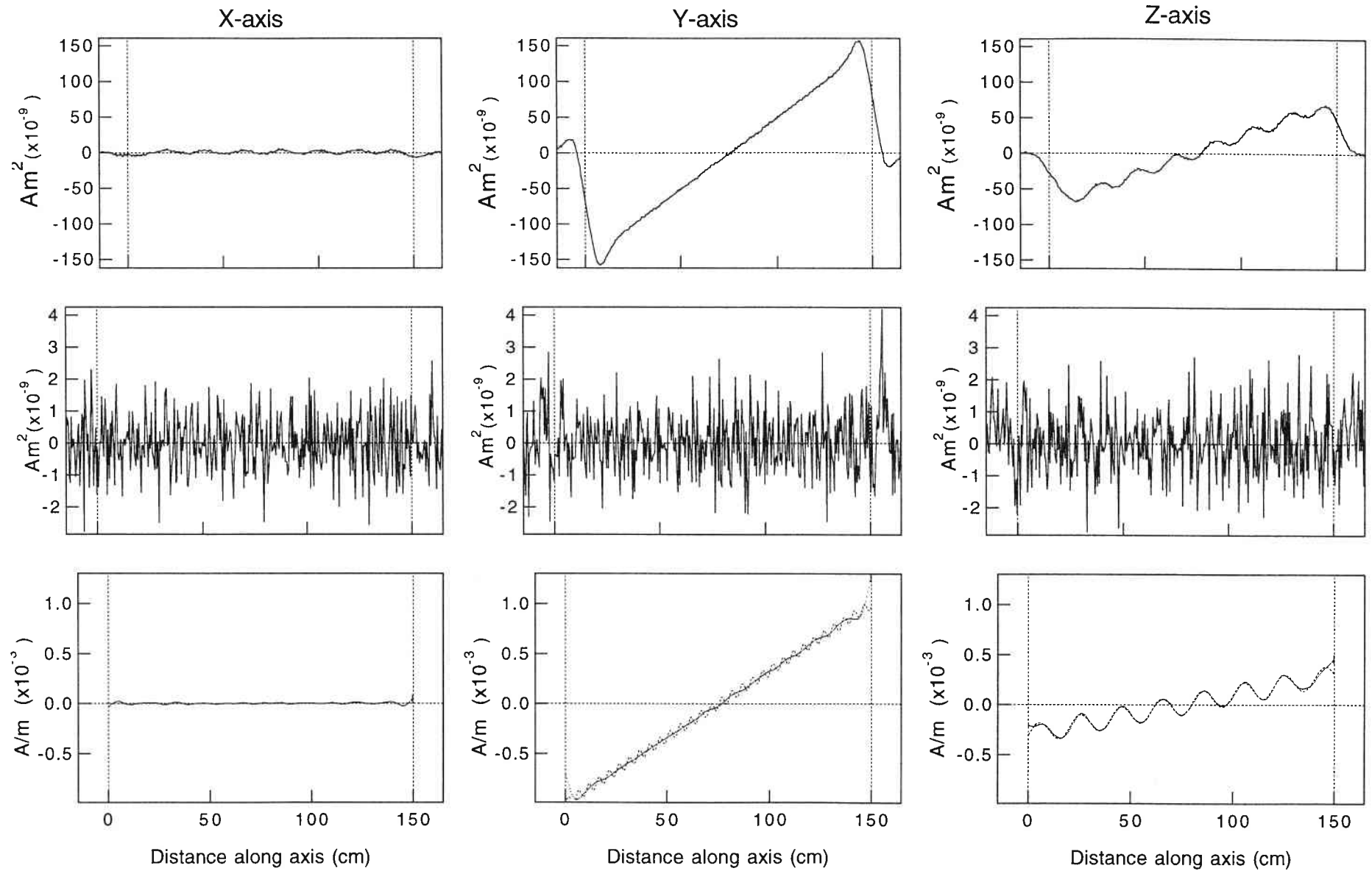


Fig. 5. Results of deconvolution for the synthetic magnetization record with polarity reversal and fluctuations in Y and Z axes. Results for X, Y and Z axes are shown from left to right columns. The top row represents magnetic moment artificially produced from the synthetic magnetization record by convolution and superimpose of Gaussian noise with S/N ratio of 51.6. Middle row shows residual of the original magnetic moment and the magnetic moment for model magnetization after deconvolution. Bottom row shows the original synthetic magnetization before convolution (broken lines) and the model magnetization obtained by deconvolution (dots).

$$\begin{aligned}
x &= 0 \\
y &= 1 \times 10^{-6} \left(\frac{i-150}{150} + 0.05 \sin \frac{2\pi}{10} i \right) \\
z &= 1 \times 10^{-6} \left(0.3 \frac{i-150}{150} + 0.1 \sin \frac{2\pi}{40} i \right)
\end{aligned} \tag{18}$$

where i is an index of the data points. The measurement spacing is set to 5mm and the length of the core is 150 cm. 15 cm on both sides of the core were also included in the measurement. In order to mimic the geomagnetic reversal records, y and z data is designed to change its polarity around middle of the synthetic long-core data with sinusoidal fluctuations of 5 cm and 20 cm wave length, while x is constantly zero to see the cross term produced by the z component magnetization. After convolving the magnetization by the sensor response curve, Gaussian noise was added with the amplitude corresponding to S/N ratios of 51.6.

ABIC draw simple downward convex curve versus lnu and comes to minimum of -26188 at $lnu = 3.41$ (Fig. 4). The results of deconvolution are shown on Fig. 5. The variation of shorter wave length in y axis (2.5 cm in half wave length) were smeared out by the noise and could not be detected by deconvolution because the spacial resolution for $lnu=3.41$ is 5.4 cm (Fig. 2b). On the contrary, longer wave length fluctuation in z axis (10 cm in half wave length) are recovered by deconvolution. This fluctuation can be seen before deconvolution, however, the amplitude of fluctuation is larger after deconvolution. This fluctuation in z axis (dots) is in good agreement with the original one (broken line). The x component suffers only little variation which can be negligible.

The residual for all the component distribute as a Gaussian without any systematic change. The estimated S/N ratio for this case is 52.7, which is very close to the value of the original data (51.6). These character of noise are consistent with the primary assumption that the noise distribute as a Gaussian.

3.3 Real data

Deep sea sediment cores from ODP Leg 124 were used as examples of real pass-through data. High sedimentation rates and high concentration of magnetic mineral of these cores provided us materials suitable for detailed magnetostratigraphic study (Rangin, 1990). Four sections from Site 769, 769B-7H6 (1.5m long), 769B-7H7 (0.7m long), 769A-7H4 (1.5m long) and 769A-7H5 (1.5m long), which correspond to the Brunhes/Matuyama polarity transition, were used. These samples were measured by a pass-through cryogenic magnetometer at intervals of 5mm after exposure to alternating magnetic fields of 15 mT and 20 mT including 15 cm beyond the region of the cores on both sides.

The data needs three kinds of corrections before deconvolution (Fig. 5). One is drift of the SQUID magnetometer, which is corrected by subtracting baseline value on PC-AT computer automatically just after the acquisition of SQUID output signal. Second are spike noises probably related to electromagnetic noise, which is often recognized with the use of other electronics near the magnetometer. This can be corrected by replacing to the interpolated value. Third are abrupt stepwise changes, one of which can be recognized as miscounting of flux jumps. These jumps exactly correspond to the magnetic moment of a flux quanta (ϕ_0) for X, Y, and Z axes ($1.740 \times 10^{-4} \text{ emu}/\phi_0$, $1.646 \times 10^{-4} \text{ emu}/\phi_0$, and $1.215 \times 10^{-4} \text{ emu}/\phi_0$). These were corrected easily by adding or subtracting the values corresponding to the flux quanta. There are another kind of jumps, which we could not specify the source. These values are around $1.6 \times 10^{-8} \text{ Am}^2$, which are smaller than flux-jump related miscounting. The magnitude of jumps were estimated by assuming smoothly changing trends. These two kinds of jumps results in an apparent drift (Fig. 6a) and lead to overcorrection (Fig. 6b). After corrections are completed (Fig. 6c), this should be resumed (Fig. 6d).

The jumps and spike noise removed before deconvolution are listed

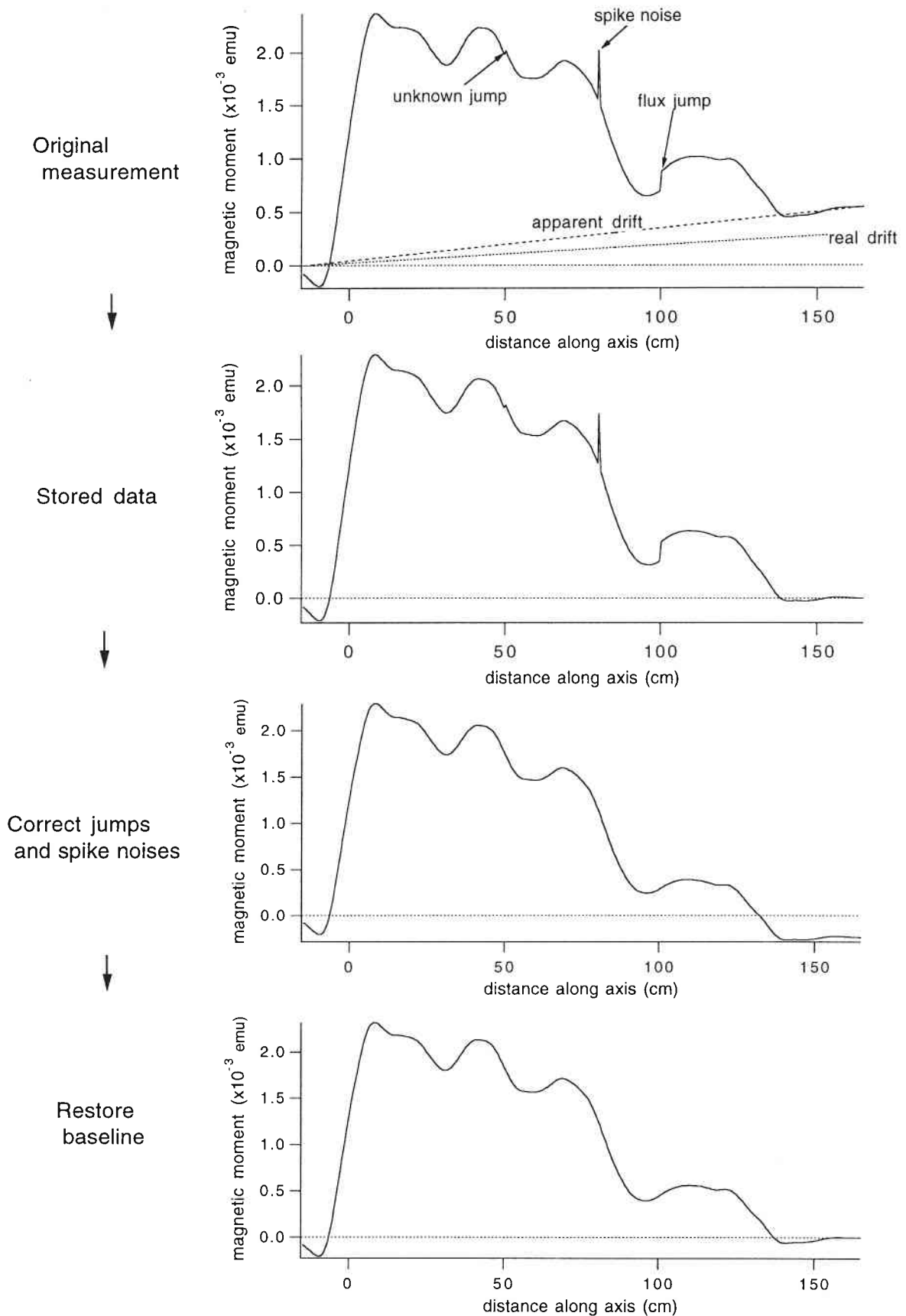


Fig. 6. Diagram showing data correction procedures. (a) Row data directly acquired by PC-AT computer contains real drift of the magnetometer and apparent drift caused by jumps. (b) The difference between baseline value before and after the measurement is considered as drift and linearly interpolated values are stored in the file. (c) The corrections of jumps and spike noises results in over-correction due to apparent drift and (d) the baseline should be resumed by linear interpolation.

Table 1. Flux jumps, other jumps and spike noises recognized for the pass-through measurements are listed. In each box left hand value represent index number of the positions of the noise and right hand value are the magnitude of noise in emu. Flux jumps are listed in the unit of flux quana (X: $1.740 \times 10^{-4} \text{ emu}/\Phi_0$, Y: $1.646 \times 10^{-4} \text{ emu}/\Phi_0$, Z: $1.215 \times 10^{-4} \text{ emu}/\Phi_0$).

Section	Demag.	X			Y			Z						
		flux jump	other jumps	spike noise	flux jump	other jumps	spike noise	flux jump	other jumps	spike noise				
769A-7H4	15mT				162	-1	32	4.21E-05	93	1.45E-05	93	1		
							312	-3.12E-05						
								330	-3.40E-05					
769A-7H4	20mT						73	3.03E-05				102	1.62E-05	
							308	-4.33E-05				237	-1.50E-05	
								332	-3.85E-05					
769A-7H5	15mT					211	-3.55E-05							
769A-7H5	20mT						224	-3.20E-05						
							333	3.14E-05						
769B-7H6	15mT	35	1				297	-3.36E-05				103	1.39E-05	
		311	-1									215	1.75E-05	
769B-7H6	20mT	35	1				296	-3.49E-05				72	1.00E+00	
												229	1.76E-05	
769B-7H7	15mT	143	-1				137	-3.15E-05						
		180	1				173	2.68E-05						
769B-7H7	20mT						145	-3.60E-05						
							173	3.33E-05						

in Table 1. These were recognized as discontinuous points by monitoring magnetization and its difference simultaneously on display. In these cases, unknown jumps in Y-axis are the most frequent noises, which sometimes appear at the same position in different demagnetization levels.

3.3.1 Section 769B-7H6

The results of ABIC minimizing deconvolution on Section 124-769B-7H6 are shown on Fig. 7. Magnetic moment measured with a pass-through magnetometer, residuals of calculated model moment, and magnetization obtained by the deconvolution are shown for X, Y and Z axes. ABIC comes to minimum value of -23465 when lnu equals to -2.09 (Table 2; case a). S/N ratio for total magnetic moment is calculated by dividing root mean squares of SQUID output, which is obtained as 566. As a result, the deconvolution improved spacial resolution of magnetization to about 2 cm in maximum. Residuals are composed of white noise and periodic waves whose wave lengths is about 15 cm.

Deconvolution by the sensor response curves customarily used on ODP, which were measured on the standard sample in the center of the bore hole (Fig. 1b; dotted lines), were also conducted and the results were compared with those of the new response curves (Fig. 8). The minimum ABIC value is much higher (-20723) than that for the correct response (-23465), indicating that the new response (Table 2; case a) is much better than the old one (Table 2; case b). The estimated S/N ratio was also lowered from 566 to 123 by using the old responses.

The response curve without cross terms were also used for the deconvolution (Table 2; case c). The results show higher minimum ABIC (-23015) and lower S/N ratio (482), which indicate that the cross terms improve the deconvolution. However, the difference of solution is not significant (Fig. 9).

Table 2. Results of deconvolution are listed for different measurements in different conditions. Average ABIC were calculated by dividing minimum ABIC values by number of data and number of axes to compare the results in different conditions. This value represents minimum ABIC value for one vector component of one data point.

case	Demag.	Section	Response curve	Conditions	number of data	number of axes	In u	minimum ABIC	average ABIC	S/N ratio
a	20mT	769B-7H6	New		360	3	-0.209	-23465	-21.73	566
b		769B-7H6	Old		360	3	1.386	-20728	-19.19	123
c		769B-7H6	New w/o X-terms		360	3	-0.472	-23015	-21.31	482
d		769B-7H6	New w/o X-terms	x-axis	360	1	0.498	-7831	-21.75	535
e			New w/o X-terms	y-axis	360	1	-0.239	-7794	-21.65	728
f			New w/o X-terms	z-axis	360	1	-1.059	-7501	-20.84	175
g			New w/o X-terms	average (x,y,z)	360	1	-	-	-21.41	479
h		769B-7H7	New		200	3	-0.282	-13344	-22.24	401
i		769B-7H6,7	New	average (7H6, 7)	560	3	-	-	-21.91	507
j			New	not overlapped	560	3	-0.402	-36732	-21.86	529
k			New	overlapped	500	3	-0.261	-32592	-21.73	552
l		769A-7H4	New		360	3	-0.281	-23173	-21.46	667
m		769A-7H5	New		360	3	-0.592	-24618	-22.79	547
n		769A-7H4,5	New	average (7H4, 5)	720	3	-	-	-22.13	607
o			New	not overlapped	720	3	-0.496	-47220	-21.86	646
p			New	overlapped	660	3	-0.431	-43242	-21.84	702
q	15mT	769B-7H6	New		360	3	-0.403	-23409	-21.67	588
r		769B-7H7	New		200	3	-0.517	-13237	-22.06	432
s		769B-7H6,7	New	average (7H6, 7)	560	3	-	-	-21.81	510
t			New	not overlapped	560	3	-0.585	-36597	-21.78	549
u			New	overlapped	500	3	-0.541	-32433	-21.62	577
v		769A-7H4	New		360	3	-0.368	-22948	-21.25	751
w		769A-7H5	New		360	3	-0.599	-24077	-22.29	496
x		769A-7H4,5	New	average (7H4, 5)	720	3	-	-	-21.77	624
y			New	not overlapped	720	3	-0.608	-46634	-21.59	701
z			New	overlapped	660	3	-0.460	-42687	-21.56	750

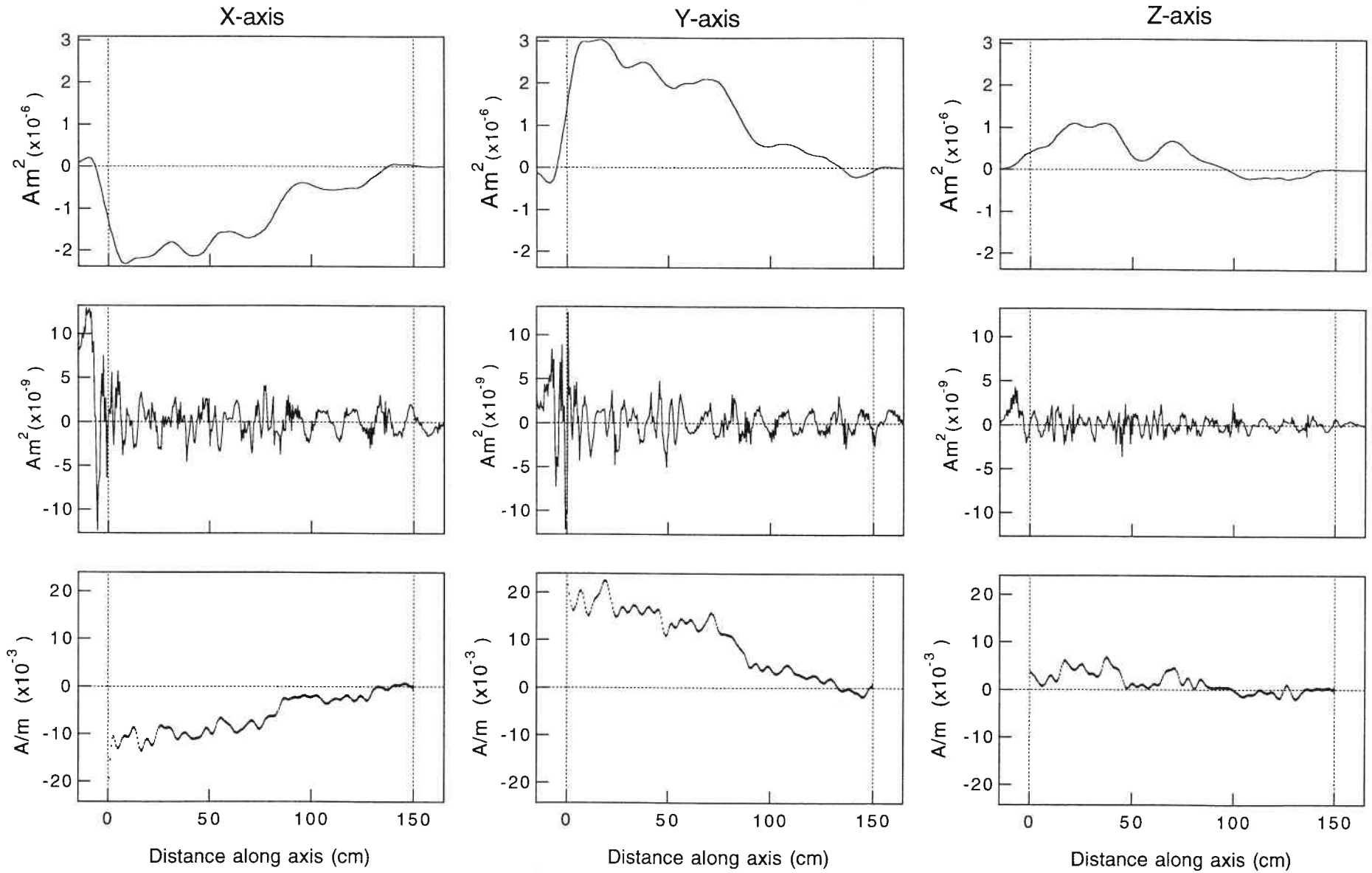


Fig. 7. Results of deconvolution for the pass-through data of 769B-7H6 after demagnetization at peak alternating field of 20 mT. Results for X, Y and Z axes are shown from left to right columns. The top row represents magnetic moment artificially produced from the synthetic magnetization record by convolution and superimpose of Gaussian noise with S/N ratio of 51.6. Middle row shows residual of the original magnetic moment and the magnetic moment for model magnetization after deconvolution. Bottom row shows model magnetization obtained by deconvolution (dots with vertical bars representing 95 % confidence limits).

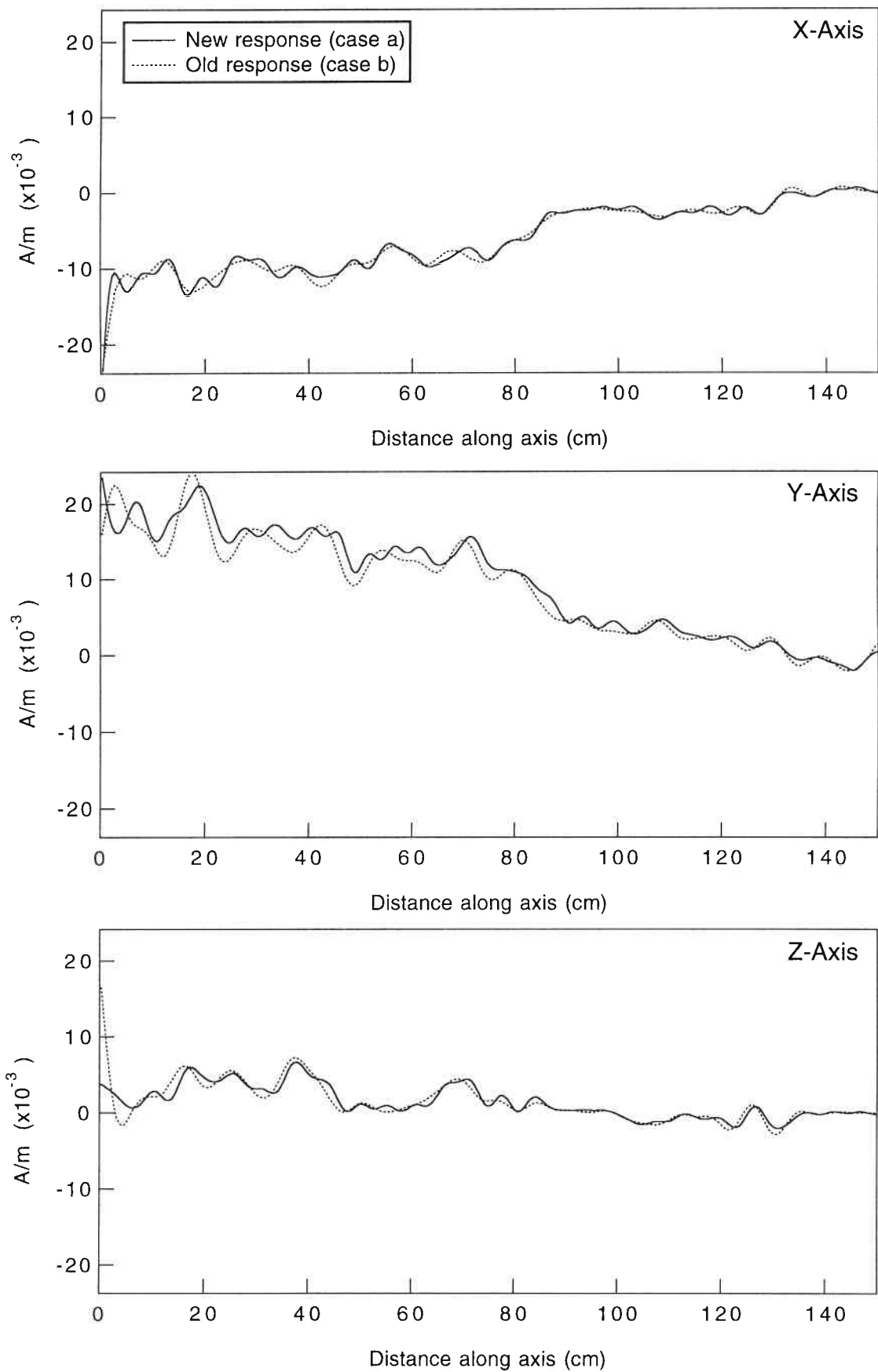


Fig. 8. The magnetizations obtained by deconvolution for the measurements of Section 769B-7H6 at 20 mT AF demagnetization are plotted for the correct response curve (solid lines) and for the old response curve used conventionally on ODP's Research Vessel (broken lines).

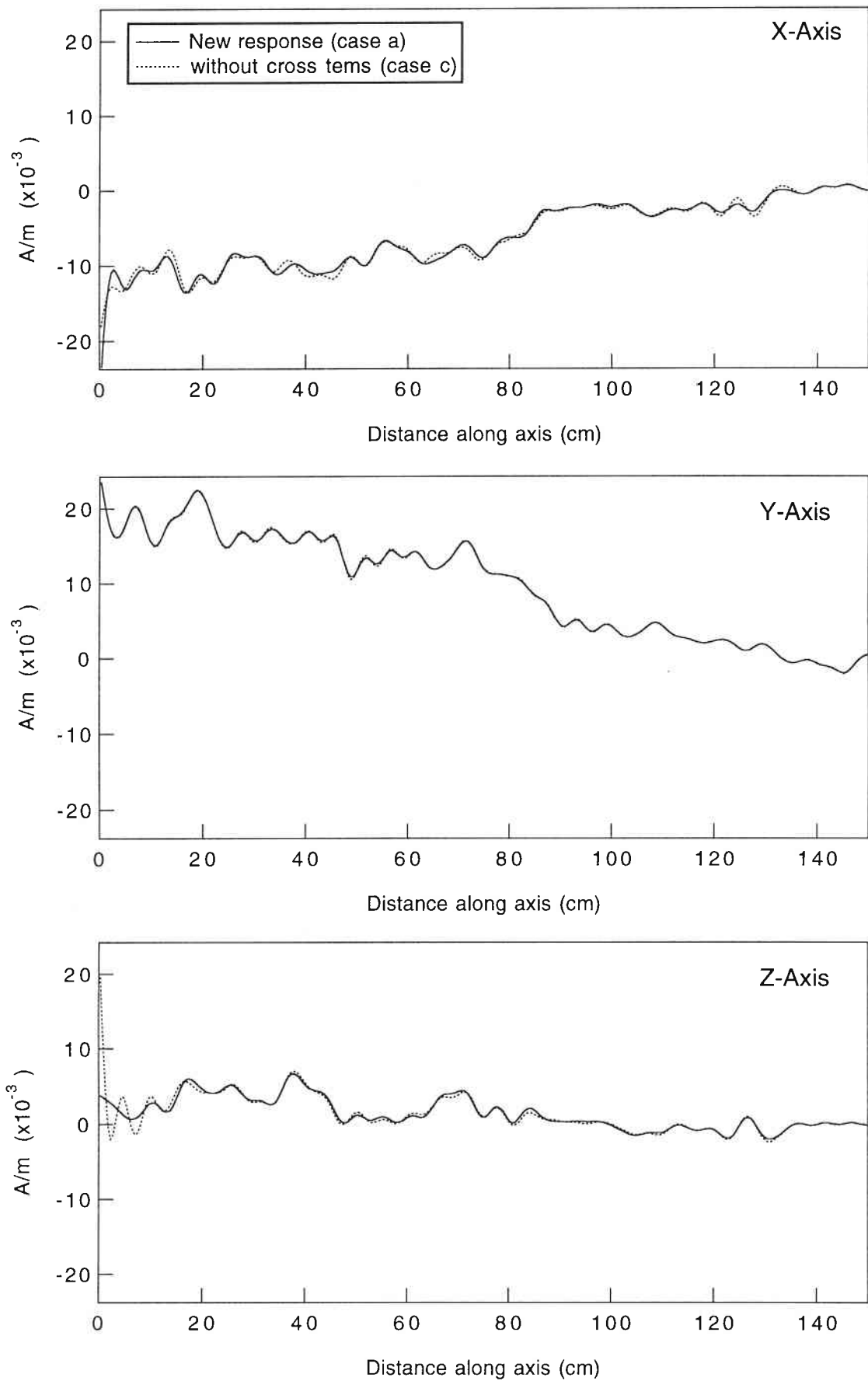


Fig. 9. The magnetizations obtained by deconvolution for the measurements of Section 769B-7H6 at 20 mT AF demagnetization are plotted for the correct response curve (solid lines) and for the response without cross terms (broken lines).

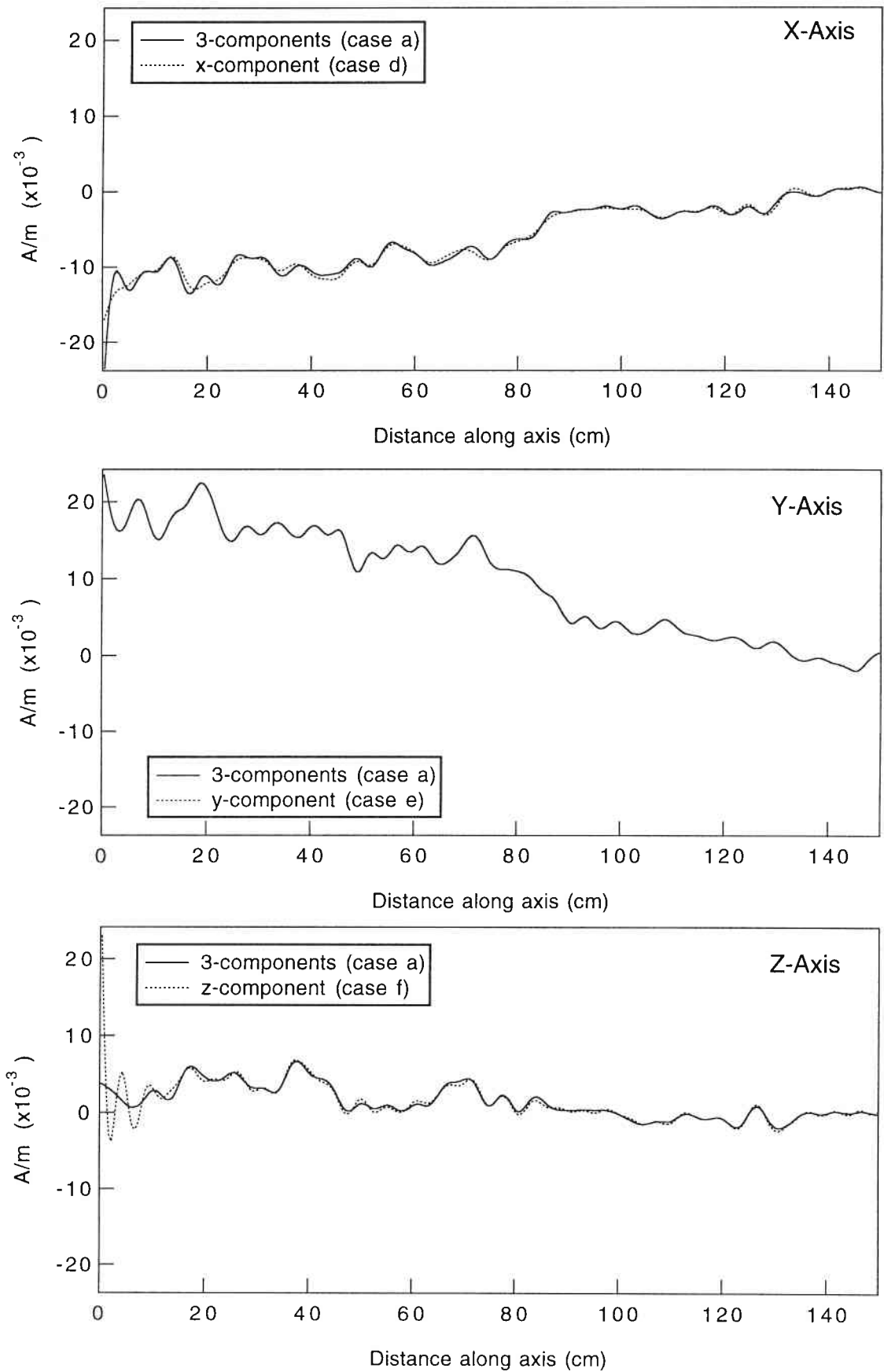


Fig. 10. The deconvolved magnetizations for the measurements of Section 769B-7H6 at 20 mT AF demagnetization by the correct response curve are plotted by solid lines. The results of deconvolution separately conducted on the same data are plotted by broken lines.

The single component deconvolution by Oda and Shibuya (1994) was also conducted separately in each axis (Table 2; case *d*, *e*, *f*) by using the new sensor response curves without cross terms. Minimum ABIC corresponding to one component of one data point (later referred as "average ABIC") was also calculated for general comparison. The results are nearly the same as the new three-dimensional deconvolution (Fig. 10) except that average ABIC (-21.41) is larger than that of case *a* (-21.73). S/N ratio averaged for the three axes was 479, which is lower than the value for case *a* (566).

The difference between case *c* and case *g* is smaller than between case *a* and case *g*, because both are deconvolved without cross terms. The most significant difference recognized for these tests was between case *a* and case *b*, which means that the old response curves formerly used on Joides Resolution should be replaced by the new response curves.

3.3.2 Connect adjacent sections

In order to deconvolve two adjacent sections without breaks in magnetization, we have to deconvolve these two sections simultaneously. Two ways to link adjacent sections into successive sequence were considered and tested. One is to overlap data points of two data sets to produce one data set with length of two sections as if it were measured by a single pass-through, and deconvolve the data set by the same equations formerly used. The average ABIC in this case is calculated as -21.73 and S/N ratio is 552 (Table 2; case *k*). The results are shown on Fig. 11 (broken lines) for comparison with the results without connection (dotted lines).

Another is to calculate the magnetization by using the following vectors and matrixes for deconvolution, which joint two data sets to one smooth sequence of magnetization,

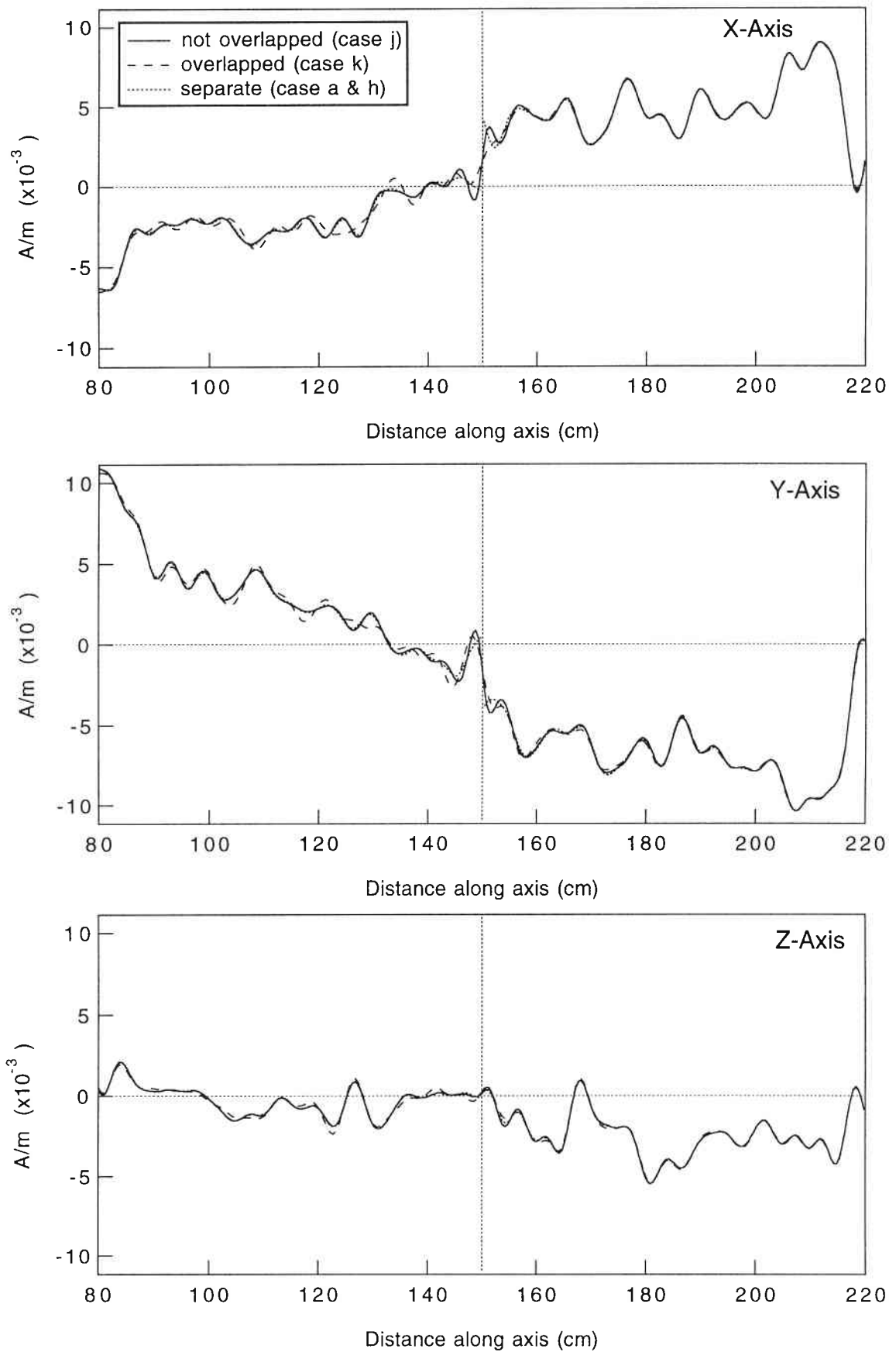


Fig. 11. The deconvolved magnetizations for the measurements of Sections 769B-7H6 and 769B-7H7 at 20 mT AF demagnetization are plotted. The connection of two adjacent sections are demonstrated by separate deconvolution (dotted lines), overlapping deconvolution (broken lines), and non-overlapping deconvolution (solid lines).

$$\mathbf{R}_{xx}^*(N, M) \rightarrow \begin{bmatrix} \mathbf{R}_{xx1}^*(N_1, M_1) & 0 \\ 0 & \mathbf{R}_{xx2}^*(N_2, M_2) \end{bmatrix}$$

$$\mathbf{D}_1^*(N, M) \rightarrow \mathbf{D}_1^*(M_1+M_2, M_1+M_2+2)$$

$$\mathbf{d}_x \rightarrow \begin{bmatrix} d_{x1} \\ d_{x2} \end{bmatrix}$$

$$\mathbf{m}_x \rightarrow \begin{bmatrix} m_{x1} \\ m_{x2} \end{bmatrix}$$

Here, matrix \mathbf{R} is composed of \mathbf{R}_1 and \mathbf{R}_2 , and two data sets d_1 and d_2 are dealt with separately, whereas matrix \mathbf{D} is continuous along with diagonal component, which means that the magnetization is considered as continuous between two adjoining sections. The average ABIC after deconvolution following above equation is -21.86 and S/N ratio is 529 (Table 2; case *j*). The average ABIC values separately obtained for 769B-7H6 (Table 2; case *a*) and 769B-7H7 (Table 2; case *h*) were averaged (Table 2; case *i*) as -21.91 and average S/N ratio is 507. Comparing these three cases, average ABIC is lowest for case *i* and highest for case *k* with minor differences. The S/N ratio is highest for case *k* and lowest for case *i*. The results are also shown on Fig. 11 (solid lines) for comparison. The difference between case *j*, and case *a* and *h* is very small except within about 5 cm of both sides of the junction at 150 cm. However, the results of case *k* (broken lines) is dissimilar to both cases from 120 cm to 155 cm. Thus we take the method of deconvolution without overlapping (case *j*) for the joint of two adjacent sections.

The results of deconvolution was also compared with the magnetization of cube samples taken from the working halves measured after 20 mT AF demagnetization (Fig. 12). The size of the cube sample along core is 2.4 cm and the measurement spacing is 10 cm, so both the resolution of the sample and measurement spacing are not enough for comparison with the results of deconvolution in detail. However, these two results seem to be in favorable agreement.

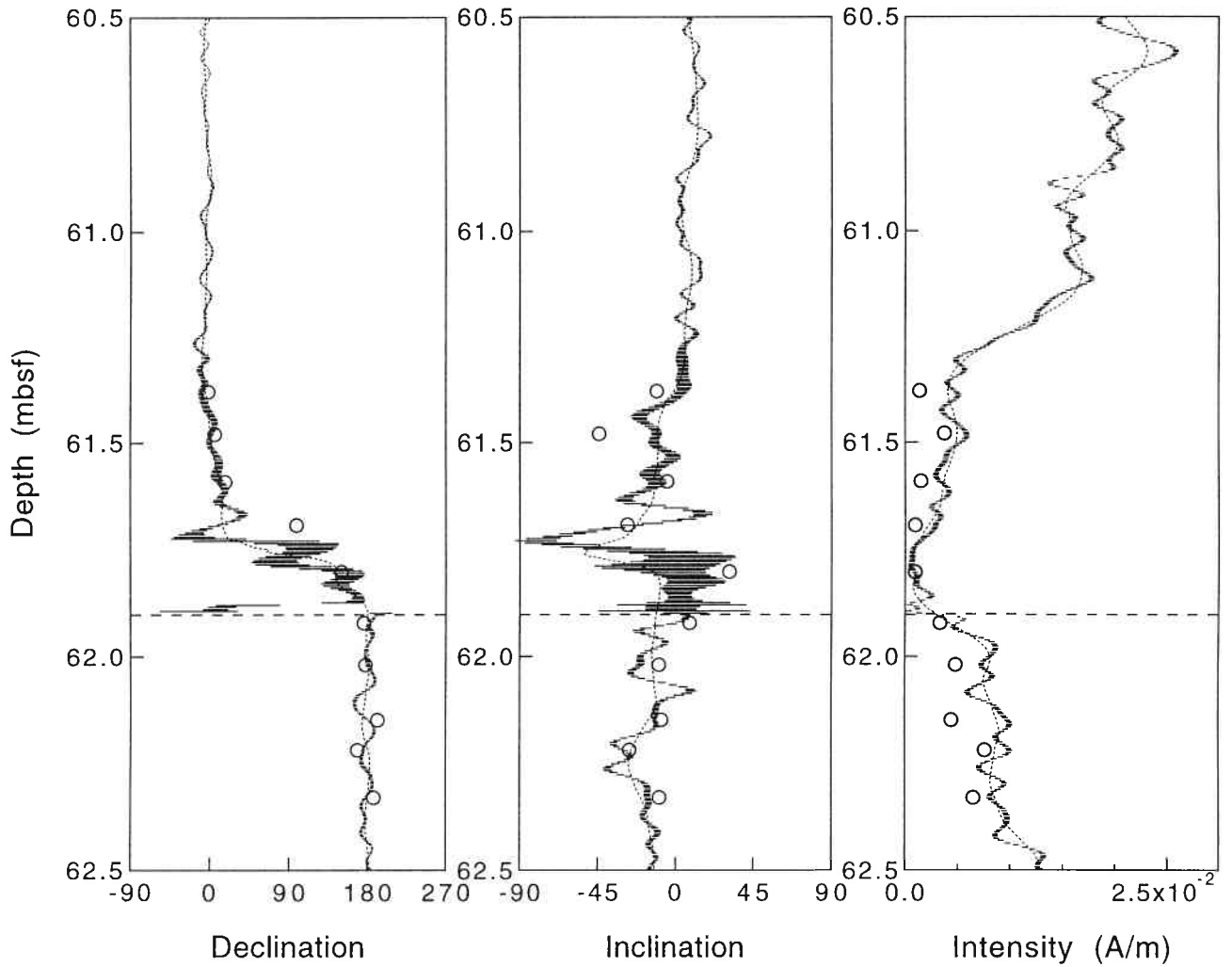


Fig. 12. Declinations, inclinations and intensities are plotted versus depth (mbsf) for magnetization of pass-through data of Sections 769B-7H6, 7 before deconvolution (broken lines), after deconvolution (dots with horizontal bars representing 95% confidence limits), and magnetization measured on cube samples of the same Sections (open circles). All the declination values are corrected to north by counter-clockwise rotation of 126°. Horizontal thick bars represent the boundary of two Sections.

The deconvolution was also conducted on samples from Hole 769A as cases n, o and p (Table 2). The results are nearly the same tendency as those of Hole 769B (cases i, j and k) that the average ABIC is minimum for separate deconvolution (case n) and maximum for overlapped case (case p), and S/N ratios are inverse. Declination, inclination and intensity for Holes 769A and 769B are calculated from x, y and z components and declination was corrected for the true north by the readings of multishot orientation tool (100° for 769A and 125° for 769B). The results show good agreement especially in declination (Fig. 13).

The deconvolutions for the data after 15 mT AFD were also conducted on both 769A and 769B samples (Fig. 14). Both of the results show almost the same fluctuation pattern as those for 20 mT except small reduction in intensity and minor changes in some places. Average ABIC values and S/N ratios (Table 2; case q-z) also show the same tendency as the results of 20 mT except S/N ratio for case y (701) is a little larger than that for case z (750).

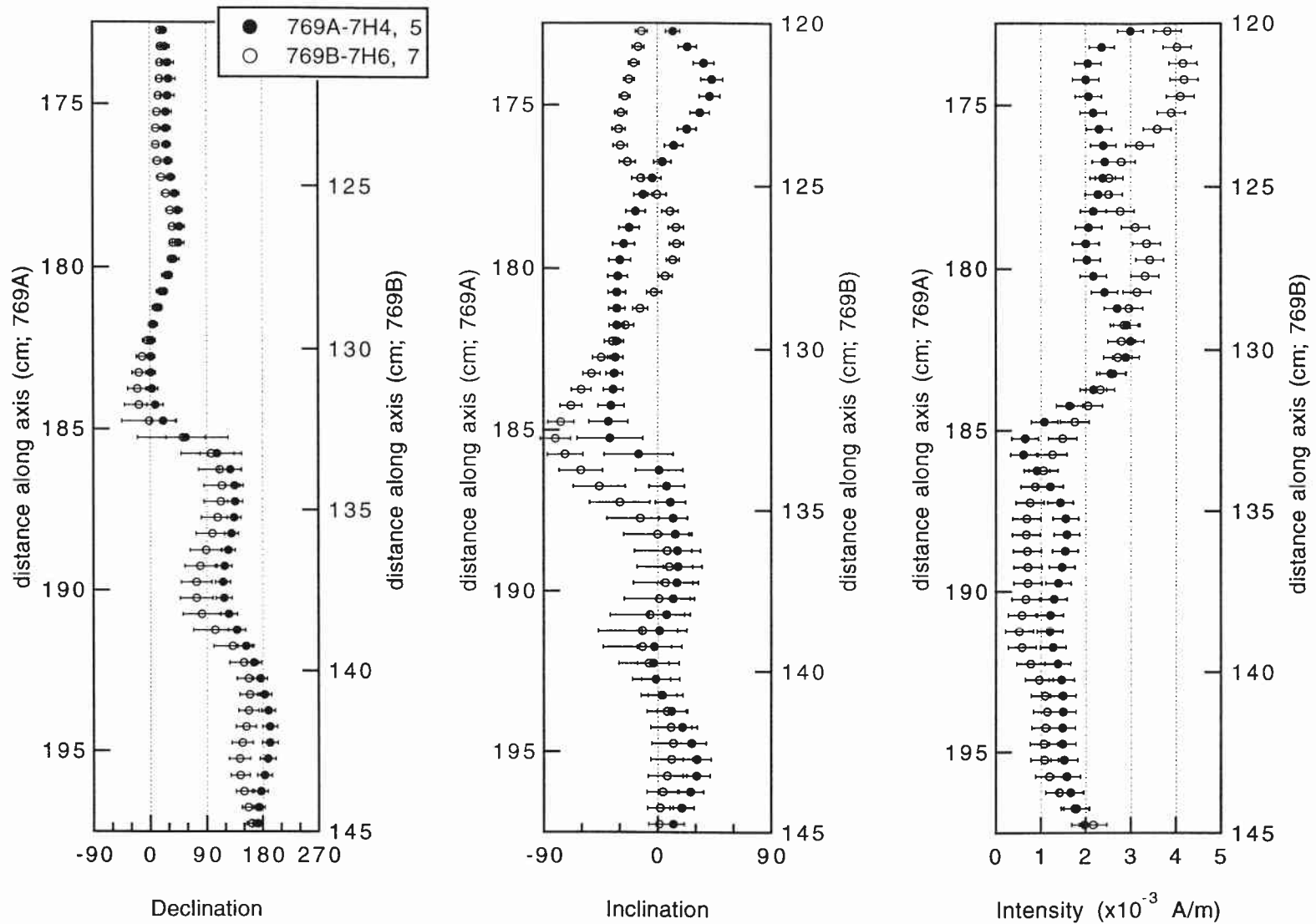


Fig. 13. Declination, Inclination and Intensity are plotted versus distance along axis for Holes 769A (solid circles) and 769B (open circles) with horizontal bars of 95% confidence limits.

(a) Sections 769A-7H4, 5

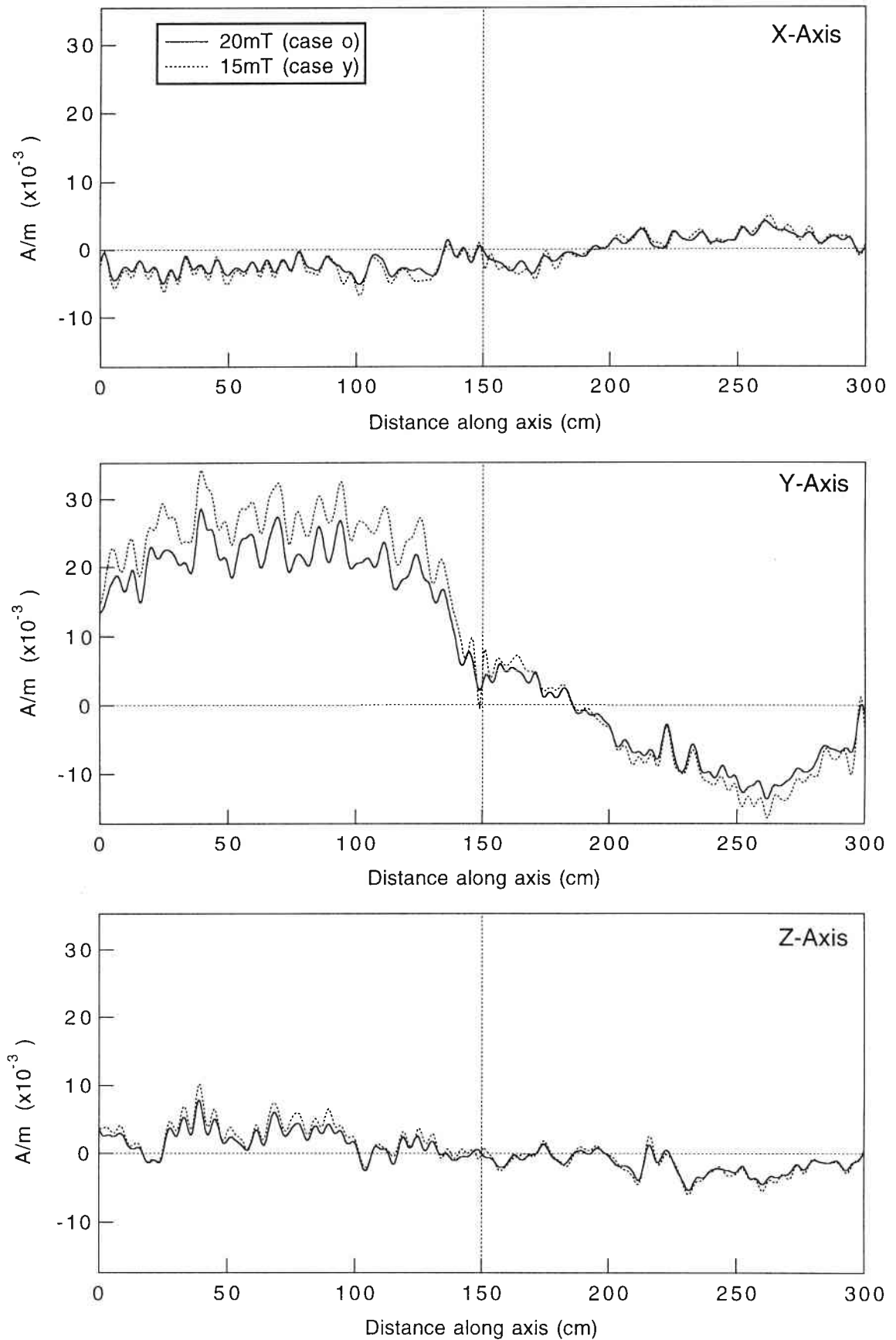


Fig. 14. (a) The magnetizations after deconvolution are plotted for Sections 769A-7H4 and 769A-7H4-7H5 after 20 mT (solid lines) and 15 mT (broken lines) AF demagnetizations. (b) Same as for Sections 769B-7H6 and 769B-7H6-7H7.

(b) Sections 769B-7H6, 7

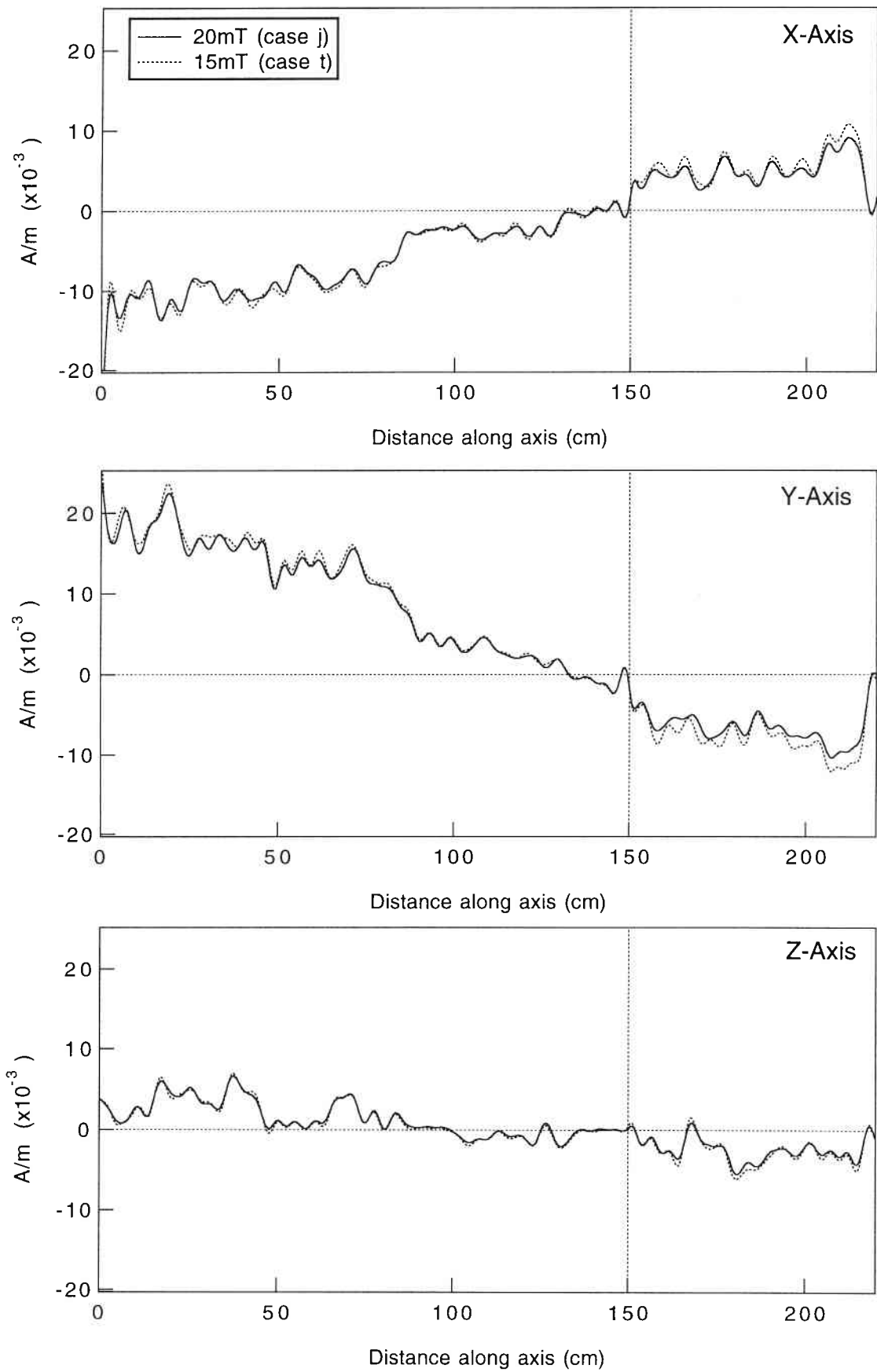


Fig. 14

4. Discussions

4.1 Stability and reliability of deconvolution

The deconvolution scheme developed here was investigated in detail in various conditions for the real data. The correct response (Table 2; case a) gave lower ABIC value than any other incorrect response curves. This is quite consistent with the principle of maximum likelihood and confirm that the correct sensor response curve is the best estimate. Although ABIC is larger, the deconvolution without cross terms of response curve are not so different from that of correct response. This may confirm the stability of the deconvolution with respect to response curve.

The noise estimated for the synthetic pass-through data are consistent with the noise superimposed before deconvolution. This may ensure that the deconvolution scheme is properly modeled as far as the noise distribute as a Gaussian.

4.2 How to connect adjacent sections?

Two ways of jointing adjacent sections were demonstrated in addition to the separate deconvolution. The overlapping method (e.g. case k) deconvolves the data as one succession and another method (e.g. case j) deconvolves by using response matrix composed of two separate blocks of columns representing sensor responses. The former method draw curves more smoothly across the junction, however, minimum ABIC is slightly larger than that of the latter method and the magnetization show meaningful discrepancy within 30 cm of the joint from the separately deconvolved results (e.g. case a and h). On the other hand, the difference between case j, and case a and h is very small except within about 5 cm of both sides of the junction. In an ideal condition, these three should agree with each other. The discrepancy may come from the disturbance of sediments on the cutting plane due to splitting and/or the heterogeneity of sediments residing from the beginning. There may also be a possibility

that the long-core is somewhat offset on the transporting plastic boat. In order to avoid effects both by disturbance of the sediments and by over-relaxation at the joint, the method to joint without overlapping data were used.

4.3 Noise source and resolution

There are several possible source of noise in the pass-through measurements. These are electromagnetic noise, the noise related to the positioning inaccuracy, lateral variation of the magnetization in the sample, and the noise introduced from the empirical response as in Eq. (2).

The noise level of the SQUID system is inversely proportional to square root of the frequency with low pass filter and the noise for 1 Hz is calculated as 5.22×10^{-12} , 4.94×10^{-12} and 6.74×10^{-12} (Am^2), in x, y and z axis, respectively. The estimated noise level of the measurement is 3.6×10^{-9} Am^2 , which is larger of the order of 3 than the electromagnetic noise. Thus the electromagnetic noise is negligible compared to the total noise level except the formerly mentioned spike noises caused by other electronics.

Although the long-core is transported by a stepping motor, the displacement from the proper position can possibly be introduced by an irregular extension of polyurethane rope due to heavy weight of the long-core samples. The displacement may be a noise source in combination with the gradient of the magnetization at the point. However, the residuals of deconvolution for the paleomagnetic data of two different AF demagnetization levels (15 mT, 20 mT) on section 124-769B-7H6 show very similar pattern in large scale (Fig. 15). This suggests that the residuals are not mainly produced by the source changeable from one measurement to another. All the cores tested yielded the same results, which can be interpreted that the noise source is mainly from noise in the response curves and/or lateral heterogeneity of the magnetization. The

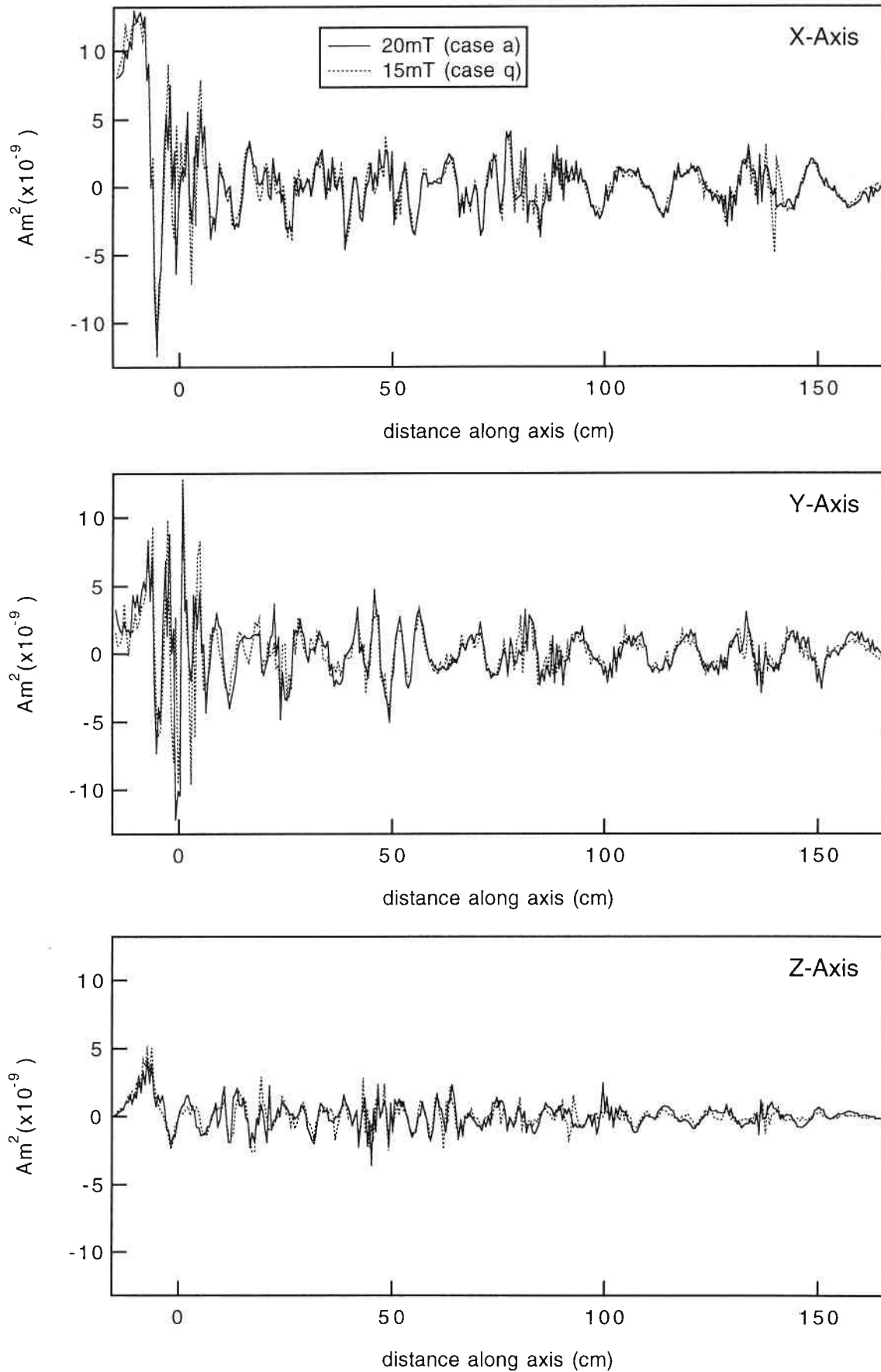


Fig. 15. The residuals of deconvolution between the SQUID output and moment calculated from the model magnetization on Section 769B-7H6 for AF demagnetization of 20 mT (solid lines) and 15 mT (broken lines). The dominant pattern is very similar to each other indicating that the contribution of positioning error (expected to randomly distribute) to the noise may be tribal.

residual can be reduced further by using more accurate response curves, however, the resolution may be finally restricted by lateral heterogeneity before encountering the limit of electromagnetic noise.

It can be expected that the outer part of the APC is more affected by drilling disturbance than the center of the core. Thus the U-channel sampling from the center of the APC is desirable to reduce the lateral heterogeneity. The U-channel sampling technique reduce the heterogeneity and enhances the spacial resolution, however, this has another problem that the magnetization records tend to be affected by heterogeneity, which may lead not to the global paleomagnetic field record but to the magnetization affected by local sediment artifacts such as bioturbation. In order to get reliable records of paleomagnetic field, the sample has to have a certain volume. In this sense, the measurement of APC sample is important for the study of the geomagnetic field.

The important point is that the resolution of deconvolved magnetization cannot be significantly improved by reducing the measurement spacing nor by reducing noise level as pointed out by Constable and Parker (1991). They suggested that the best way to enhance the spacial resolution of the magnetometer is to use smaller diameter pick-up coils for the measurement. A new high-resolution magnetometer with smaller diameter of pick-up coils (a modified 4.2 cm access model 755-R with two sets of SQUIDS) has recently been developed by 2G, which enable us measurements of U-channel (20 mm x 20 mm of cross section) with spacial resolution of 4 cm (Nagy and Valet,1993; Weeks et al.,1993). Deconvolution of the data further increased the resolution to about 2 cm.

The SQUID magnetometer on Joides Resolution (model 760R) has much larger spacial resolution (~15 cm), however, the resolution of the magnetization was shown to be reduced to about 2 cm in maximum by deconvolution. As far as we use the existing magnetometer for the measurement of archive half, the deconvolution presented here can be an

important tool to raise the resolution of the paleomagnetic records. There is an advantage of pass-through measurement on Joides Resolution that the measurements are usually carried out within a day typically several hours after the recovery of APC samples. This may rule out the possibility of alteration cause after the recovery of the samples. The deconvolution can be used for initial scan for the records of geomagnetic reversals, short events and excursions, and assessment for subsequent sampling. This can also be a powerful tool for the detailed study of geomagnetic secular variations, because pass-through measurement may be the only way to get continuous records from ODP sediments due to the restricted sampling strategy of ODP.

5. Conclusions

The ABIC minimizing deconvolution was developed for long-core paleomagnetic data of ODP sediments. The deconvolution scheme was applied to the pass-through data of APC samples from Holes 769A and 769B of Leg 124 and the results are in favorable agreement with each other especially in declination. The deconvolution could enhance the resolution from the former spacial resolution of pick-up coils (~ 11 cm) to the spacial resolution of about 2 cm in maximum for the data measured at interval of 5 mm.

The noise estimation is quite consistent with the amplitude of noise added before deconvolution for the synthetic data. This ensures that the ABIC minimization deconvolution is working well as far as the assumption that the noise distribute as a Gaussian holds. Various test with respect to response curves revealed that the old response is not applicable for the deconvolution, however, the cross term seems not to play an important role in the deconvolution.

Main noise source of the pass-through data may be lateral variation of the magnetization and noise in the empirical response curve. The noise

of the empirical response curve can be reduced in some extent, however the spacial resolution of the measurement is essentially limited by the lateral variation of the magnetization due to bioturbation and/or drilling disturbance. Recently developed magnetometer for u-channel samples with smaller diameter pick-up coils strongly enhanced the spacial resolution to about 4 cm (Nagy and Valet, 1993; Weeks et al., 1993). Although the new magnetometer is the powerful tool for the detailed paleomagnetic study, the deconvolution scheme for the ODP pass-through measurement system presented here can play an important role in the detailed paleomagnetic study for its high productivity and prompt measurement free of alteration.

References

- Akaike, H., Likelihood and the Bayes procedure, in *Bayesian Statistics*, pp. 143-166, ed. M. H. D. J. M. Bernardo D. V. Lindley and A. F. M. Smith, Univ. Press, Valencia, Spain, 1980.
- Akaike, H., On the selection of prior distribution and its application, in *Bayesian statistics and its application*, pp. 81-98, ed. Y. Suzuki and N. Kunitomo, Tokyo Univ. Press, Tokyo, 1989.
- Constable, C. and R. Parker, Deconvolution of long-core palaeomagnetic measurements - spline therapy for the linear problem, *Geophys. J. Int.*, **104**, 453-468, 1991.
- Dimri, V., *Deconvolution and inverse theory, Application to geophysical problems*, Elsevier, Amsterdam, 1992.
- Dodson, R., M. Fuller and W. Pilant, On the measurement of the magnetism of long cores, *Geophys. Res. Lett.*, **1**, 185-188, 1974.
- Nagy, E. A. and J.-P. Valet, New advances for paleomagnetic studies of sediment cores using u-channels, *Geophys. Res. Lett.*, **20**, 671-674, 1993.
- Oda, H. and H. Shibuya, Deconvolution of whole-core magnetic remanence data by ABIC minimization, *J. Geomag. Geoelectr.*, **46**, 613-628, 1994.
- Okamoto, Y., *Inverse problem and its solution*, ed. T. Musha, Ohm Co., Tokyo, 1992 (*in Japanese*).
- Press, W. H., S. A. Teukolsky, W. T. Vetterling and B. P. Flannery, *Numerical Recipes in Fortran, The Art of Scientific Computing*, 2nd ed., Cambridge University Press, New York, 1992.
- Rangin, C., E. A. Silver, M. T. von Breyman et al., *Proc. ODP, Init. Repts.* **124**, 1990.
- Tamura, Y., T. Sato, M. Ooe and M. Ishiguro, A procedure for tidal analysis with a Bayesian information criterion, *Geophys. J. Int.*, **104**, 507-516, 1991.
- Tarantola, A., *Inverse problem theory, Methods for data fitting and model*

parameter estimation, Elsevier, Amsterdam, 1987.

Togawa, H., *Matrix calculations*, Ohm Co., Tokyo, 1971 (*in Japanese*).

Tsunakawa, H., Bayesian approach to smoothing palaeomagnetic data using ABIC, *Geophys. J. Int.*, **108**, 801-811, 1992.

Weeks, R., C. Laj, Endignoux, L., M. Fuller, A. Roberts, R. Manganne, E. Blanchard and W. Goree, Improvements in long-core measurement techniques: applications in palaeomagnetism and palaeoceanography, *Geophys. J. Int.*, **114**, 651-662, 1993.

Part II : High resolution paleomagnetic records of
Brunhes/Matuyama polarity transition from
ODP Leg 124 (Celebes and Sulu Seas)

Abstract

High quality and high resolution record of Brunhes/Matuyama polarity transition was obtained from deep-sea sediments of ODP Leg 124 drilled in the Celebes and Sulu Seas. Advanced piston core (APC) samples with high magnetization intensity and high sedimentation rate were recovered from ODP Leg 124. Pass-through measurements were conducted at intervals of 5 mm on APC samples across the Brunhes/Matuyama polarity transition for Holes 767B, 769A and 769B. A short normal reversal record prior to the Brunhes/Matuyama transition was also obtained from Hole 768B. These pass-through data were analyzed by ABIC-minimizing deconvolution.

The results from the three holes are in good agreement, especially between two Holes of Site 769, 769A and 769B, which are about 100 m apart. VGP shows eastward swing to north Atlantic just after the equator crossing. Relatively stable intermediated VGP positions were recognized before and after the transition. The intermediate VGP positions after the reversal agree well among the three holes and persisted for about 2000-3000 yr. The paleomagnetic cube samples were also taken from the polarity transition zones and their VGP positions are in good agreement with the pass-through data after deconvolution. These intermediate VGPs can be well correlative to the sediment record of Brunhes/Matuyama boundary from the Boso Peninsula. The longitudinal distribution of transitional VGPs support the idea of preference of the site and VGP distribution $\pm 90^\circ$ away from the site. The relative intensity was also estimated and 4000 yr interval of low intensity zone across the reversal boundary was recognized.

1. Introduction

1.1. Transitional field study

The study to understand the behavior of the geomagnetic field at the time of polarity transition started by studying deep-sea sediment cores (Opdyke et al., 1973; Kawai and Otofujii, 1976; Hammond et al., 1979). After these pioneering works, extensive works have been done on deep-sea sediments of Deep Sea Drilling Project (DSDP) and Ocean Drilling Program (ODP) (Clement and Kent, 1986; Valet et al., 1989) and other piston cored samples (Clement et al., 1982; Clement and Kent 1984, 1991; Theyer et al., 1985). The sediments exposed on land were also studied both of marine sediments (Boso Peninsula; Niitsuma, 1971) and lacustrine sediments (Lake Tecopa; Hillhouse and Cox, 1976). The marine sediments from the Mediterranean area (Tric et al., 1991; Linssen, 1988; Valet et al., 1988; Laj et al., 1988) has been increasing the number of geomagnetic reversal records.

The volcanic rocks can be a good medium for recording transitional field of geomagnetic reversals by the benefit of stability of thermoremanent magnetization (TRM). The Steens mountain (Oregon, North America) record of a Miocene reversal is the most detailed record measured on volcanic lava sequences (Mankinen et al., 1985; Prévot et al., 1985). They studied paleointensity during geomagnetic reversal as well as the transitional field directions (Prévot et al., 1985). There have also been reports of geomagnetic reversal records on volcanic lava sequences from Tahiti (Chauvin et al., 1990; Roperch and Duncan, 1990), Iceland (Dagley and Lawley, 1974; Shaw, 1975) and Hawaii (Bogue and Coe, 1982, 1984; Hoffman, 1991). The transitional field of geomagnetic reversal was also reported from intrusive rock cooled during a geomagnetic reversal (Dodson et al., 1978).

Because successive volcanic activity with a lot of lava sequences is needed to catch the rapidly changing transitional field in detail, the

sites of volcanic records of young geomagnetic reversals are mainly restricted to active hot spot area. For this reason sediments have advantage for the transitional field study to cover geographically wide area, although the magnetization of volcanic rocks are more stable and reliable than sediments.

1.2. Evolution of transition field models

The geomagnetic polarity reversal is the most dynamic feature of the Earth's magnetic field, and a proper documentation may therefore be expected to yield useful ideas about the generation of the geomagnetic field. In modeling reversal transitional field we have to start with the phenomenological model to describe the global character of the field before constructing dynamo models that can explain polarity reversal theoretically. Many attempts have been made to model the global nature of the reversal transitional field. The transitional field models has been developed as the quality and quantity of the record increases.

Hillhouse and Cox (1976) assumed that the non-dipole field can be described as the sum of a westward drifting and a standing component, and accepted the estimate of 4600 yr for the duration of a reversal, obtained from records in deep-sea cores. They calculated that, if the usual non-dipole field remained unchanged during a polarity reversal, its westward drifting component should cause large longitudinal swings of the VGP which would be clearly visible in the records. The absence of such characteristics in the Lake Tecopa record where transitional directions are confined along a great circle, led Hillhouse and Cox to suggest that a standing component of the field is present during the main part of the transition, while the dipole field decreases to zero and regenerates with opposite polarity. This has been called the 'standing field' model for reversal.

A completely different conclusion was reached by Hoffman (1977)

who suggested that the reversals originate in a well-localized region of the core and subsequently "floods" into other regions. An important aspect of this approach was the recognition that this process would lead to zonal transitional fields which involved simultaneous vertical inclinations in successive bands of latitude. The VGP path passes near to the site, or near to the antipode of the site ('near' or 'far sided' path). Later Hoffman (1981) pointed out that the standing field and flooding field models predict different field behavior associated with sequential field reversals at the same site that is theoretically distinguishable. Specifically, if a standing field predominates during the transition and remains unchanged for times longer than the interval separating two successive reversals, the intermediate field geometries should be identical (independent of the sense of the transition). Widely different intermediate directions are, on the contrary, expected if a flooding field controls the reversal process.

The observation that zonal harmonics seemed to dominate transitional fields (Fuller et al., 1979) led Williams and Fuller (1981) to develop a mathematical model in which dipole component decay to zero and grow in the opposite sense, with the variation in dipole field energy fed into the lower order zonal harmonics. Valet et al. (1986) measured the sediment records of Miocene reversals from Crete and reported periodic oscillations in the angular displacement from the pre-reversal dipole field direction, which is similar to the secular variation seen when the field is not reversing. This led Williams et al. (1988) to model the reversing geomagnetic field as zonal harmonics with a drifting non-dipole field. The VGP paths produced by this model sweeps around the surface of the Earth.

1.3. Preferred longitudinal bands and clusters of VGP

Recently long-lived dipolar nature of the geomagnetic field during

polarity transition has been discussed. Tric (1991) pointed out nearly dipolar geometry for the reversal transitional field through compilation of recent geomagnetic reversal records from sediments. Clement (1991) also suggested the longitudinal confinement of VGP paths, through the Americas or through Asia and Australia, for the Brunhes/Matuyama polarity reversal from 21 records of sediments and volcanic rocks. The long-lived preferred longitudinal bands of VGP paths are discussed in correlation with the preference of p-wave velocity low and pole-ward flow at the surface of the outer-core by Laj et al. (1991). This leads to the speculation that the long lived states of the physical (thermal) condition at the core mantle boundary (CMB) controls VGP paths at the time of the geomagnetic field reversal.

Valet et al. (1992) rejected the idea of preferred longitudinal bands by chi-square test on the data base from sediment and volcanic records younger than 12 Ma. Other statistical analyses on reversal VGPs suggested that the preference of VGP paths is acceptable (circular statistics: Laj, 1992a, 1992b; statistical simulation on rotating sectors: McFadden et al., 1993). However, it is pointed out that the preference of VGP longitude can also be explained by the preference of site longitudes and VGPs $\pm 90^\circ$ away from the sites.

The clustering of transitional VGPs over western Australia and southern part of South America are reported on volcanic rock records of recent reversals (Hoffman, 1992). Brown et al. (1994) also reported Brunhes/Matuyama transition record from Chilean Andes which shows clustering over Australia. These may indicate the long-lived inclined dipolar states during reversal. On the contrary, Prévot and Camps (1993) compiled 400 intermediate poles from 121 volcanic records of excursions and reversals less than 16 Ma, which does not confirm VGP clusters and rejected the idea of lowermost mantle control on the transitional fields.

1.4. This study

Although transitional records of geomagnetic reversals have been studied intensively for the past two decades, the nature of geomagnetic field during polarity transitions is still in debate. The reliable transitional records of each distinct polarity transition with enough global distribution of recording sites are strongly required for better understanding of geomagnetic reversal.

ODP Leg 124 were drilled in the Celebes and Sulu Seas where distribution of reversal sites are sparse and recovered stable and high in intensity paleomagnetic records with high sedimentation rates. The reversal records of advanced hydraulic piston core (APC) samples were obtained from the Brunhes/Matuyama transition as multiple records. Pass-through measurements of long-core samples on-board and paleomagnetic measurements on discrete samples were performed. Pass-through data measured at intervals of 5mm were analyzed by ABIC minimizing deconvolution developed in Part I. The results from three Holes 767B, 769A and 769B show good agreement, especially between 769A and 769B. The details of geomagnetic field during the Brunhes/Matuyama polarity transition is discussed.

2. Geological setting and sample descriptions

The Sulu and Celebes Seas are western Pacific marginal basins lying to the southeast of the South China Sea. Five sites were drilled in the Celebes and Sulu basins during ODP Leg 124 (Fig. 1; Rangin and Silver, 1990). Unusually detailed magnetostratigraphic records of Pleistocene time were obtained from advanced piston core (APC) samples of Sites 767, 768 and 769 (Rangin and Silver, 1990). Archive halves of 1.5m-long APC cores and discrete cube samples taken from working halves of these three Sites were used for the study (Fig. 1). All the samples subjected to the study are listed in Table 1.

2.1. Celebes Sea (Site 767)

Site 767 (4.79°N, 123.50°E) is located approximately 100 km from the Cotabato Trench in the Celebes Sea (Fig. 1). Three holes were drilled at a depth of 4905 m and 787 m thick sediments were recovered until basaltic basement was encountered. The sediment sequence recovered at this site ranges in age from late Middle Eocene to Holocene. Sediment at this site is deposited below carbonate compensation depth (CCD). Four distinct lithologic units are recognized at this site (Rangin and Silver, 1990).

The magnetic reversal sequence is well determined in all oriented APC samples (Fig. 2). Due to the coring disturbance in XCB and RCB cores and low inclinations of paleomagnetic results, no magnetic reversals can be recognized below 90.5 mbsf at this site. The Brunhes/Matuyama polarity transition (Sections 767B-6H1, 6H2) was recorded in the Unit I sediment (Fig. 2).

Unit I is a 56.8 m-thick Peistocene-Holocene hemipelagic volcanogenic clayey silt with rare calcareous turbidite layers and sparsely interbedded volcanic ashes (Fig. 2). The sediment is slightly to highly bioturbated, resulting in color mottling and a lack of

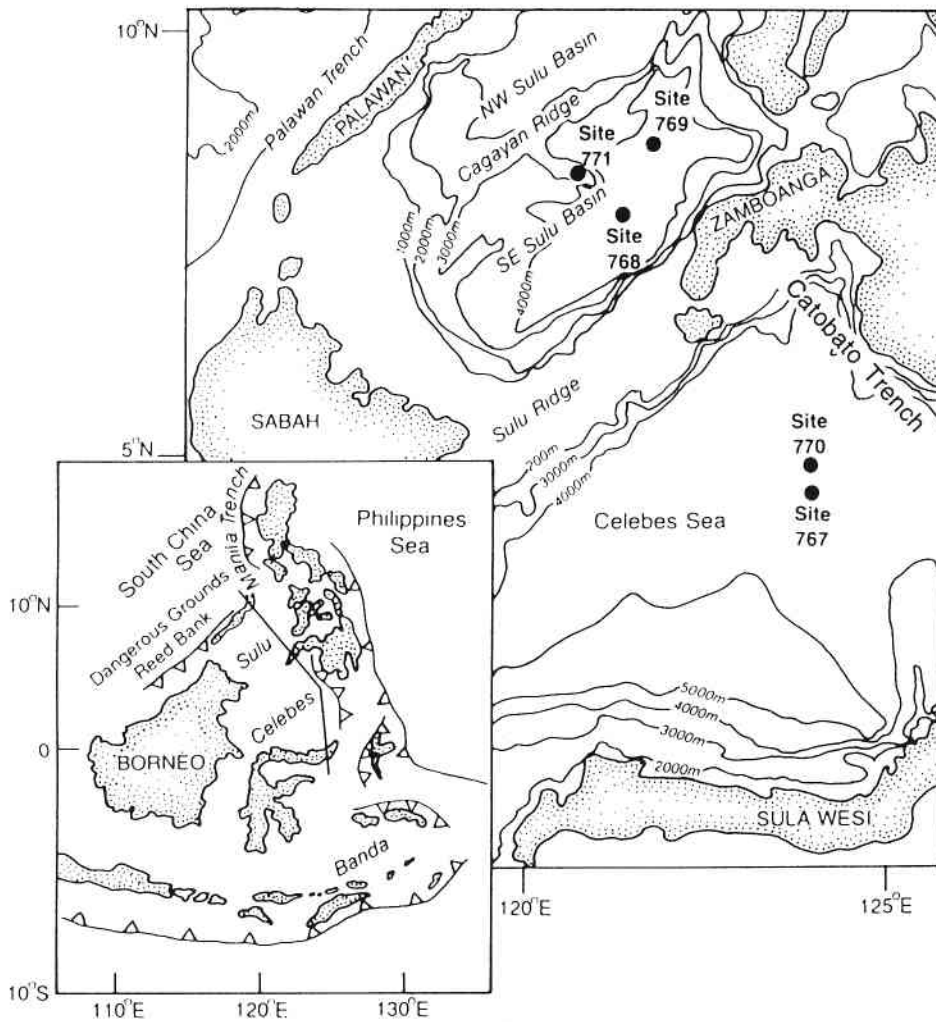


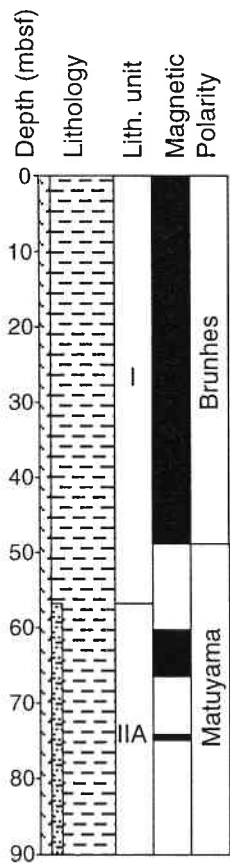
Fig. 1 Location map of drilled sites during Leg 124. APC samples from Sites 767, 768 and 769 are used for the study. Modified from Rangin and Silver (1990).

Table 1. Advanced piston core (APC) samples used for the study are listed. The pass-through measurement and cube samples used for the study are indicated by circles. Orientations are determined by the readings of Eastman Whipstock multishot tool (MS) and by averaging non-transitional field directions (fit).

Hole	Water depth (m)	Latitude (°N)	Longitude (°E)	Section	Pass-through	Cube	Orientation (°)	
							MS	fit
767B	4905	4°47.47'	123°30.21'	6H1, 2	○	○	328	137
768B	4385	8°00.05'	121°13.19'	9H4, 5	○	○	10	-3
769A	3644	8°47.14'	121°17.65'	7H4, 5	○	-	100	100
769B	3644	8°47.12'	121°17.68'	7H6, 7	○	○	125	126

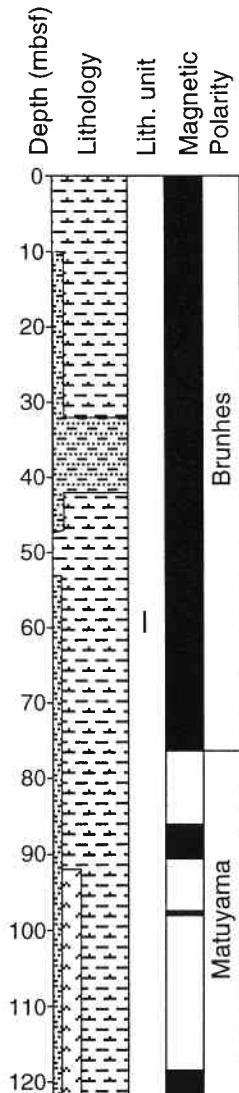
Celebes Sea

Site 767 (4905m)

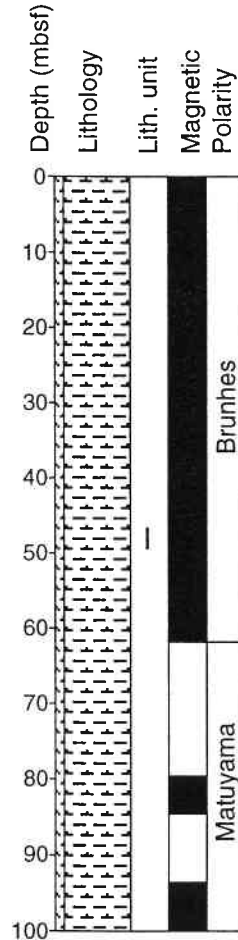


Sulu Sea

Site 768 (4385m)



Site 769 (3644m)




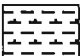

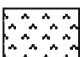
-  Clayey silt
-  Foraminifer-nannofossil marl
-  Calcareous turbidite
-  Volcanic fine ash/tuff

Fig. 2. Schematic stratigraphic columns for upper parts of Sites 767, 768 and 769. Lithological units are specified by roman numbers. Magnetic polarities identified are indicated by black (normal polarity) and white (reversed polarity).

preservation of primary sedimentary structures. The silt component of the clayey silt is primarily volcanic ash, including glass shards, pumiceous glasses, rock fragments, feldspar, and hornblende. Biogenic grains form only a minor component of the clayey silt, with siliceous material more abundant than the scarce calcareous grains.

As the Section 767B-6H1 is top of the Core, upper most part is disturbed by drilling (Plate 1). No significant sediment structure was reported for Sections 767B-6H1 and 767B-6H2 (Rangin and Silver, 1990). However, there is a brown colored band from 65-70 cm, which can be seen as a high of magnetization intensity zone.

2.2. Sulu Sea

Site 768 and 769 were drilled in the Sulu Sea at a depth of 4383 m and 3643 m. Site 768 lies in the deeper part of the SE Sulu basin and Site 769 lies on the flank of the Cagayan ridge. Late Pliocene to Pleistocene sediments of Sites 768 and 769 deposited above CCD and contains large amount of foraminifera and nannofossils.

2.2.1. Site 768

Site 768 (8.00°N, 121.22°E) was drilled in the SE Sulu Sea and the water depth at this site is 4384.4 m. The sedimentary section overlying the basaltic basement at Site 768 is 1046.6 m thick ranging from Early Miocene to Holocene. The section can be divided into five lithologic units. The paleomagnetic records of the APC cores were generally excellent except for the lower part of the two Reunion Subchrons. The Brunhes/Matuyama polarity transition was recorded in Unit I sediments (Sections 124-768B-9H4 and -9H5).

Unit I is spanning 0-122.5 mbsf and consists of thin- to thick-bedded marl with varying proportions of nannofossils and foraminifers and sparse thin beds of volcanic ash (Fig. 2). The marl beds are greenish

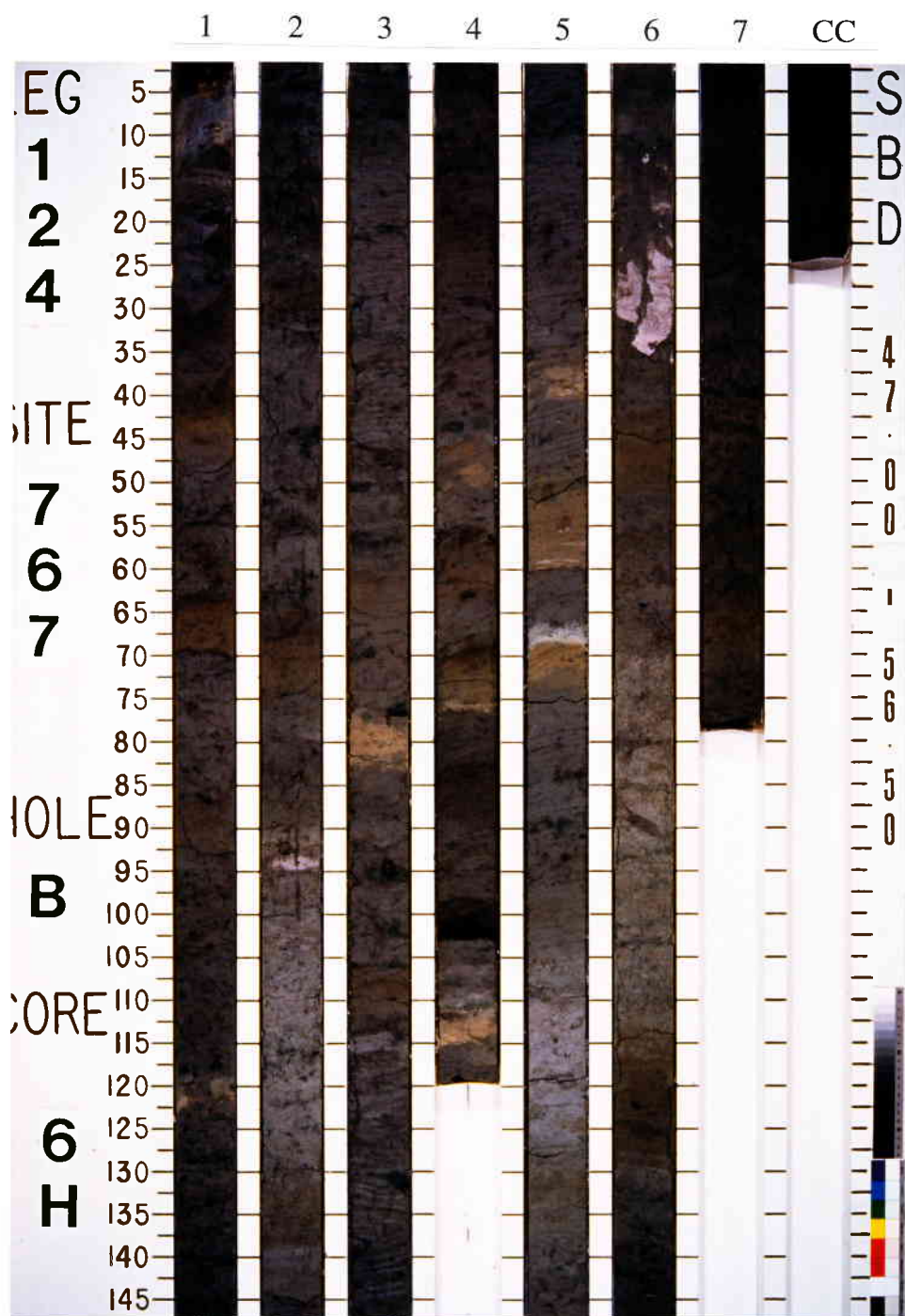


Plate 1. Photograph of Core 124-767B-6H taken on board. Sections are 1-7, and CC (core catcher) from left to right. The boundary of Brunhes/Matuyama polarity transition was recognized at 21 cm of Section 2. Sections 124-767B-6H1 and 124-767B-6H2 are used for the study of Brunhes/Matuyama polarity transition.

gray to gray and are mostly massive and bioturbated. Planktonic foraminifers and fewer benthic foraminifers as well as nannofossils, and clay are the principal components of the marl. The minor components are siliceous biogenic material (spicules, diatoms, radiolarians, and silicoflagelates), bioclasts, and volcanic detritus (glass, rock fragments, feldspar, and hornblende).

Most of the marl is interpreted as pelagic sediment because it is predominantly massive and bioturbated. Deposition must have taken place above the CCD, which currently is deeper than the water depth (4384.4 mbsf) at Site 768. However, some thin to medium beds display normally graded bedding, planar lamination, and rare convolute and cross lamination indicating deposition by turbidity currents.

Bioturbation is only present in the upper portion of these beds. The proportion of recognized turbidite beds is 7% of the thickness of Unit I, but this is a minimum estimate because the structures that display possible deposition by density currents may have been destroyed by bioturbation or drilling disturbance (Rangin and Silver, 1990).

Fining upward sequence was recognized in Section 768B-9H4 with sharp base contact at 39 cm (Plate 2). Fining upward sequences were also recognized in Section 768B-9H5 below 80 cm, however, all the samples were collected above these sequences and pass-through measurement were not conducted. After the pass-through measurement and sampling of paleomagnetic cubes, it was recognized that Section 768B-9H4 covers the short excursion like precursor of the Brunhes/Matuyama transition and the main transition of Brunhes/Matuyama seems to be around the top of Section 768B-9H4.

2.2.2. Site 769

Site 769 (8.79°N, 121.29°E) was drilled on the southeastern flank of Cagayan ridge at 3643 m water depth and 376.9 m-thick sedimentary

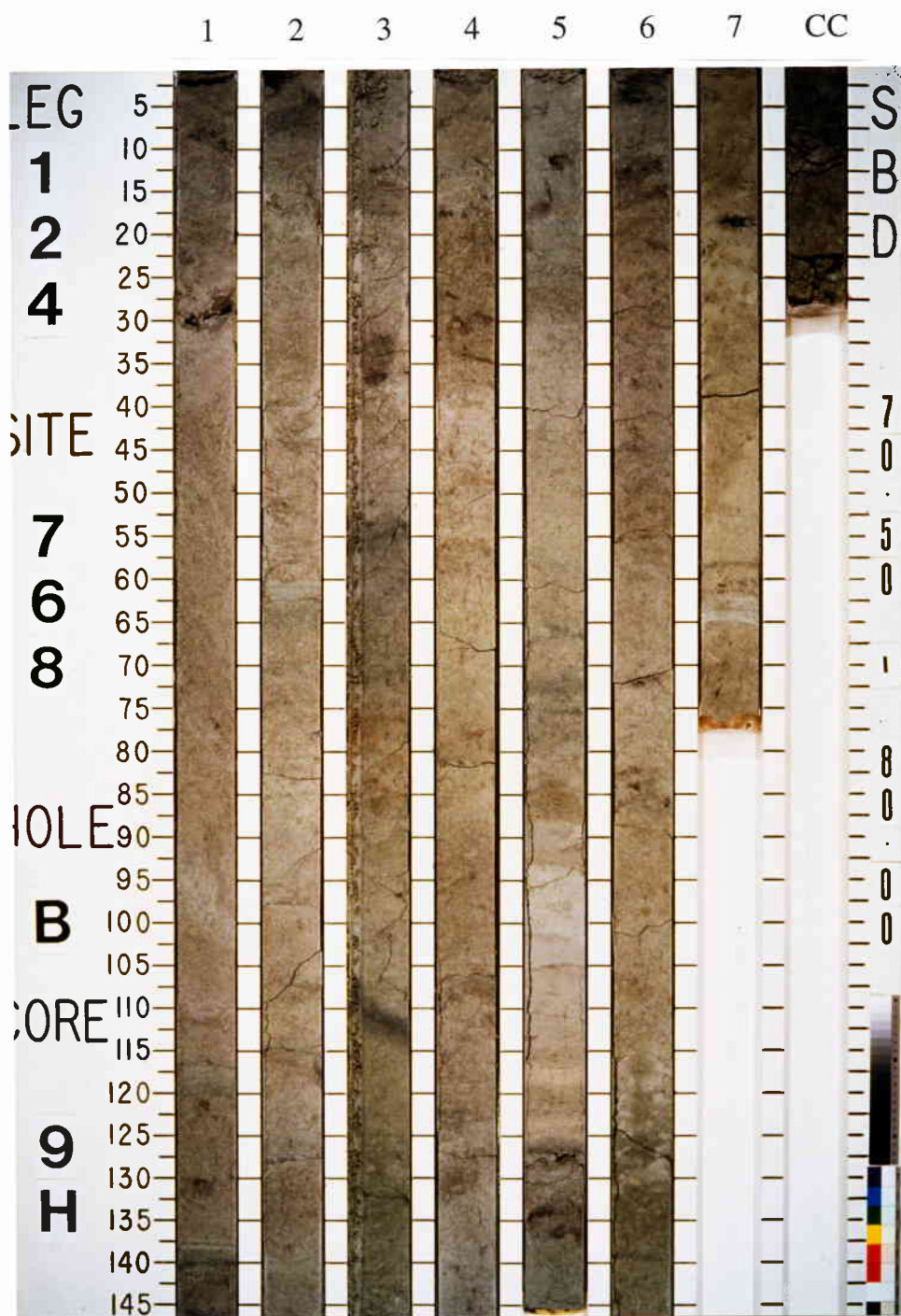


Plate 2. Photograph of Core 124-768B-9H taken on board. Sections are 1-7, and CC (core catcher) from left to right. Sections 124-768B-9H4 and 124-768B-9H5 are used for the study. Brunhes/Matuyama polarity transition was not determined precisely, because the pass-through measurement at intervals of 5mm was not conducted on Section 3. The boundary is from 120 cm of Section 3 to top (3 cm) of Section 4. A short reversal precursor to Brunhes/Matuyama polarity transition was recognized from 70 cm to 110 cm of Section 4.

and volcanoclastic strata was recovered. Three holes were drilled at this site. The age of the sediments range from late Early Miocene or older to Holocene. The section can be divided into three lithologic units.

The quality of paleomagnetic data collected at Site 769 was generally good in APC cores. All the widely accepted magnetic reversal boundaries above the bottom of the upper part of the Reunion Subchron were recognized. Results indicate that the sedimentary column in Cores 124-769B-1H to -24H has accumulated since 9.4 Ma, with a few breaks in deposition. The Brunhes/Matuyama transition was obtained from Unit I; Sections 769A-7H4 and -7H5 for Hole 769A, and Sections 769B-7H6 and -7H7 for Hole 769B. Holes 769A and 769B were drilled about 100 m apart.

Unit I is formed by pelagic to hemipelagic marl with nannofossils and foraminifers deposited above CCD. The marl contains clay, abundant nannofossils and planktonic foraminifers, scattered benthic foraminifers, volcanic glass, and varying amounts of siliceous biogenic material (spicules, diatoms, and radiolarians). Minor thin beds of volcanic ash and turbidites of foraminiferal ooze are also present within the unit. The marl is gray to greenish gray in color and is bioturbated throughout with faint laminations preserved in places. Bioturbation is expressed by dark gray mottling and by 2 to 3 mm-thick burrows that are filled by ash.

In the upper part of the unit (Cores 124-769B-1H to -7H), some thin-to-thick, upward-fining beds of foraminifer ooze are present. The lower-bounding contacts of these layers are sharp and the upper limits are transitional with the marl. These layers are interpreted as turbidite deposits. The deposits of Unit I show significant soft-sediment deformation, which affects parts of the section from about 15 mbsf to the bottom of the unit. The deformation is commonly expressed as slightly to steeply inclined lithologic contacts, convolute

lamination, and possible water escape structures. These features imply that episodic small-scale slumping has affected significant portions of Unit I, but much of the section nevertheless remains intact (Rangin and Silver, 1990).

The sediment of Sections 769A-7H4 and 769A-7H5 is highly bioturbated massive marl (Rangin and Silver, 1990). The marl mainly composed of nannofossils, foraminifers and clay. Bioturbation is evidenced by large mottles of dark gray and olive gray marl interpreted as burrow fills (Plate 3). The sediment of Sections 769B-7H6 and 769B-7H7 is massive nannofossils marl with foraminifers extensively bioturbated (Plate 4). These samples do not show normally grading upward sequence nor structures indicating the presence of slumping, which were reported some other samples from Unit I.

2.3. Core Orientation

Orientation of the APC samples were determined with an Eastman Whipstock multishot tool, which is rigidly mounted onto the core barrel. The Eastman-Whipstock tool consists of a magnetic compass and a camera. The battery-operated camera photographs continuously at prescribed intervals from 0.5 to 2 minutes from the time it leaves the ship's deck. At the bottom of the hole, the core barrel is allowed to rest for sufficient time (2-8 min.) to settle the compass needle and make sure that several photographs are taken before the corer is shot into the sediment. The photographs used for orientation are those taken just prior to shooting the core barrel into the sediment. The two perpendicular gravity sensor are also included and allow the azimuth and dip of the hole to be measured as well as the azimuth of the APC core double orientation line. The core orientation (east of north) obtained are listed in Table 1. The orientations calculated by averaging declination of non-transitional field direction (fit) are also listed for

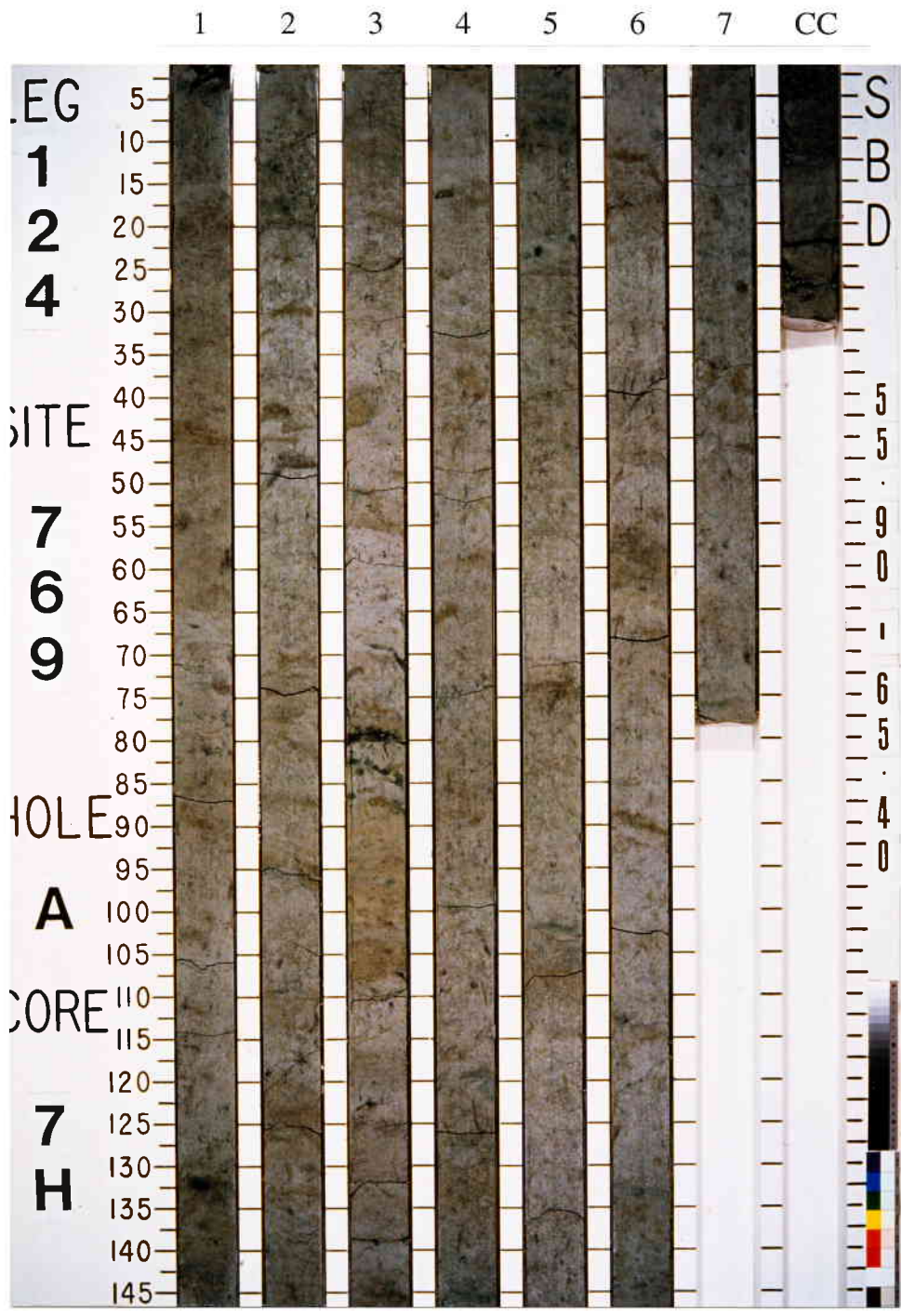


Plate 3. Photograph of Core 124-769A-7H taken on board. Sections are 1-7, and CC (core catcher) from left to right. The boundary of Brunhes/Matuyama polarity transition was recognized at 35 cm of Section 5. Sections 124-769A-7H4 and 124-769A-7H5 are used for the study of Brunhes/Matuyama transition.

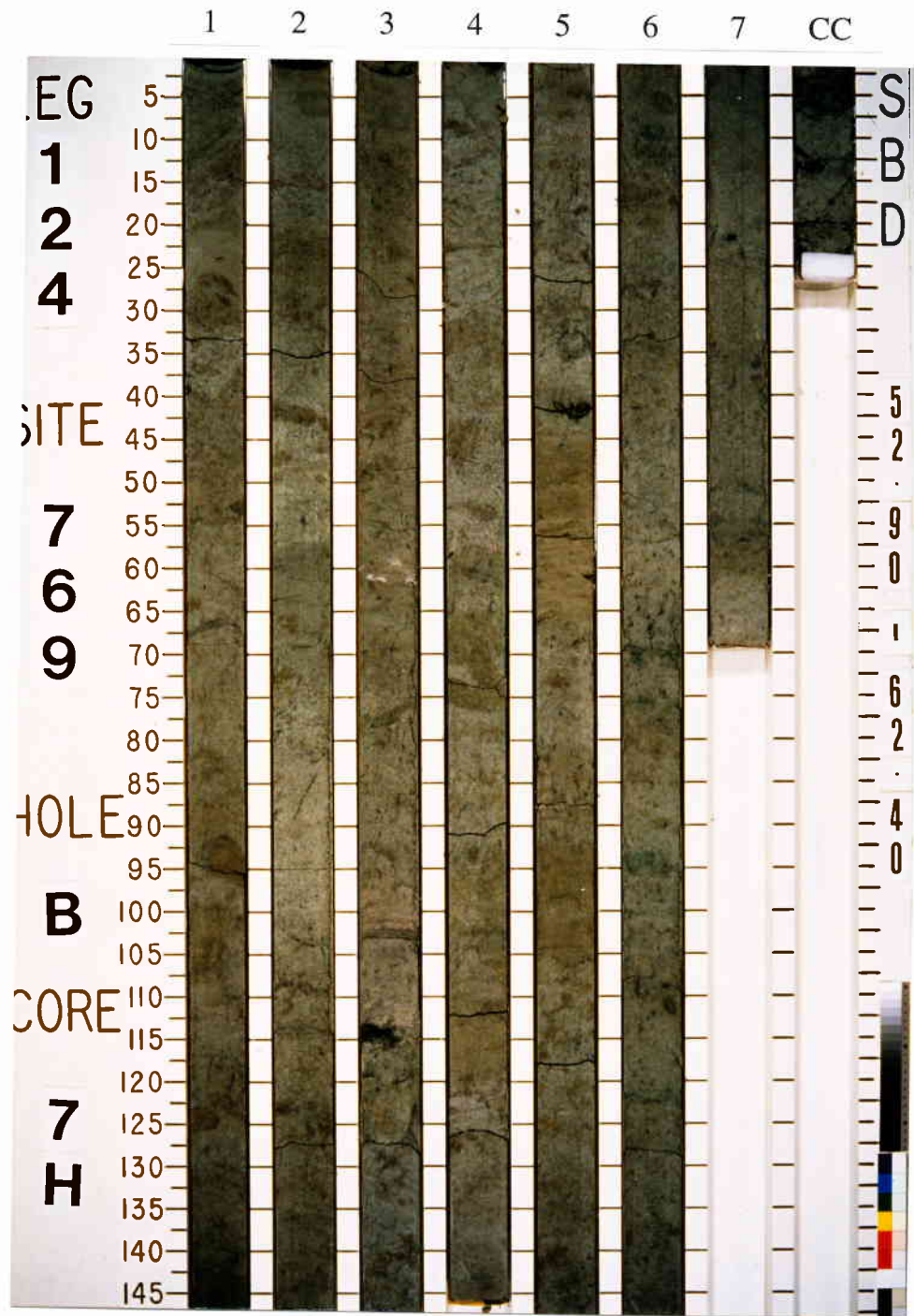


Plate 4. Photograph of Core 124-769B-7H taken on board. Sections are 1-7, and CC (core catcher) from left to right. The boundary of Brunhes/Matuyama polarity transition was recognized at 133 cm of Section 6. Sections 124-769B-7H6 and 124-769B-7H7 are used for the study of Brunhes/Matuyama transition.

comparison. For cores from 767B and core 768B-9H, these two orientations are significantly different, which may be the disturbance of magnetic field produced by the core barrel. Orientations for other cores are in good agreement. To keep consistency, the orientation calculated by averaging non-transitional field are used for the whole cores.

2.4. Sedimentation rates

2.4.1. Revision of Pleistocene geomagnetic polarity timescale

Recent $^{40}\text{Ar}/^{39}\text{Ar}$ dating on volcanic rocks (Spell and McDougall, 1992; Tauxe et al., 1992; Baksi et al., 1992; Izett and Obradovich, 1994; Baksi 1994) indicate that the K-Ar derived ages for geomagnetic field reversals of Pleistocene time (Mankinen and Dalrymple, 1979; Berggren et al., 1985; Harland et al., 1990) are incorrect (Table 2). The newly developed method called 'astronomical calibration' based on adjustment of $\delta^{18}\text{O}$ data (Johnson, 1982; Shackleton et al., 1990; Berger et al., 1994) or sapropel patterns (Hilgen, 1991) to Milankovich cyclicity show consistency with the recent $^{40}\text{Ar}/^{39}\text{Ar}$ dated ages.

Cande and Kent (1992) compiled worldwide magnetic anomaly data and produced new geologic polarity time scale, which is consistent with the results of $^{40}\text{Ar}/^{39}\text{Ar}$ dating and astronomical tuning. The spreading rates for past few million years calculated by the revised geochronological/astronomical ages are in much better accord (<2%) with the rate calculated from space geodetic data (Baksi, 1994; DeMets et al., 1994).

These lines of evidence support that the revised ages for the Pleistocene geomagnetic polarity reversals should be used as a new geomagnetic polarity time scale. In this paper, I will use the ages for the polarity boundary proposed by Baksi (1994). For the age of Cobb Mountain Subchron $^{40}\text{Ar}/^{39}\text{Ar}$ dated age of rhyolite from Cobb Mountain

Table 2. Revisions of geomagnetic polarity timescales (GPTS) for Pleistocene age (ages are in kyr). Recent report of $^{40}\text{Ar}/^{39}\text{Ar}$ dated ages and astronomically calibrated ages are systematically older than the conventional GPTS ages. These are also consistent with the time scale calculated from magnetic anomaly data by Cande and Kent (1992). B/M, uJ, lJ, uO and lO represents Brunhes/Matuyama, upper Jaramillo, lower Jaramillo, upper Olduvai transitions and lower Jaramillo transitions, respectively.

Category	Paper	B/M	uJ	lJ	uO	lO
Conventional GPTS	Mankinen&Dalrymple (1979)	730	900	970	1670	1870
	Berggren et al. (1985)	730	920	980	1660	1880
	Harland et al. (1990)	720	910	970	1650	1880
$^{40}\text{Ar}/^{39}\text{Ar}$ dated	Spell&McDougall (1992)	780±10	915	1010		
	Baksi et al. (1992)	783±11				
	Izett&Obradovich (1994)	770	970	1110		
	Baksi (1994)	780	990	1050	1780	2020
Astronomically calibrated	Shackleton et al. (1990)	780	990	1070	1770	
	Hilgen (1991)				1790	1950
	Berger et al. (1994)	790±5	992±10	1073±10	1783±10	1955±10
Magnetic anomaly	Cande & Kent (1992)	780	984	1049	1757	1983

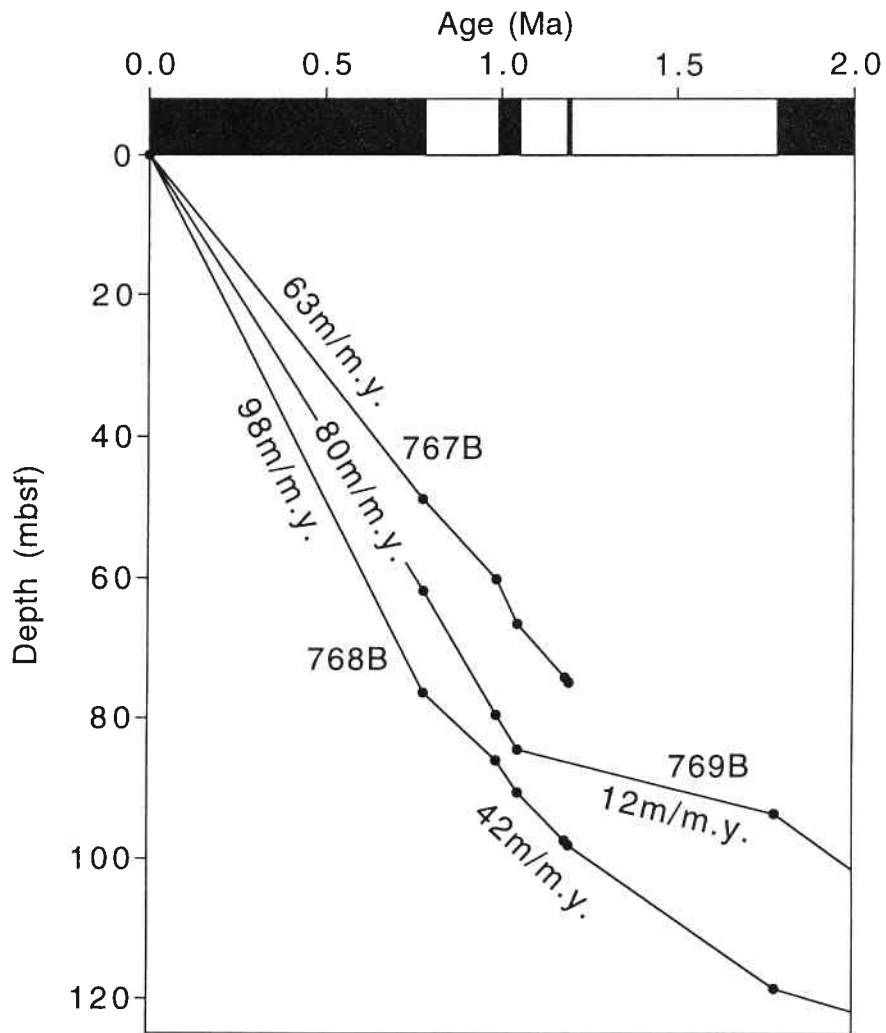


Fig. 3. Polarity transitions plotted versus depth for Holes 767B, 768B and 769B. Sedimentation rates are calculated based on the geomagnetic polarity timescale proposed by Baksi (1994), and the age of the Cobb Mountain Subchron is from Obradovich and Izett (1992).

(1.19 ± 0.01 Ma) was used (Obradovich and Izett, 1992).

2.4.2. Sedimentation rates of Sites 767, 768 and 769

Biostratigraphic and magnetostratigraphic data of ODP Leg 124 are combined by Shyu et al. (1991), however ages of biohorizons interpolated by magnetostratigraphic results are not consistent between sites and only a few of them are in good agreement with the previous calibrations (Berggren et al., 1985). They concluded that the difference may be the results of redeposition by turbidity currents and selective dissolution of key fossils. Thus the most reliable age marker of these sediments are magnetostratigraphy itself.

Magnetic reversal transitions were plotted versus depth for Holes 767B, 768B, and 769B in Fig. 3. For Hole 767B magnetic reversal transitions (Brunhes/Matuyama, upper and lower Jaramillo, and Cobb Mountain Subchron) form almost straight line from the top of the hole yielding sedimentation rate of 63 m/m.y.

Hole 768B gives sedimentation rate of 98 m/m.y. from top of the hole to the Brunhes/Matuyama boundary (76.3 mbsf). A change in sedimentation rates occurs from the Brunhes/Matuyama boundary to the top of the Olduvai Subchron (118.5 mbsf), where sedimentation rates average 42 m/m.y. From top of Olduvai Subchron (118.5 mbsf) to Gilbert/Chron 3An boundary (195.0 mbsf), the depth versus reversal age gives fairly linear correlation with average sedimentation rate of 20 m/m.y.

Hole 769B yields very consistent sedimentation rate (80 m/m.y.) from top of the hole to the base of the Jaramillo Subchron (84.5 mbsf). From the base of the Jaramillo Subchron to the base of the Cochiti Subchron (132.6 mbsf), sedimentation rates decrease dramatically compared with the previous interval, averaging 16 m/m.y. From the base of the Jaramillo Subchron (84.5 mbsf) to the top of the Olduvai

Subchron (93.6 mbsf), sedimentation rates averaged 12 m/m.y, and sedimentation rates increased to 36 m/m.y. throughout the Olduvai Subchron (93.6-102.3 mbsf).

3. Measurements

3.1. Measurements of archive half samples

Just after the recovery of 9.5m-long APC cores, each core was split into 1.5 m-long sections. Initial magnetic susceptibility measurements were made on this whole-core sections with a Bartington Instrument magnetic susceptibility meter (model M.S.1) with a M.S.1/CX 80 mm whole-core sensor loop set at 0.47 kHz in the low-sensitivity mode at intervals of 10 cm. The volume magnetic susceptibility calculated on board in cgs unit was converted to SI unit by multiplying 4π , and was corrected by using the coil-to-inner core liner diameter ratio of 0.825.

After measurements of magnetic susceptibility, whole-core samples were split into working and archive halves (Fig. 4). Archive halves were subjected to pass-through measurements at intervals of 5 mm using a pass-through cryogenic superconducting magnetometer (SRM) of 2G Enterprises (SRM model 760R) on board Joides Resolution (research vessel of ODP). An AF demagnetizer (Model 2G600) capable of AF fields up to 25 mT in three axis was in line with the cryogenic SRM. Long-core samples were demagnetized at a peak AC field of 15 and 20 mT. The results after AF demagnetization at 20 mT were used for the study. A FASTCOM4 multi-serial communication board was installed in the PC-AT compatible computer which controls the SRM, the demagnetizer, and the step motor that transports the core sections. Samples were inserted in the bore hole of the magnetometer by a plastic container connected to a stepping motor by a polyurethane rope. The SQUID electronics of the SRM were operating at the 1X scale and using flux-counting mode. Sensor response curves for archive half core samples were measured with thin half circle standard made of magnetic cassette tape magnetized to three directions.

The pass-through data contains flux jumps, other jumps and spike

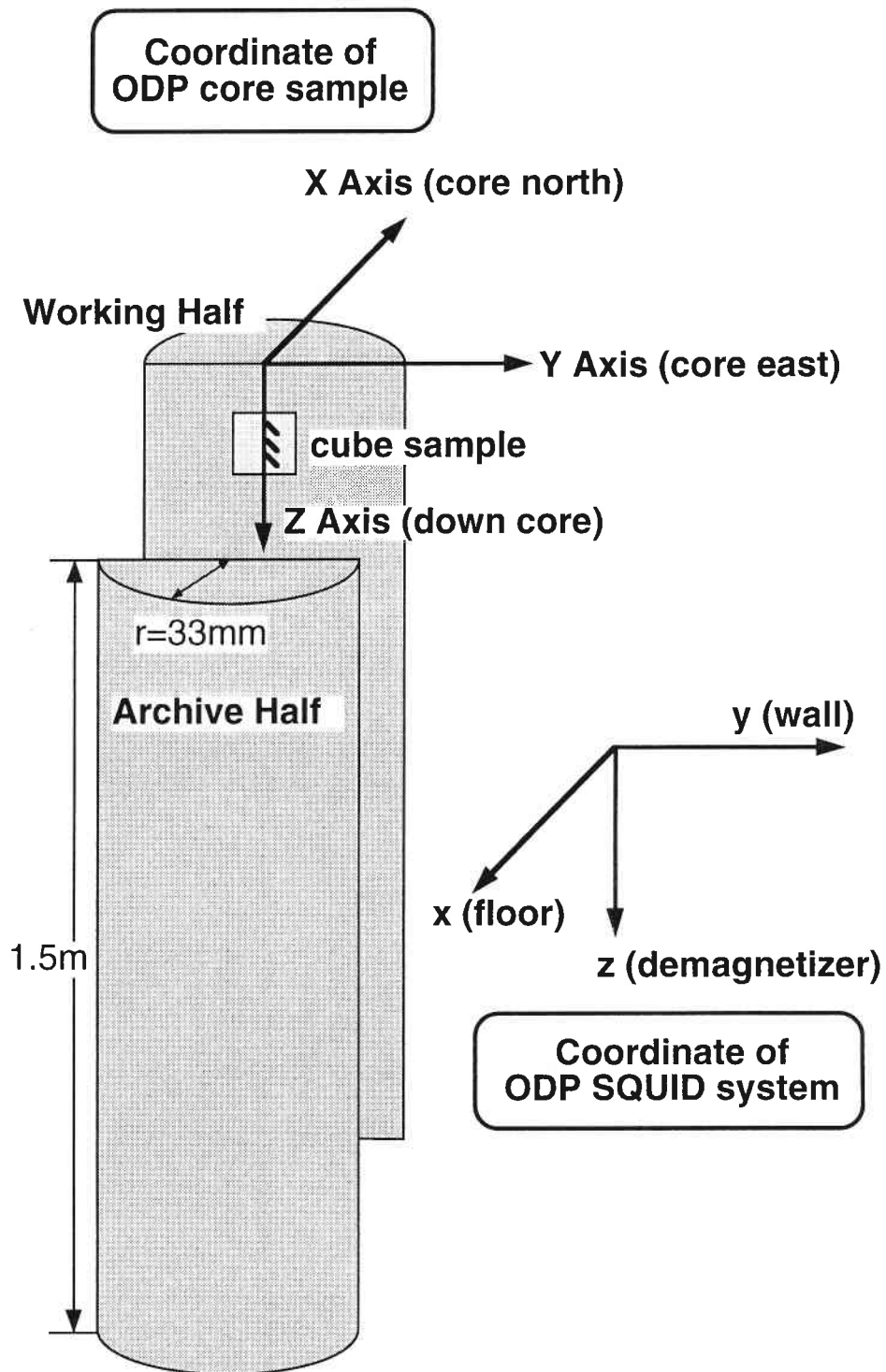


Fig. 4. Coordinates of APC samples and ODP SQUID system are shown. Each Section of 1.5m-long is splitted into working and archive halves. The archive half is subjected to pass-through measurement on board. Oriented paleomagnetic cube samples are taken from the working half.

Table 3. List of corrections made on pass-through measured paleomagnetic data before deconvolution. In each column, left value shows the position of the correction and right value represents the magnetide of correction. Flux jumps are expressed in unit flux quanta and other jumps and spike noises are in emu.

Section	X			Y			Z				
	flux jump	other jumps	spike noise	flux jump	other jumps	spike noise	flux jump	other jumps	spike noise		
767B-6H1	51	-1	253 3.14E-04		263	-3.93E-05	71				
	52	2			328	-3.19E-05					
	57	1									
	62	1									
	68	1									
	74	1									
	99	-1									
	106	-1									
	270	-1									
	339	-1									
767B-6H2	96	-1									
	111	-1									
	196	-1									
	234	1									
	247	1									
767B-7H3	38	-1			139	2.86E-05					
	138	1			208	3.41E-05					
767-8H1	135	-1						181	2.07E-05		
	141	-1									
	148	-1									
	157	-1									
	198	1									
	316	1									
	324	1									
337	1										
768B-9H4			170	4.85E-05				349	1.52E-06	61	-2.03E-05
769A-7H4					73	3.03E-05			102	1.62E-05	
					308	-4.33E-05			237	-1.50E-05	
					332	-3.85E-05					
769A-7H5					224	-3.20E-05					
					333	3.14E-05					
769B-7H6	35	1			296	-3.49E-05			72	1.00E+00	
									229	1.76E-05	
769B-7H7					145	-3.60E-05					
					173	3.33E-05					

noises. These noises were corrected according to the procedure mentioned in Part I of this study. All the noises corrected for the APC samples were listed in Table 3. The flux jumps frequently occur in X axis.

3.2. Measurements of discrete samples

Paleomagnetic cube samples (2.1 cm x 2.1 cm x 1.4 cm = 6.17 cc) were collected at intervals of approximately 5 cm from working halves of the APC samples. Initial magnetic susceptibility was measured on paleomagnetic cube samples by using a Bartington Instruments magnetic susceptibility meter (model M.S.2) at Kyoto University in low frequency modes (0.47 kHz).

Paleomagnetic cube samples were subjected to PAFD (progressive alternating field demagnetization) and PThD (progressive thermal demagnetization) experiments almost alternately. Remanent magnetization was measured by a cryogenic magnetometer (ScT C-112) at Kyoto University. Alternating field demagnetization was conducted using a 2G demagnetizer at 6-13 steps up to 60 mT in maximum. Stepwise thermal demagnetization experiment was conducted in a home-made magnetically shielded furnace up to 610°C at 13-18 steps. The magnetic field intensity remaining in the furnace is less than 10 nT.

Thermomagnetic analysis was performed on three sediment samples with a thermomagnetic balance at Kyoto University in a DC magnetic field of 0.85 T up to 700°C at 8 °C/min in Ar gas. Curie temperature was calculated from heating and cooling curves by fitting quadratic curves on the experimental data lower than the inversion temperature with an accuracy of about 5°C (Moskowitz, 1981).

4. Results

4.1. Results of deconvolution

Remanent magnetizations were obtained continuously at intervals of 5 mm from APC samples after AF demagnetization of 20 mT by a pass-through SQUID magnetometer on board. Pass-through data were analyzed by ABIC-minimizing deconvolution scheme developed in Part I of this study. The magnetization vector components obtained after deconvolution are shown with original magnetic moments and residuals on Fig. 5 (Sections 767B-6H1, 2), Fig. 6 (Section 768B-9H4), Fig. 7 (Sections 769A-7H4, 5) and Fig. 8 (Sections 769B-7H6, 7). Generally quite detailed variations are recovered by deconvolution compared with the variations observable in original magnetic moment before deconvolution.

Table 4 shows several parameters on the results of deconvolution in each case. Natural log of smoothness parameter (lnu) that gives minimum ABIC value ranges from -2.1 to -0.3 and corresponding resolution limit is about 2 cm ranging 1.8-2.3 cm. S/N ratios of magnetizations were also estimated from the power of signal and rms values of residuals. The ratios for Holes 769A and 769B are rather high values of 50 and 42, and that for Hole 767B is low of about 8. If lnu (smoothness) decreases by highly fluctuating feature in some places of the data, the resolution increases, hence S/N ratio decreases with decreasing lnu as a result of trade-off between resolution and S/N ratio. Thus low S/N ratio of Hole 767B may come from strong signal with high frequency, which is clearly seen in magnetization of y-axis after deconvolution at the left end (close to 0 cm; middle bottom of Fig. 5). Section 767B-6H1 may suffer from contamination of rust from the drill string to the sediment at the top of the Core.

768B-9H4: Brunhes/Matuyama (precursor)

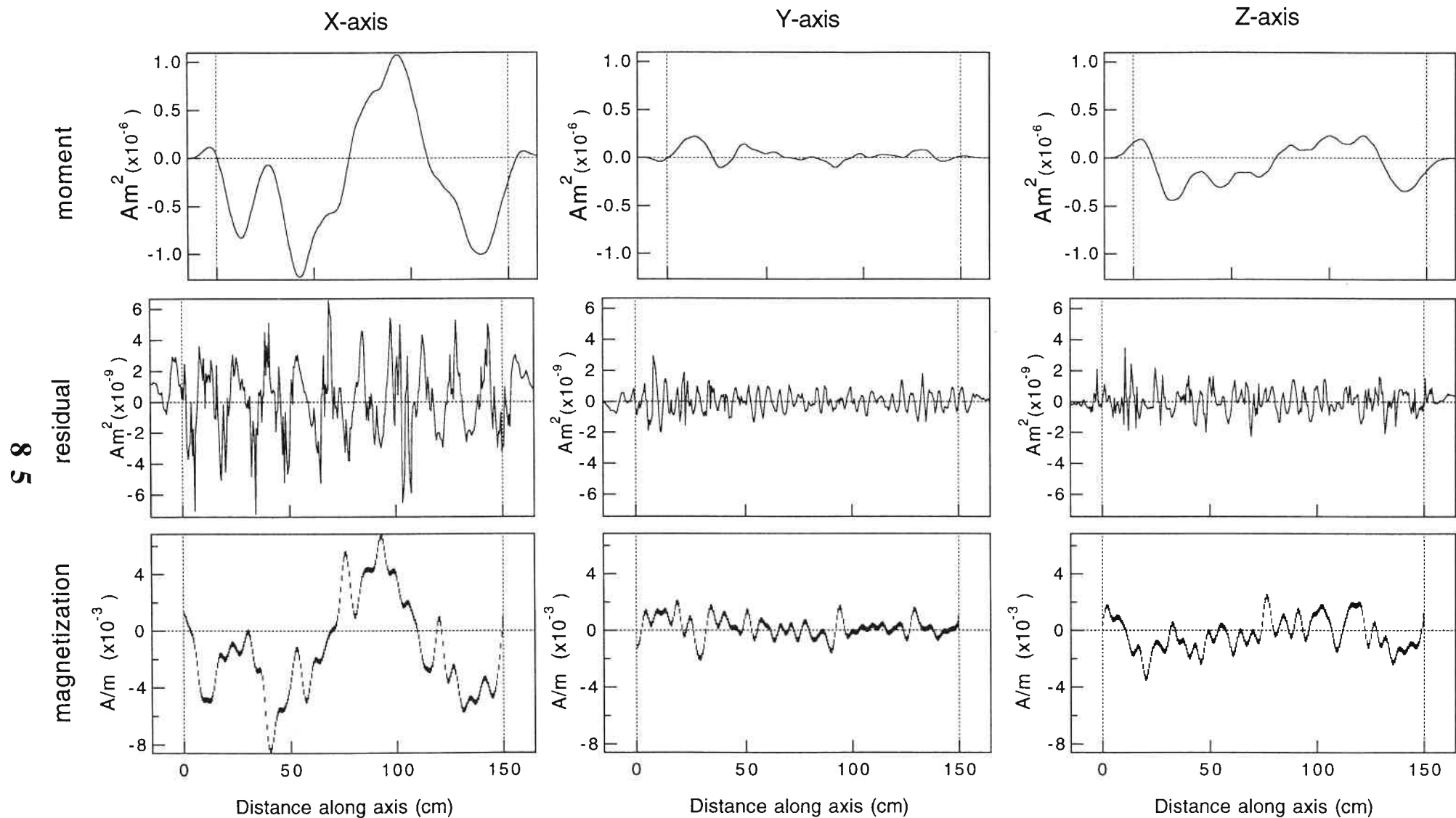


Fig. 6. Same as Fig. 5 for Section 768B-9H4.

769A-7H4, 5: Brunhes/Matuyama

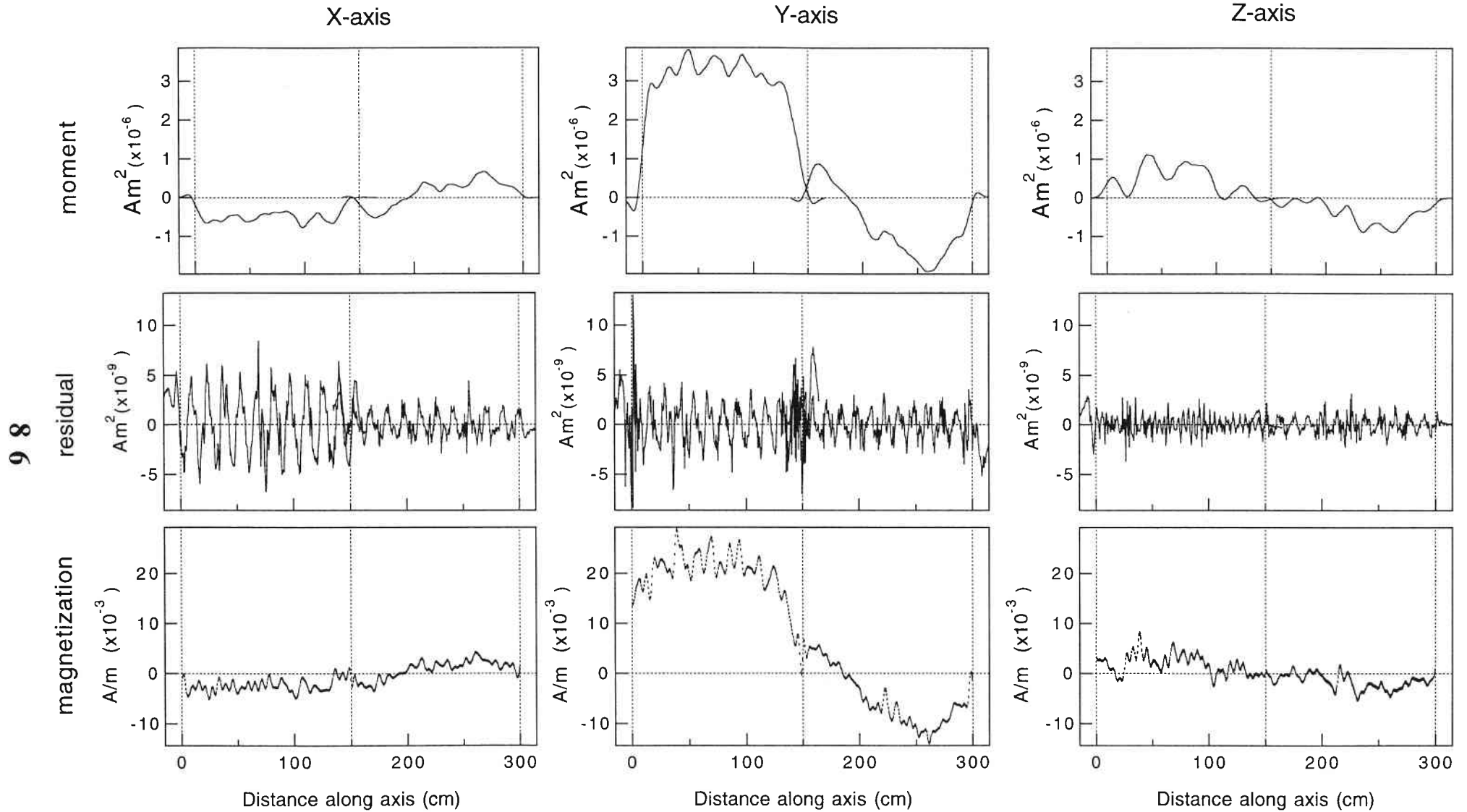


Fig. 7. Same as Fig. 5 for Sections 769A-7H4 and 769A-7H5.

769B-7H6, 7: Brunhes/Matuyama

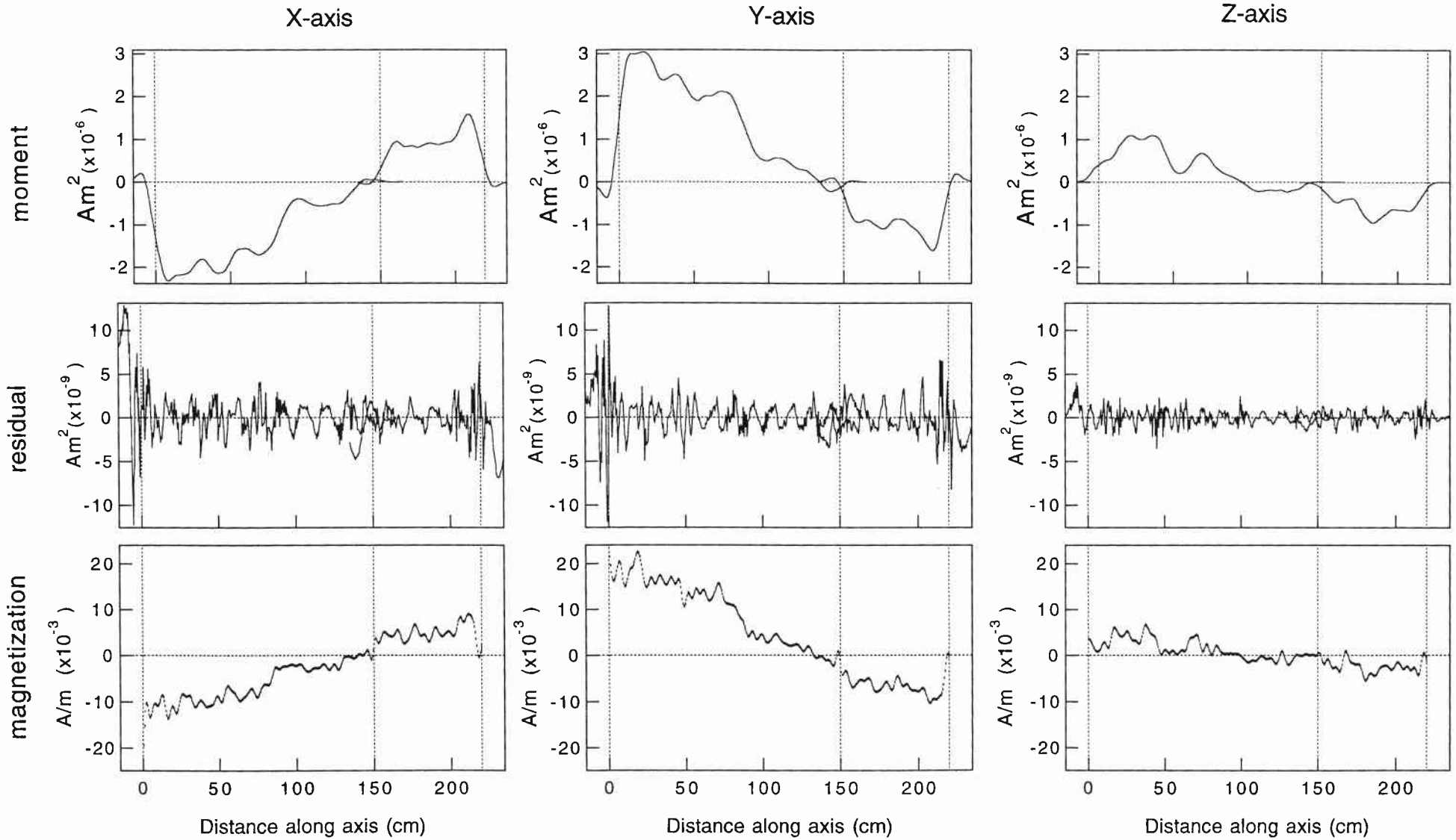


Fig. 8. Same as Fig. 5 for Sections 769B-7H6 and 769B-7H7.

Table 4. Results of deconvolution by ABIC minimization developed in Part I of this study. ABIC come to minimum values at $\ln u$ values listed. S/N ratios for the raw measurements (magnetic moment) estimated as root mean square values of residuals and for magnetization (after deconvolution) estimated from error of magnetizations are also listed. Resolutions are calculated as one-to-one correlation with $\ln u$ (see Part I: Fig. 2).

APC sample (Section)	Number of data	$\ln u$	Minimum ABIC	S/N ratio of moment	Intensity (A/m)	Error (A/m)	S/N ratio of magnetization	Resolution (cm)
767B-6H1,2	720	-1.681	-40094	283	2.80E-02	3.4E-03	8	1.8
768B-9H4	360	-0.312	-24340	263	3.86E-03	2.0E-04	19	2.3
769A-7H4,5	720	-0.496	-47220	646	1.56E-02	3.1E-04	50	2.3
769B-7H6,7	560	-0.402	-36732	529	1.29E-02	3.1E-04	42	2.3

∞
∞

4.2. Magnetic mineral

The magnetization of samples were almost removed by demagnetizing in a peak alternating field of about 45 mT (Fig. 9a). There seems to be no magnetic mineral of higher coercivity. The magnetization of samples were almost completely demagnetized by heating up to 570-600°C during thermal demagnetization experiments (Fig. 9b).

Three bulk samples were subjected to thermomagnetic analysis in Ar atmosphere and the thermomagnetic curves are plotted on Fig. 10. Thermomagnetic curves show Curie temperatures of 490-500°C upon heating (Fig. 10; solid lines) and 520-560°C upon cooling (Fig. 10; dotted lines). The cooling curve exhibit increase in magnetization after heating to 700°C. This can be attributed to the production of magnetite from the matrix of sediment samples. The difference in Curie temperature between heating and cooling may come from lag of rapid temperature change and production of magnetite from the matrix of sediment samples. The true Curie temperature is expected to be around 510°C. From the results of demagnetization character and Curie temperatures, the remanence carrying magnetic mineral is considered to be Fe-rich titanomagnetite. The Curie temperature of 510°C for unoxidized titanomagnetite correspond to composition of about $X=0.3$ (Nishitani and Kono, 1983).

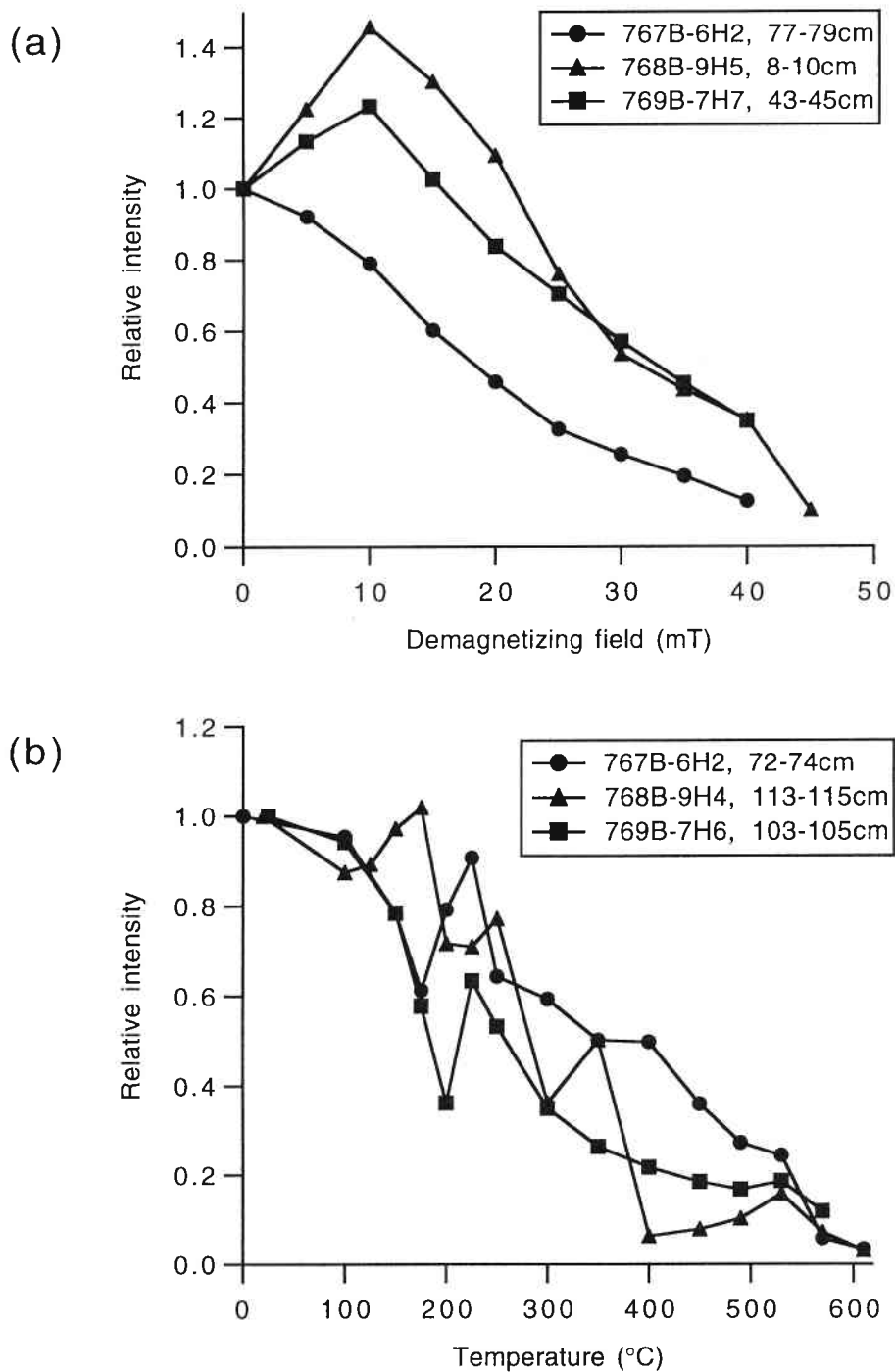


Fig. 9. Decay of remanent magnetization of samples against (a) AF demagnetization and (b) thermal demagnetization are plotted. Solid circles, solid triangles and solid rectangles indicate the samples from Holes 767B, 768B and 769B, respectively. Remanent magnetizations were almost removed at peak alternating field of 45 mT and heating up to 600°C.

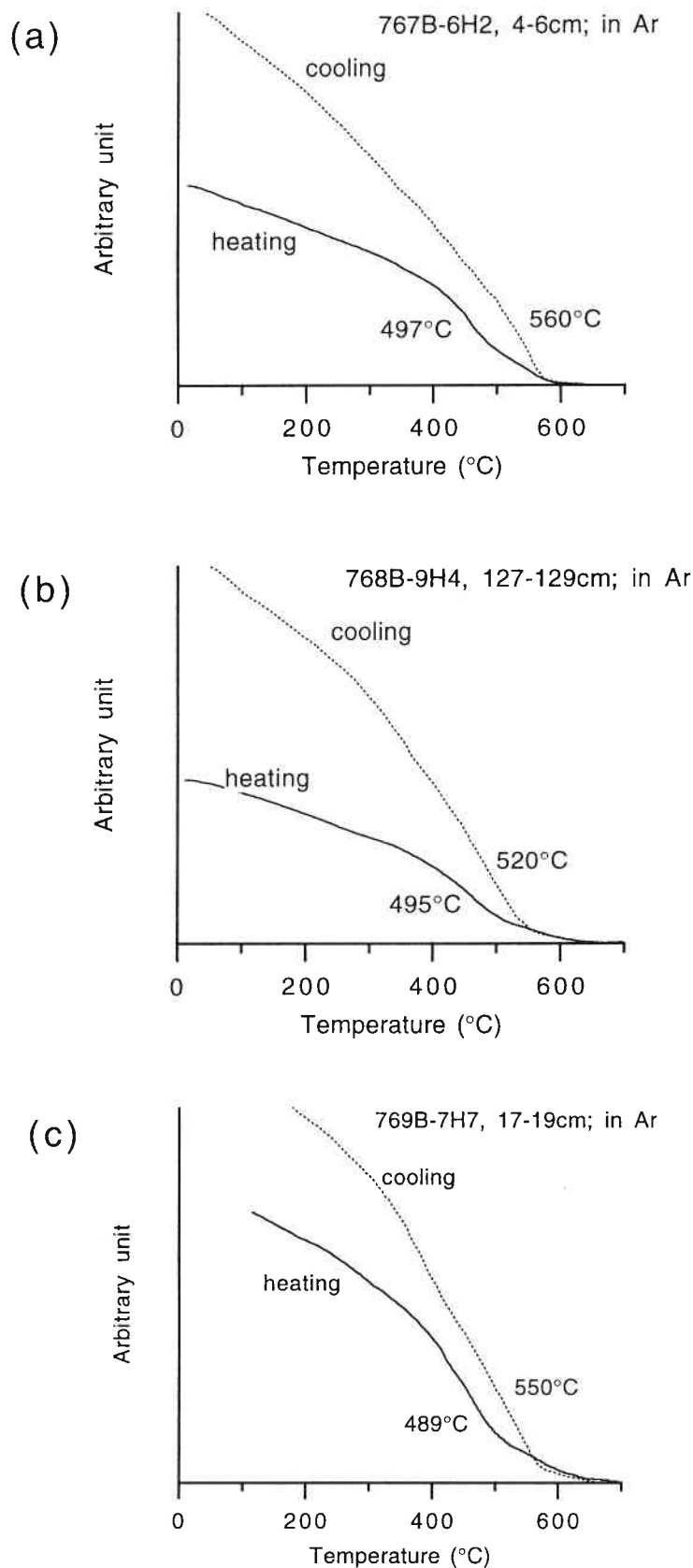


Fig. 10. Results of thermo-magnetic analysis are shown on bulk samples from Holes (a) 767B, (b) 768B and (c) 769B. Samples were heated in a DC magnetic field of 0.85 T up to 700°C at 8 °C/min in Ar atmosphere. Heating and cooling curves are indicated by solid and dotted lines, respectively. Curie temperatures are calculated by fitting quadratic curves to the data points before inversion (Moskowitz, 1981).

4.3. Paleomagnetic results

Stable remanent magnetizations were generally obtained from paleomagnetic cube samples outside of the polarity transition zones. Two paleomagnetic samples from upper and lower ends of the sampled interval were selected from each transition as pilot specimens and PThD experiments were conducted 3-4 months after the cruise. Samples were stable against thermal demagnetization experiments both of reversed polarity (Fig. 11a) and normal polarity (Fig. 11d). Low temperature viscous components were completely demagnetized by heating up to 150°C for most of the samples. High temperature components with unblocking temperature of more than 150°C were demagnetized linearly toward the origin of the diagram until the magnetization almost vanishes up to heating of the 590°C. The intensity of natural remanent magnetization (NRM) is quite strong ranging 10~40 A/m. This can be attributed to high concentration of magnetic mineral supplied as volcanogenic materials which were recognized in the sediments (Rangin and Silver, 1990).

Other samples were measured more than one year after the cruise either by PThD or PAFD experiments. The PThD experiments of samples within 10 cm of the formerly measured samples are compared and many of them show unstable feature of apparent growth or looping of magnetization by heating above 200°C and was subsequently removed around 400-450°C (Fig. 11b, e). This may be interpreted as production and subsequent destruction of magnetic phases of unstable viscous nature by heating. The PAFD experiments of samples outside of transition zones yielded stable linear trend after the demagnetization in a field of 10 mT which is consistent with the directions of thermal demagnetization measured earlier (Fig. 11c, f). Progressive demagnetization results from transition zone generally give less stable results than non-transitional samples. This may be caused by a low

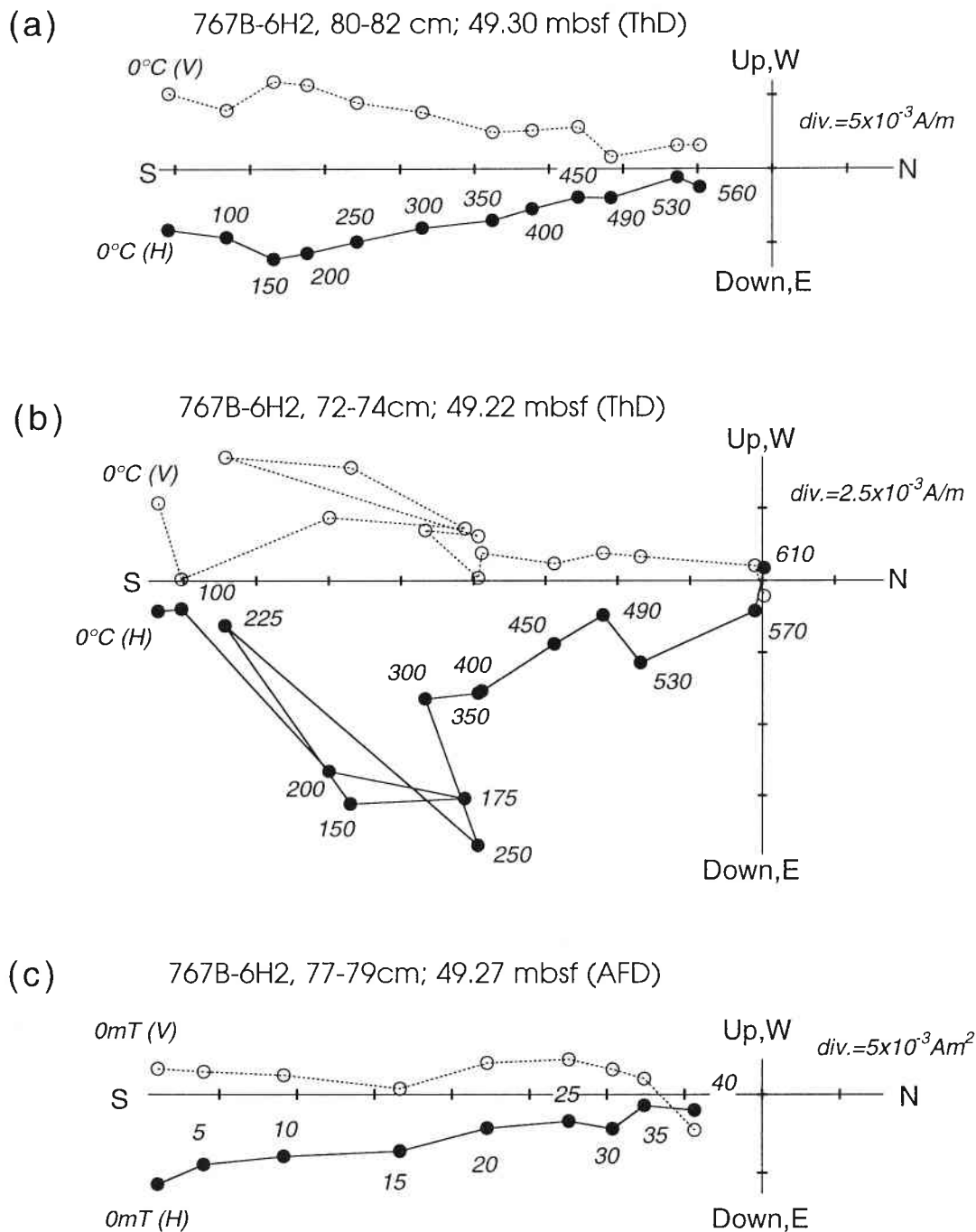


Fig. 11. Vector endpoint diagrams of progressive demagnetization experiments for samples from Hole 767B (a, b, c) and Hole 769B (d, e, f). Solid circles (open circles) represent vector components projected onto horizontal plane (vertical plane). Demagnetization levels are shown by numbers attached in mT (AFD) and °C (ThD). Two samples of each hole from nearly upper and lower end of the sampled intervals were subjected to the progressive thermal demagnetization experiments several months after the cruise (a, d). Other samples were subjected to either PThD or PAFD more than one year after the cruise. PThD (b, e) and PAFD (c, f) results within 10cm of the samples a and d are also shown.

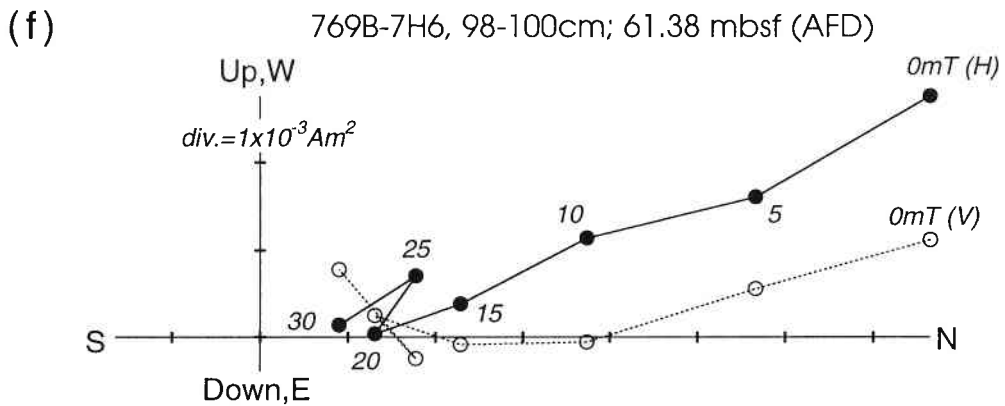
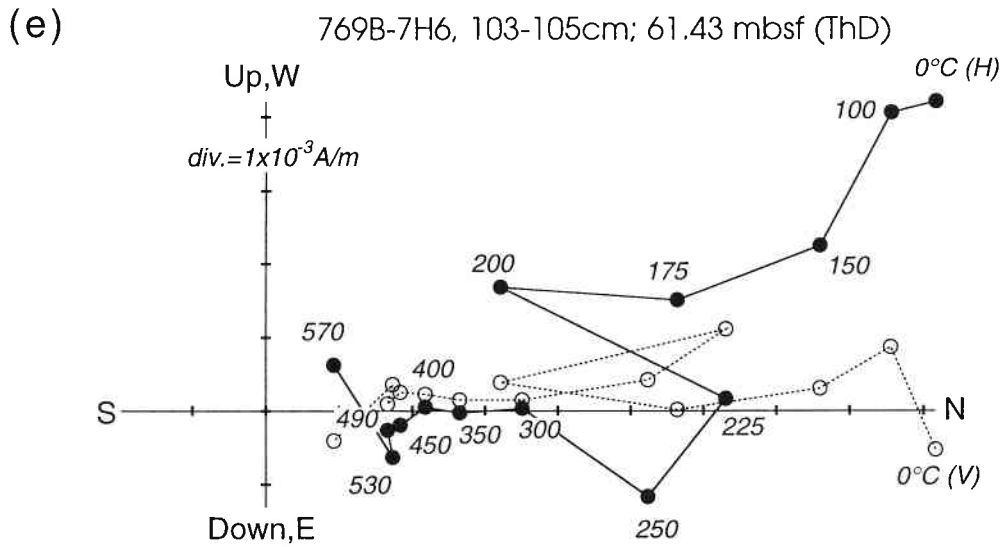
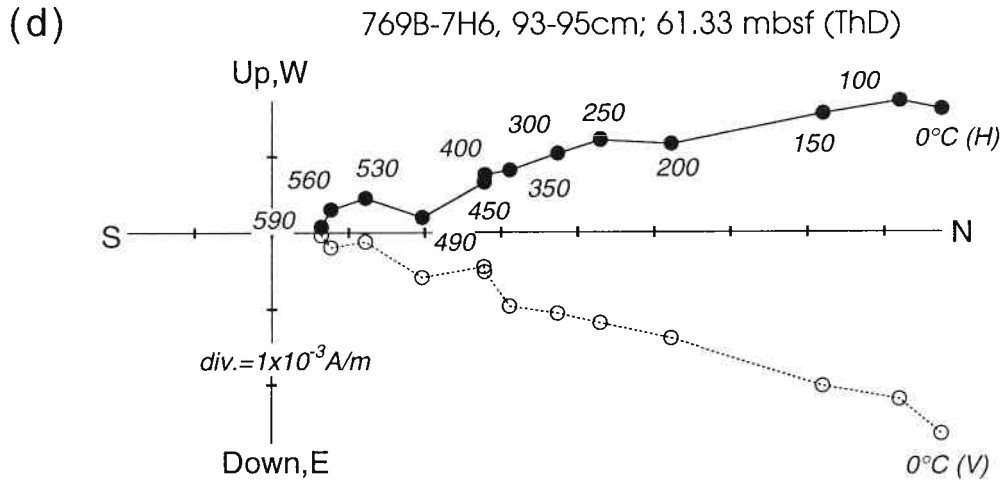


Fig. 11. (continued)

geomagnetic field intensity during polarity reversals.

It seems that the magnetization of samples were affected by drying in the laboratory, however, thermal demagnetization up to 400°C or alternating field demagnetization up to 10 mT is generally enough to get the primary directions. Thus the paleomagnetic directions of discrete samples were determined on the basis of thermal demagnetization at 400°C and alternation field demagnetization at 20 mT. Table 5 shows the paleomagnetic directions, intensities obtained after demagnetization at AF of 20 mT and heating of 400°C. VGP positions were calculated for these paleomagnetic directions and listed in Table 5. Volume magnetic susceptibility before demagnetizations are also listed in Table 5. These results will be used in the next section.

Relative intensity was estimated by normalizing magnetization intensity with the volume magnetic susceptibility both for pass-through measurements and discrete measurements. Paleomagnetic cube samples generally show slight reduction in intensity compared with that of pass-through data after deconvolution. The discrepancy in low-field susceptibility is small compared with the magnetization intensity. This may be the reduction of remanent magnetization by the effect of drying as was pointed out by Otofujii et al. (1982).

Table 5. Results of progressive demagnetization experiments and initial magnetic susceptibilities.

Sample Identification	Depth (mbsf)	Demag. method	Dec (°)	Inc (°)	Intensity (A/m)	VGP		Susceptibility (SI)
						Lat (°N)	Lon(°E)	
124-767B-								
6H1, 134-136cm	48.34	ThD	-33.5	-35.3	1.83E-03	49.1	356.1	
6H1, 139-141cm	48.39	AFD	-22.2	-57.5	6.62E-04	42.4	327.2	1.05E-03
6H1, 144-146cm	48.44	ThD	50.3	-36.9	1.56E-03	34.5	242.6	7.78E-04
6H1, 148-150cm	48.48	ThD	47.4	-40.7	3.13E-03	36.0	246.9	7.13E-04
6H2, 4-6cm	48.54	AFD	35.2	-28.2	1.98E-03	49.9	243.7	9.08E-04
6H2, 9-11cm	48.59	ThD	28.2	-11.3	3.02E-03	60.0	233.6	1.20E-03
6H2, 14-16cm	48.64	AFD	155.6	-31.1	1.97E-03	-63.3	242.0	1.62E-03
6H2, 19-21cm	48.69	ThD	49.5	7.8	3.17E-03	40.6	212.5	1.67E-03
6H2, 24-26cm	48.74	ThD	-3.8	13.7	4.97E-03	85.7	63.6	1.13E-03
6H2, 29-31cm	48.79	AFD	167.7	27.8	5.92E-03	-66.9	155.4	1.73E-03
6H2, 34-36cm	48.84	AFD	176.2	-11.1	6.44E-03	-86.1	225.6	1.38E-03
6H2, 39-41cm	48.89	ThD	171.6	0.2	1.03E-02	-80.3	183.5	2.07E-03
6H2, 45-47cm	48.95	AFD	192.9	-7.3	9.84E-03	-77.1	38.1	1.86E-03
6H2, 49-51cm	48.99	ThD	178.6	-5.6	9.96E-03	-87.5	159.2	1.78E-03
6H2, 54-56cm	49.04	ThD	168.8	-4.2	1.02E-02	-78.5	200.4	1.30E-03
6H2, 60-62cm	49.10	AFD	172.7	-11.8	1.05E-02	-82.7	222.9	1.13E-03
6H2, 65-67cm	49.15	AFD	168.4	-2.3	1.78E-02	-77.9	196.3	1.88E-03
6H2, 72-74cm	49.22	ThD	158.6	-5.2	1.05E-02	-68.5	208.4	1.28E-03
6H2, 77-79cm	49.27	AFD	173.0	-6.5	1.80E-02	-82.9	201.2	1.77E-03
6H2, 80-82cm	49.30	ThD	170.4	-9.0	1.65E-02	-80.4	212.3	1.59E-03
124-768B-								
9H4, 113-115cm	76.13	ThD	-51.1	-45.1	1.12E-03	29.6	354.3	1.47E-03
9H4, 118-120cm	76.18	ThD	148.0	-28.2	4.13E-03	-57.9	226.8	
9H4, 122-124cm	76.22	AFD	182.0	5.6	1.41E-03	-79.0	110.7	1.38E-03
9H4, 127-129cm	76.27	ThD	175.0	-14.5	3.16E-03	-85.0	204.3	8.59E-04
9H4, 131-133cm	76.31	AFD	205.0	-5.9	1.41E-03	-64.6	41.3	9.56E-04
9H4, 135-137cm	76.35	ThD	186.1	-16.8	4.18E-03	-83.9	25.3	6.00E-04
9H4, 139-141cm	76.39	AFD	171.9	-28.9	4.34E-03	-79.1	255.1	
9H4, 143-145cm	76.43	ThD	179.6	-10.7	4.47E-03	-87.4	129.9	6.48E-04
9H4, 147-149cm	76.47	AFD	173.0	-22.1	3.48E-03	-82.3	238.5	7.78E-04
9H5, 4-6cm	76.54	ThD	173.2	-9.8	4.83E-03	-82.6	187.2	7.62E-04

to be continued

Table 5. Results of progressive demagnetization experiments and initial magnetic susceptibilities.

Sample Identification	Depth (mbsf)	Demag. method	Dec (°)	Inc (°)	Intensity (A/m)	VGP		Susceptibility (SI)
						Lat (°N)	Lon(°E)	
9H5, 8-10cm	76.58	AFD	181.0	-5.7	7.07E-03	-84.8	110.2	5.02E-04
9H5, 12-14cm	76.62	ThD	178.2	-8.5	6.69E-03	-85.9	147.0	4.38E-04
9H5, 17-19cm	76.67	AFD	178.0	-22.7	4.00E-03	-85.7	274.1	3.08E-04
9H5, 21-23cm	76.71	ThD	166.2	-18.6	4.23E-03	-76.3	218.7	3.73E-04
9H5, 25-27cm	76.75	ThD	175.0	6.9	3.58E-03	-77.5	144.9	
124-769B-								
7H6, 93-95cm	61.33	ThD	-15.4	10.1	2.93E-03	74.3	18.7	
7H6, 98-100cm	61.38	AFD	-1.7	-11.0	1.33E-03	75.5	308.2	4.05E-04
7H6, 103-105cm	61.43	ThD	-1.2	-5.8	2.19E-03	78.2	307.1	5.35E-04
7H6, 108-110cm	61.48	AFD	5.9	-44.1	3.73E-03	54.9	292.0	6.32E-04
7H6, 113-115cm	61.53	ThD	26.4	-0.8	2.78E-03	62.2	229.2	5.83E-04
7H6, 119-121cm	61.59	AFD	17.5	-4.9	1.44E-03	69.2	243.2	6.97E-04
7H6, 125-127cm	61.65	ThD	36.0	-17.8	2.13E-03	49.9	236.9	5.51E-04
7H6, 129-131cm	61.69	AFD	98.9	-28.0	9.41E-04	-10.8	224.9	5.67E-04
7H6, 135-137cm	61.75	ThD	79.7	-22.5	9.08E-04	8.2	224.6	6.48E-04
7H6, 140-142cm	61.80	AFD	150.1	31.1	9.20E-04	-50.9	170.5	7.46E-04
7H6, 145-147cm	61.85	ThD	150.0	9.7	2.21E-03	-57.1	187.9	6.81E-04
7H7, 2-4cm	61.92	AFD	175.9	8.1	3.29E-03	-76.5	139.0	7.13E-04
7H7, 7-9cm	61.97	ThD	179.0	-7.6	5.26E-03	-84.9	132.8	6.81E-04
7H7, 12-14cm	62.02	AFD	177.9	-9.5	4.78E-03	-85.5	148.3	7.78E-04
7H7, 17-19cm	62.07	ThD	177.0	15.5	3.53E-03	-73.0	131.5	1.20E-03
7H7, 25-27cm	62.15	AFD	191.7	-8.2	4.41E-03	-77.5	52.4	1.17E-03
7H7, 27-29cm	62.17	ThD	178.4	-9.0	6.68E-03	-85.4	141.6	1.04E-03
7H7, 32-34cm	62.22	AFD	168.4	-26.7	7.55E-03	-77.5	237.5	1.09E-03
7H7, 38-40cm	62.28	ThD	170.4	-20.2	5.01E-03	-80.4	221.7	8.59E-04
7H7, 43-45cm	62.33	AFD	187.7	-9.2	6.49E-03	-81.3	59.3	7.94E-04
7H7, 48-50cm	62.38	ThD	166.6	-10.6	5.76E-03	-76.3	197.7	

Paleomagnetic results were obtained for the measurement after demagnetization at 20 mT (AFD) and 400°C (ThD). Orientations were corrected according to the average declination of non-transitional field directions.

4.3.1. Hole 767B

The paleomagnetic results of Brunhes/Matuyama transition from Hole 767B are shown on Fig. 12. The transition zone is characterized by a low intensity of magnetization at 48.25-48.75 mbsf following swing in declination at 48.71 mbsf (Fig. 12). The low intensity of magnetization increased the error of declination and inclination after deconvolution (Fig. 12). Susceptibility is rather consistent for this interval resulting in a decrease of relative intensity. Relative intensity have two highs at around 47.5 mbsf and 49.5 mbsf. The relative intensity is reduced to less than 1/25 of peak value at the boundary and about 1/5 for the intensity low between 48.25 and 48.75 mbsf. The susceptibility increases to about two times higher value at 47.2 mbsf.

Declination shows sharp change of polarity at 48.7 mbsf followed by an intermediate direction at 48.5-48.7 mbsf about 30° east of north and finally settle to the non-transitional directions (north directing dipole). Inclination gradually decreases from about zero just after the reversal to -45° at 48.45 mbsf and come back to the negative low and gradually to positive value at 48 mbsf. The VGP paths for the transitional directions are calculated and plotted on Fig. 13. The error angle of VGP is not indicated on Fig. 13, which is quite large of about 30°. The VGPs show quick swing to Africa, cross the equator to Alaska staying for a long period (about 3000 yr assuming constant sedimentation rate), change suddenly to northeast Canada, and shift gradually to the stable north dipole position with fluctuations. This correspond to the nearly stepwise change in declination at 48.5 mbsf. Sparse data points between $\pm 30^\circ$ latitude may indicate the rapid change of field directions during the polarity reversal.

Remanent magnetizations of discrete samples generally show quite consistent directions with those of pass-through data after deconvolution (Fig. 12) . The VGPs of discrete samples corresponding to

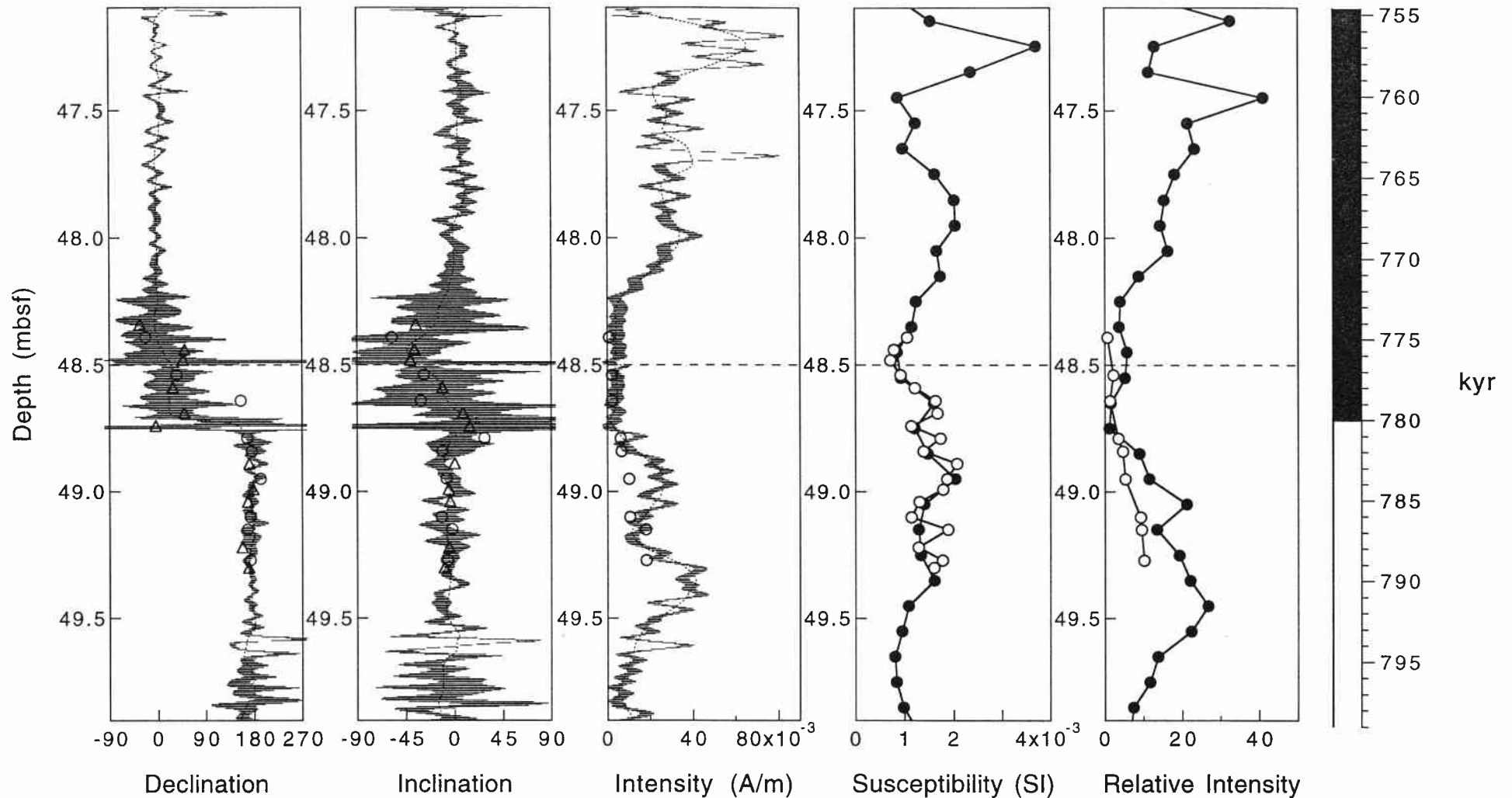


Fig. 12. Paleomagnetic results of Brunhes/Matuyama boundary for Hole 767B (767B-6H1 and 767B-6H2) are shown. Declination, inclination, intensity, susceptibility and relative intensity are plotted versus depth with a time scale estimated by assuming constant sedimentation rate of 6.3 cm/kyr. Horizontal broken lines represent the boundary of sections. Results (declination, inclination and intensity) of pass-through measurement before deconvolution are shown by dotted lines and results after deconvolution are shown by horizontal bars of which length indicate 95% confidence limits. Open circles and open triangles represent paleomagnetic results of cube samples after AF demagnetization of 20 mT and thermal demagnetization of 400°C, respectively. Volume magnetic susceptibility and relative intensity normalized by susceptibility are plotted by solid circles for pass-through data and open circles for cube samples.

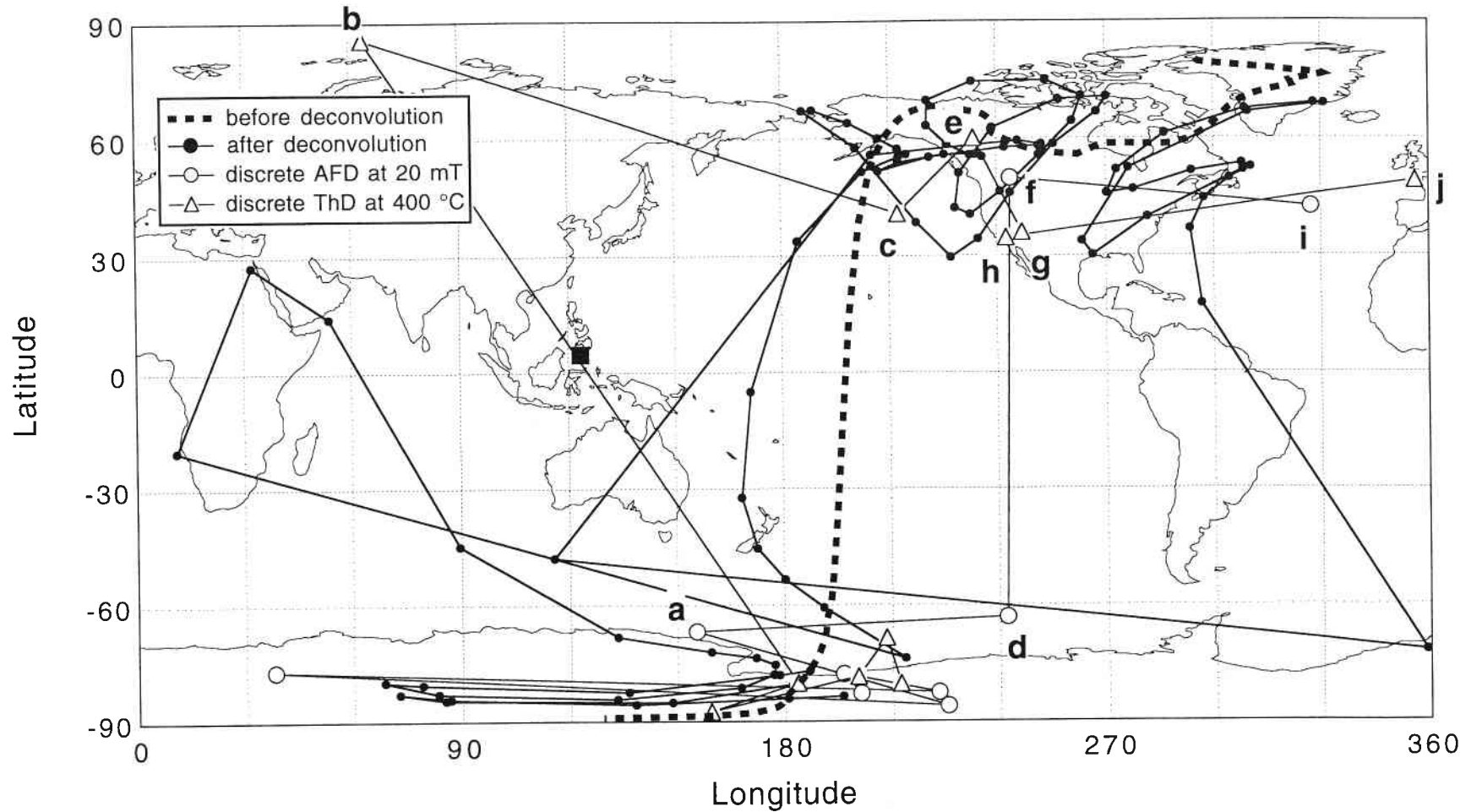
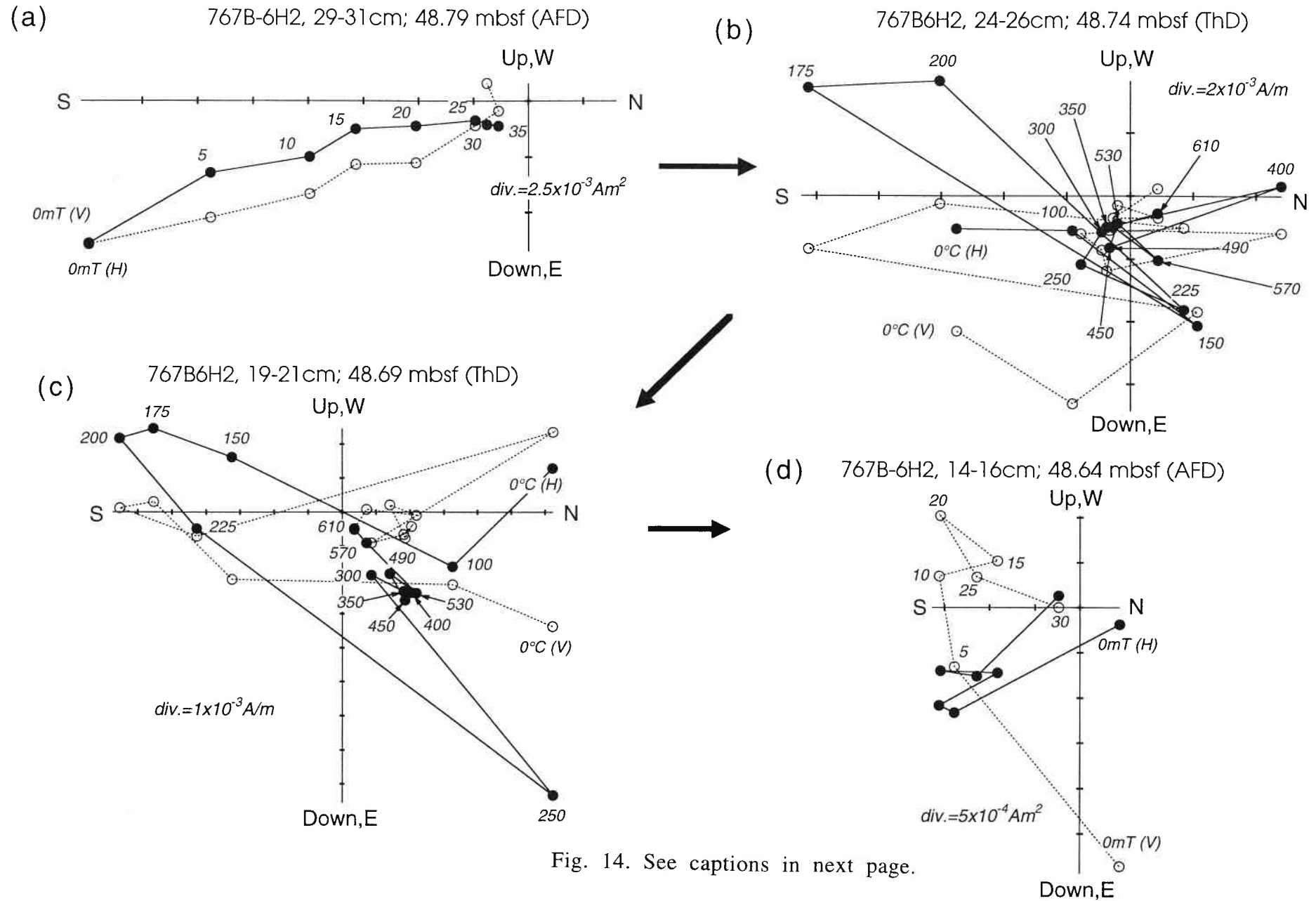


Fig. 13. VGP paths of Brunhes/Matuyama polarity transition for Hole 767B are plotted. Location of the site is indicated by a solid rectangle. Thick broken line show the VGP path for the pass-through data before deconvolution. Solid lines with small solid circles represent the VGP path for pass-through data after deconvolution. Open circles and open triangles represent VGPs of cube samples after 20 mT AF demagnetization and thermal demagnetization of 400°C. Bold alphabets from **a** to **j** represent cube samples showing transitional directions.

the transitional directions are denoted by "a" to "i" (polarity reversal proceeds in alphabetical order). The results of demagnetization on discrete samples are shown on Fig. 14. The remanent magnetization below (before) the low intensity zone show stable directions (Fig. 14a). Discrete samples from intensity low at 48.25-48.75 mbsf is unstable against demagnetization (Fig. 14b~j). Sample 767B-6H2, 24-26 cm (Fig. 14b) seems most unstable, which corresponds to the swing of VGP recognized in the deconvolution results of pass-through data. Although unstable compared with the results outside the transition zone, samples "c", "e", "f", "g" and "h" seems to give directions toward the origin of the diagram with large amplitude of noise (Fig. 14c, e, f, g, h). Samples "i" and "j" show VGPs close to the second cluster over northeast Canada. Fig. 14i show unstable character, however, Fig. 14j seems to give reliable directions of negative inclination and westerly declination above 250°C.



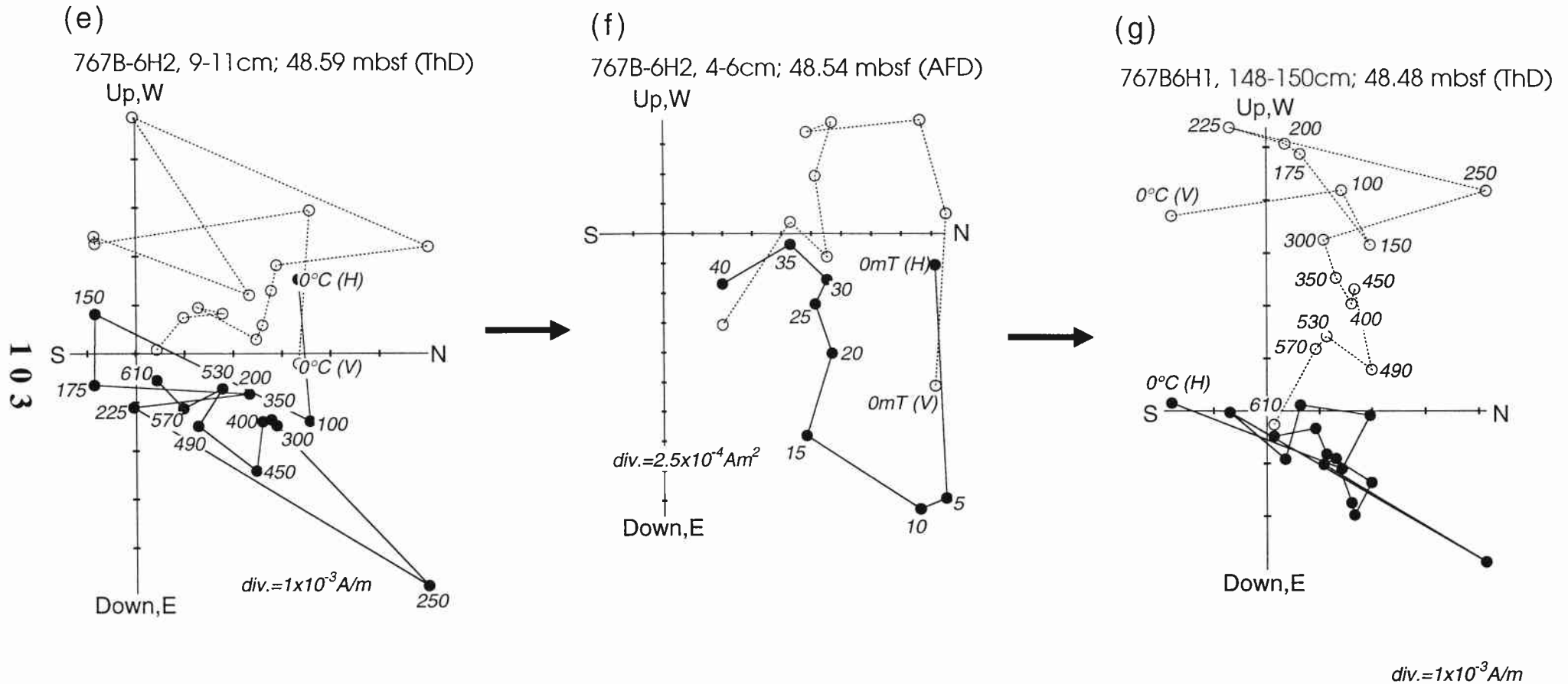
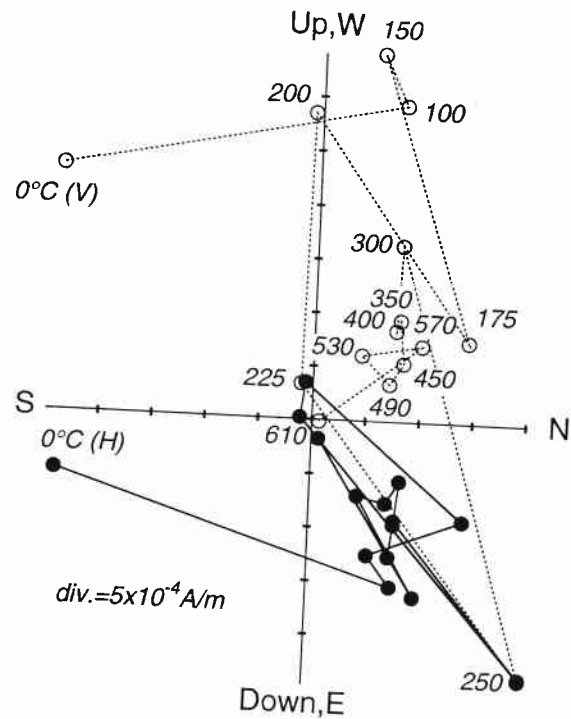
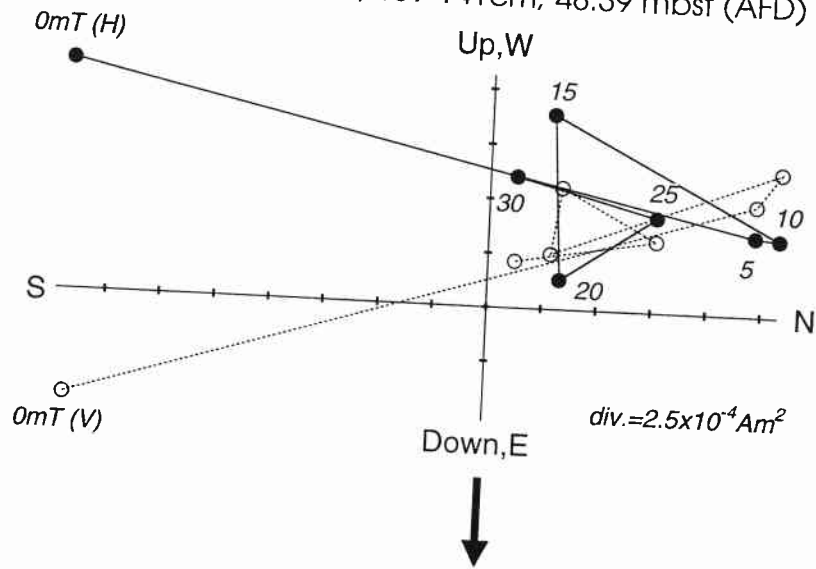


Fig. 14. Vector endpoint diagrams of progressive demagnetization experiments for cube samples of polarity transition zone from Hole 767B. Alphabets a~j on Fig. 17 correspond to (a)~(j). The depth (age) of the sample decreases (becomes younger) in alphabetical order. Solid circles (open circles) represent vector components projected onto horizontal plane (vertical plane). Demagnetization levels are shown by numbers attached in mT (AFD) and °C (ThD). Samples a, d, f and i were AF demagnetized and samples b, c, e, g, h and j were subjected to thermal demagnetization experiments.

(h) 767B6H1, 144-146cm; 48.44 mbsf (ThD)



(i) 767B-6H1, 139-141cm; 48.39 mbsf (AFD)



(j) 767B6H1, 134-136cm; 48.34 mbsf (ThD)

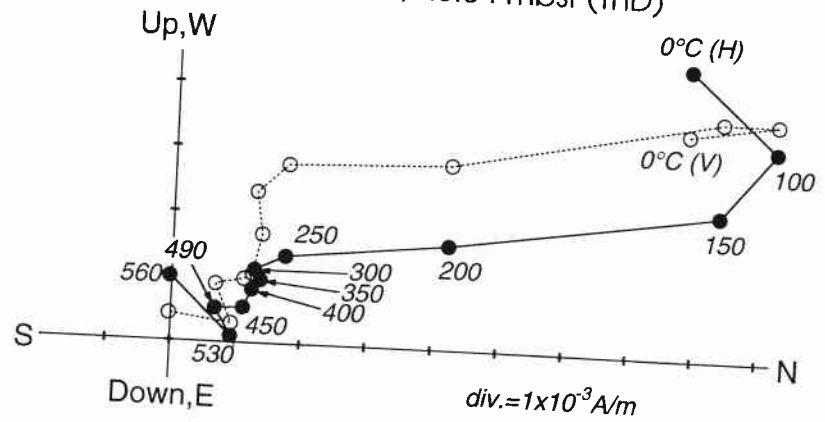


Fig. 14. (continued)

4.3.2. Holes 769A and 769B

Paleomagnetic results from Holes 769A and 769B show quite consistent record with each other (Figs. 15 and 16). Declinations of Holes 769A and 769B show sharp swing at 62.3 and 61.75 mbsf, respectively. Both show subsequent intermediate direction of slightly east of north. Inclination show steep negative value at the reversal boundary, swing again to positive value and settle to the low value.

VGP paths calculated for these directions were plotted on Figs. 17 and 18. Although these two VGP paths show slight difference, their pattern agree with each other indicating three segments of cusps or small loops below New Zealand (segment 1), and central to south Pacific (segment 2), followed by a large loop over Atlantic touching Green Land and to Alaska (segment 3). The VGPs stay for about 2000-2500 yr (16-20 cm) around the northern part of Canada (cluster) and change to the position closer to the axial dipole field. It should be noted that the large loop (segment 3) is significantly larger than 95% confidence ovals both for 769A and 769B.

Volume magnetic susceptibility is almost constant with average value of 8.0×10^{-4} (SI) and show two peak values slightly higher than 1.0×10^{-3} (SI) in both records. One is at 62.8 mbsf of Hole 769A and at 63.3 mbsf of 769B, and another is at 61.6 mbsf of Hole 769A and at 61.2 mbsf of Hole 769B. Relative intensity calculated for both Holes show gradual decrease from around 790 ka (63.1 mbsf for Hole 769A; 62.5 mbsf for Hole 769B) to the minima at the polarity transition and gradually increase to peak value at around 765 ka (60.9 mbsf for Hole 769A; 60.5 mbsf for Hole 769B). The relative intensity record of Hole 769A continues upward and slightly decrease from about 60.9 mbsf to top of the Section 769A-7H4. The minimum of relative intensity is about 1/25 of peak value at around 765 kyr. Oxygen isotope record reported by Linsley and von Breyman (1991) for Hole 769A are plotted

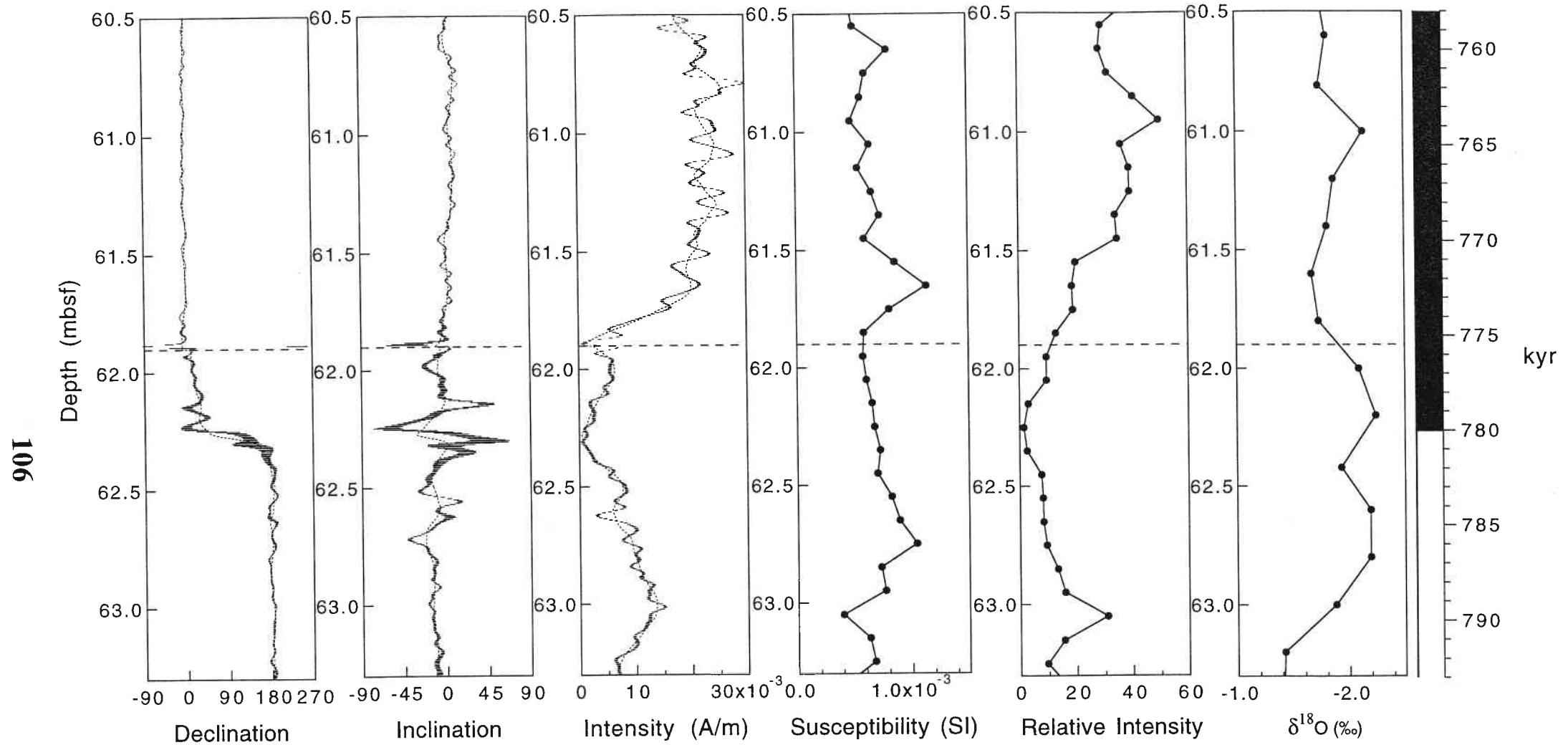


Fig. 15. Paleomagnetic results of Brunhes/Matuyama polarity transition for Hole 769A (769A-7H4 and 769A-7H5) are shown. Declination, inclination, intensity, susceptibility and relative intensity are plotted versus depth with a time scale estimated by assuming constant sedimentation rate of 8.0 cm/kyr. Horizontal broken lines represent the boundary of the sections. Results (declination, inclination and intensity) of pass-through measurement before deconvolution are shown by dotted lines and results after deconvolution are shown by horizontal bars of which length indicate 95% confidence limits. Volume magnetic susceptibility and relative intensity normalized by susceptibility are also plotted. Oxygen isotope data obtained from planktonic foraminifer by Linsley and von Breyman (1991) are also shown.

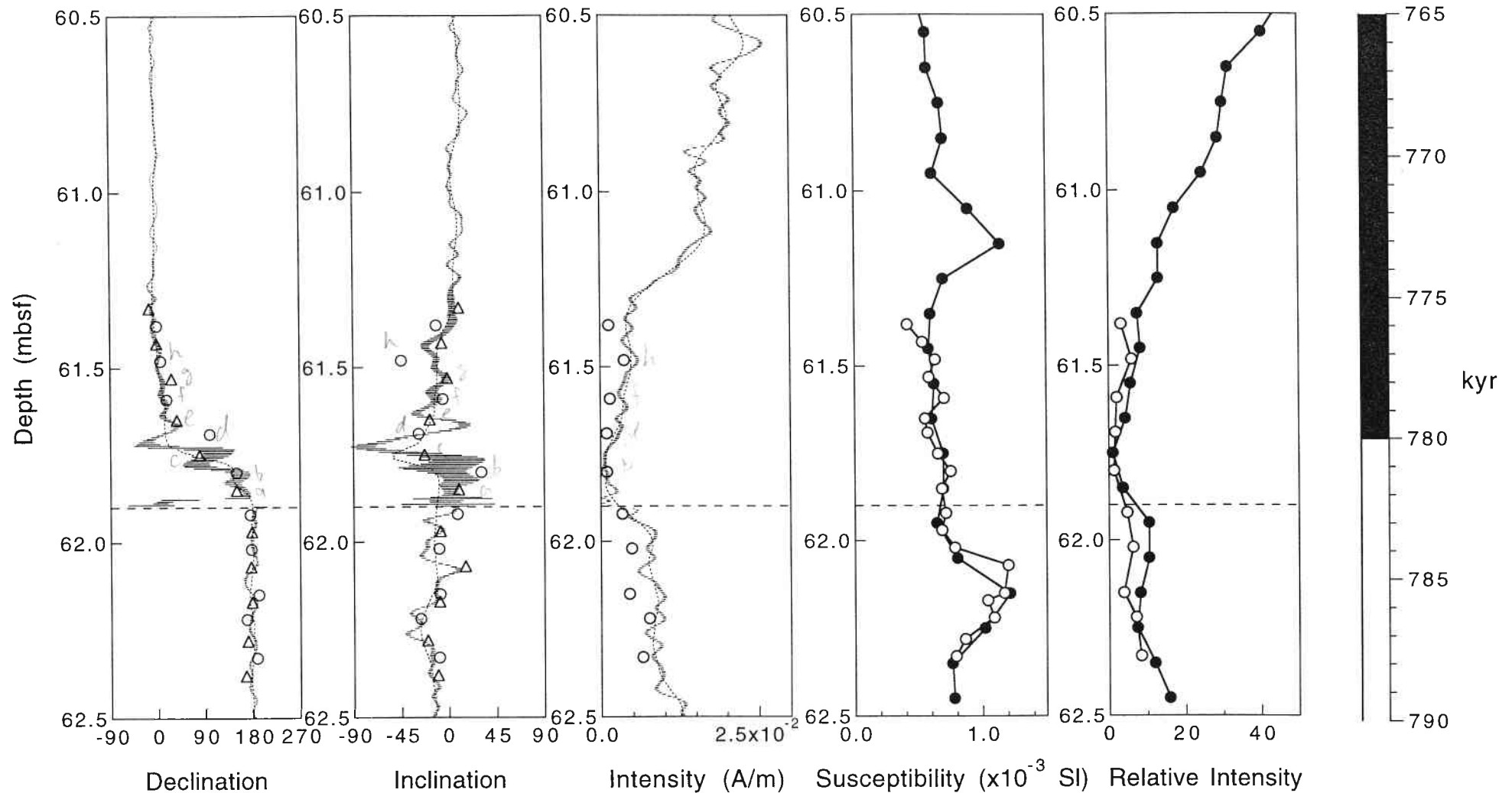


Fig. 16. Paleomagnetic results of Brunhes/Matuyama polarity transition for Hole 769B (769B-7H6 and 769B-7H7) are shown. Declination, inclination, intensity, susceptibility and relative intensity are plotted versus depth with a time scale estimated by assuming constant sedimentation rate of 8.0 cm/kyr. Horizontal broken lines represent the boundary of sections. Results (declination, inclination and intensity) of pass-through measurement before deconvolution are shown by dotted lines and results after deconvolution are shown by horizontal bars of which length indicate 95% confidence limits. Open circles and open triangles represent paleomagnetic results of cube samples after AF demagnetization of 20 mT and thermal demagnetization of 400°C, respectively. Volume magnetic susceptibility and relative intensity normalized by susceptibility are plotted by solid circles for pass-through data and open circles for cube samples.

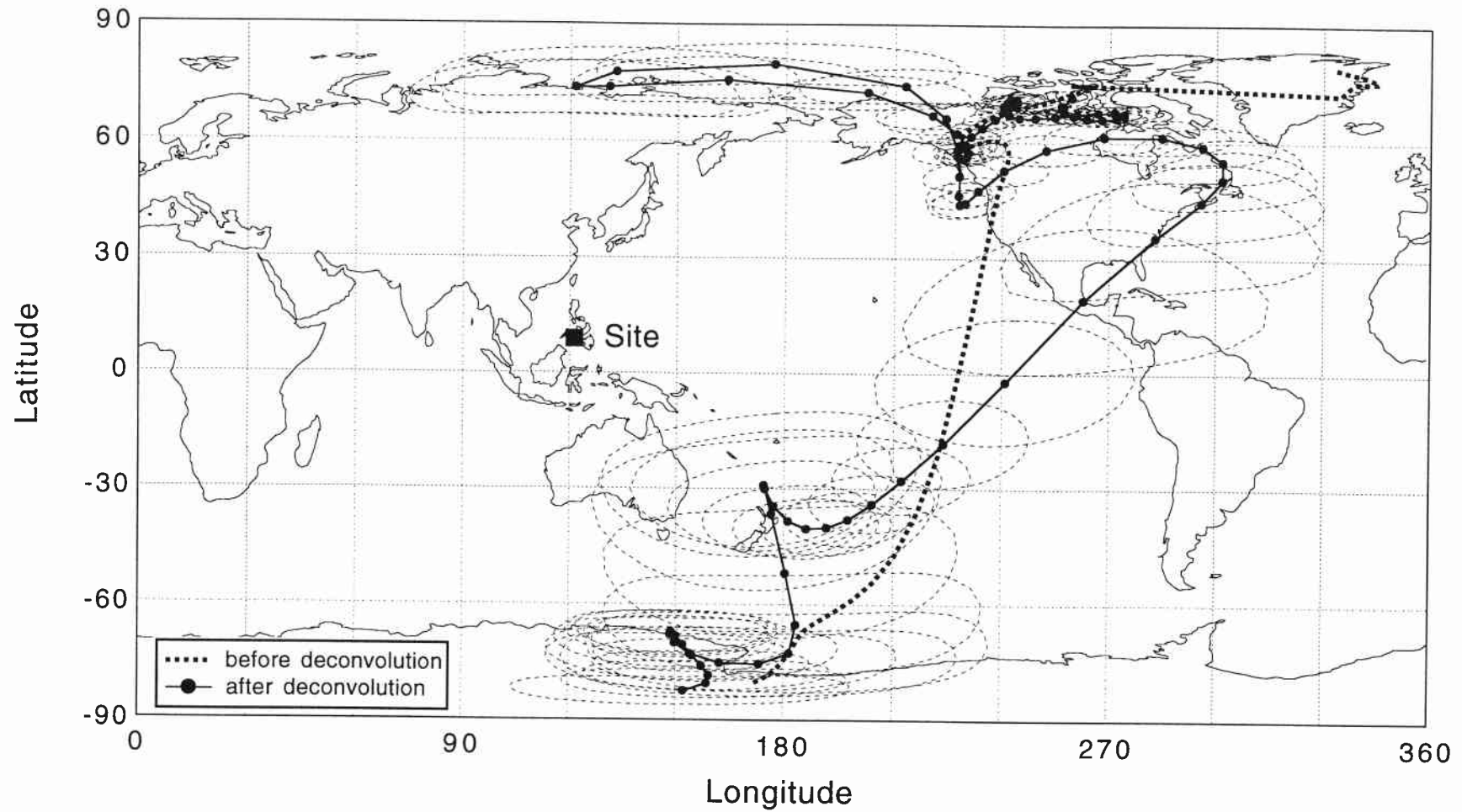


Fig. 17. VGP paths of Brunhes/Matuyama polarity transition for Hole 769A are plotted. Location of the site is indicated by a solid rectangle. Thick broken line show the VGP path for the pass-through data before deconvolution. Solid lines with small solid circles represent the VGP path for pass-through data after deconvolution.

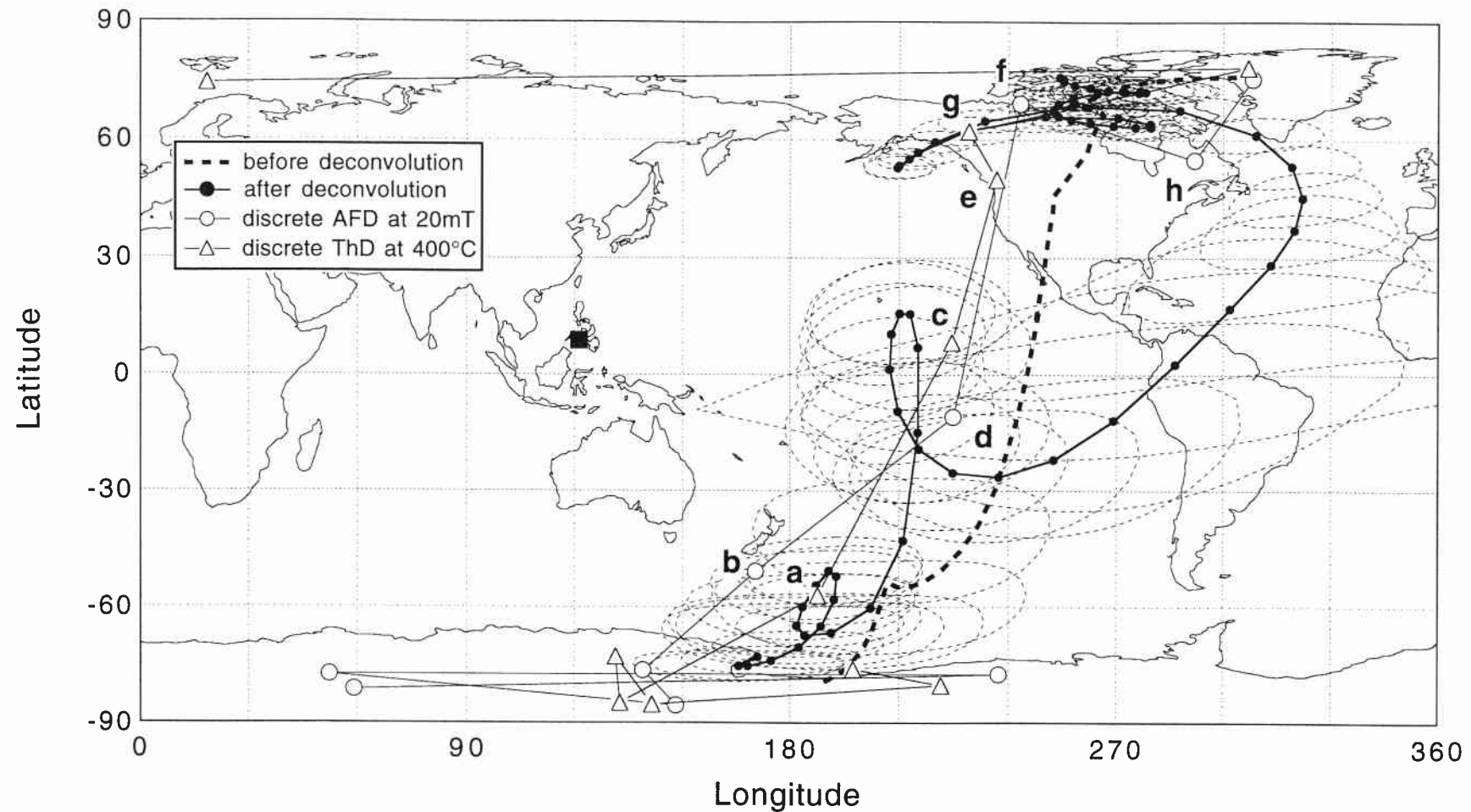


Fig. 18. VGP paths of Brunhes/Matuyama polarity transition for Hole 769B are plotted. Location of the site is indicated by a solid rectangle. Thick broken line show the VGP path for the pass-through data before deconvolution. Solid lines with small solid circles represent the VGP path for pass-through data after deconvolution. Open circles and open triangles represent VGPs of cube samples after 20 mT AF demagnetization and thermal demagnetization of 400°C. Bold alphabets from **a** to **j** represent cube samples showing transitional directions.

with the paleomagnetic results. The polarity transition is about 40 cm above the oxygen isotopic Stage 19.1. This is consistent with the relationships between Brunhes/Matuyama transition and Stage 19.1 obtained from the deep-sea sediments of comparatively high sedimentation rates (deMenocal et al., 1990) .

Figs. 19 show PThD and PAFD results for the samples from transition zone. The results of PThD (Fig. 19a, c, e, g) show relatively stable features trending toward the origin. The results of PAFD (Fig. 19b, d, f, h) is less stable, however, all the results, pass-through data after deconvolution, PAFD and PThD results, are quite consistent on VGP paths (Fig. 18). Higher latitude loop of the first segment correspond to the depth range of 61.80-61.85 mbsf (~ 600 yr) and samples "a" and "b" is quite consistently lie within the 95% confidence limit ovals for the VGPs of this segment.

The second segment correspond to the depth interval of 61.75 to 61.79 mbsf (~ 500 yr), however, the demagnetization character is unstable (Fig. 19c, d). Samples "e" and "g" are thermally demagnetized and exhibit complicated pattern with multiple component during stepwise heating. The viscous component was removed by heating up to 200°C. Between 200°C and 250°C magnetization increased and was subsequently removed above 300°C. This can be interpreted either by the unstable character associated with the drying effect or real geomagnetic feature during the transition. Above 300°C the magnetization vector seems to give primary directions. Although sample "g" seems to have two components, the magnetization at the 400°C heating is adopted. These directions give (Fig. 19e, g) VGP positions around Alaska, which is also seen for VGPs of magnetization after deconvolution.

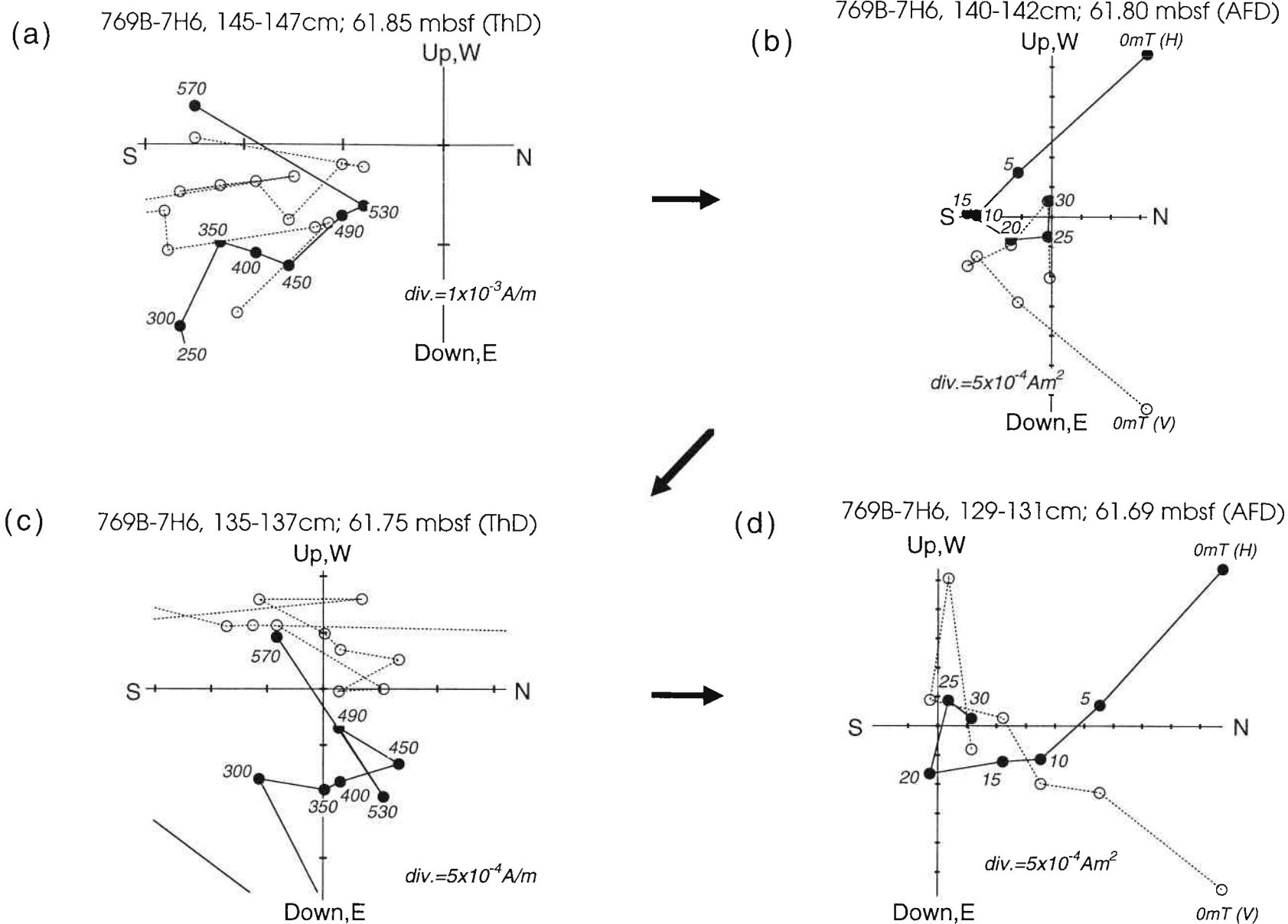


Fig. 19. Vector endpoint diagrams of progressive demagnetization experiments for cube samples of polarity transition zone from Hole 769B. Alphabets **a**~**h** on Fig. 22 correspond to (a)~(h). Samples **b**, **d**, **f** and **h** were AF demagnetized and samples **a**, **c**, **e** and **g** were subjected to thermal demagnetization experiments.

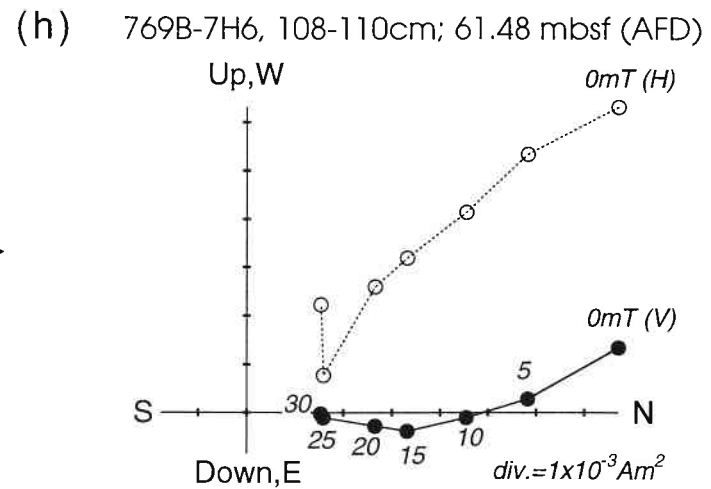
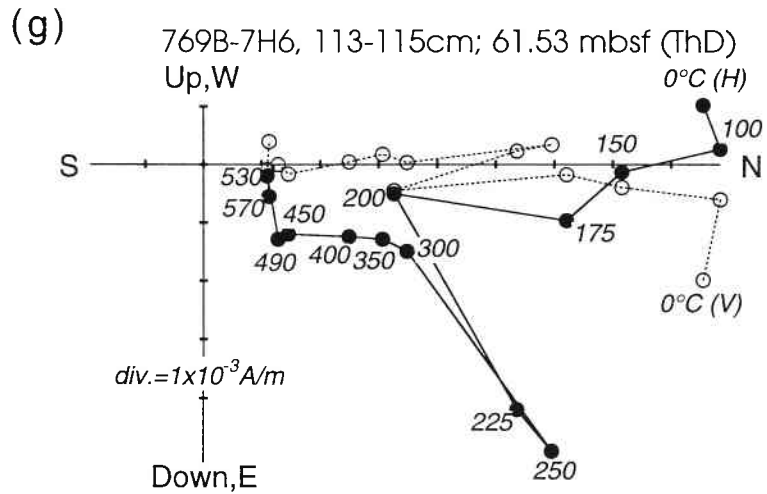
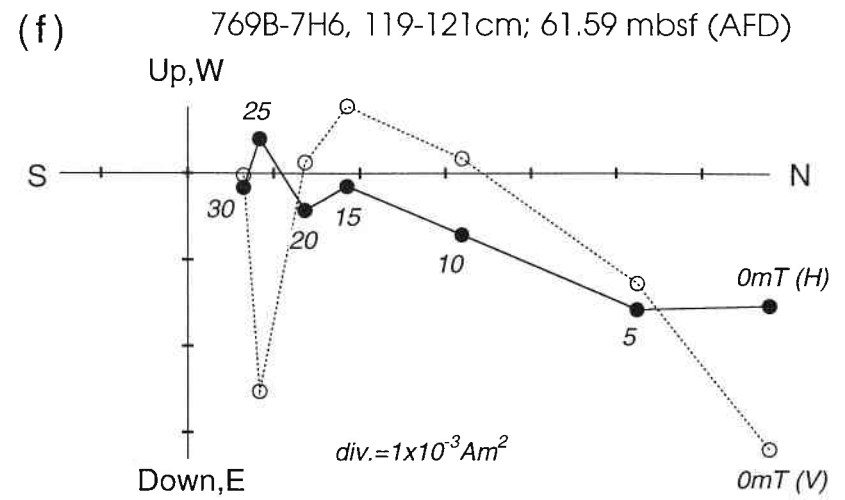
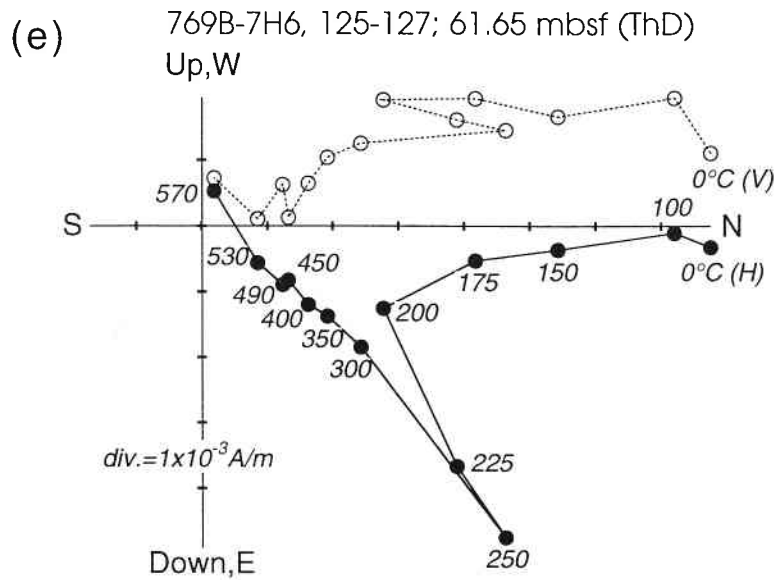


Fig. 19. (continued)

4.3.3. Hole 768B

The records from Section 768B-9H4 is thought to have recorded a short reversal precursor to the Brunhes/Matuyama transition, which may be correlated with the record from other area (e.g. Okada and Niitsuma, 1989). This short reversal can also be recognized in the declination records of Holes 769A and 769B (Fig. 20). It is not clearly be seen in the record of Hole 767B, however, this may correspond to the fluctuation in the directional record below 49.6 mbsf (Fig. 12). The length of the normal polarity short reversal is 40 cm (Fig. 21; 75.70-76.10 mbsf) and the duration is 4000 yr assuming constant sedimentation rate of 9.8 cm/kyr. The swing of declination at the top of the Section (75.03 mbsf) may be the last swing of the Brunhes/Matuyama transition (Fig. 21). However, the upper most part may be slightly affected by the unstable character of deconvolution near the end. From the termination of the short reversal to the beginning of the Brunhes/Matuyama is 67 cm and can be estimated to be 7000 yr for maximum sedimentation rate of 9.8 cm/kyr and 16 kyr for minimum sedimentation rate of 4.2 cm/kyr. The same interval both for Holes 769A and 769B is about 120 cm, and the timing is 15 kyr before the last swing of Brunhes/Matuyama for sedimentation rate of 8.0 cm/kyr at this site, which is close to the value calculated for 768B using the minimum sedimentation rate.

During the short normal reversal, magnetization intensity is relatively low (about 4×10^{-3} A/m), which is comparative to the low intensity zone of other Holes across the Brunhes/Matuyama boundary (Figs. 12, 15 and 16). Relative intensity normalized with the volume magnetic susceptibility is constantly low about 2, which is also comparative to the low of relative intensity around the Brunhes/Matuyama boundary obtained for other Holes (Figs. 12, 15 and 16) and increases to about 13 below 76.5 mbsf (Fig. 21). The VGPs are

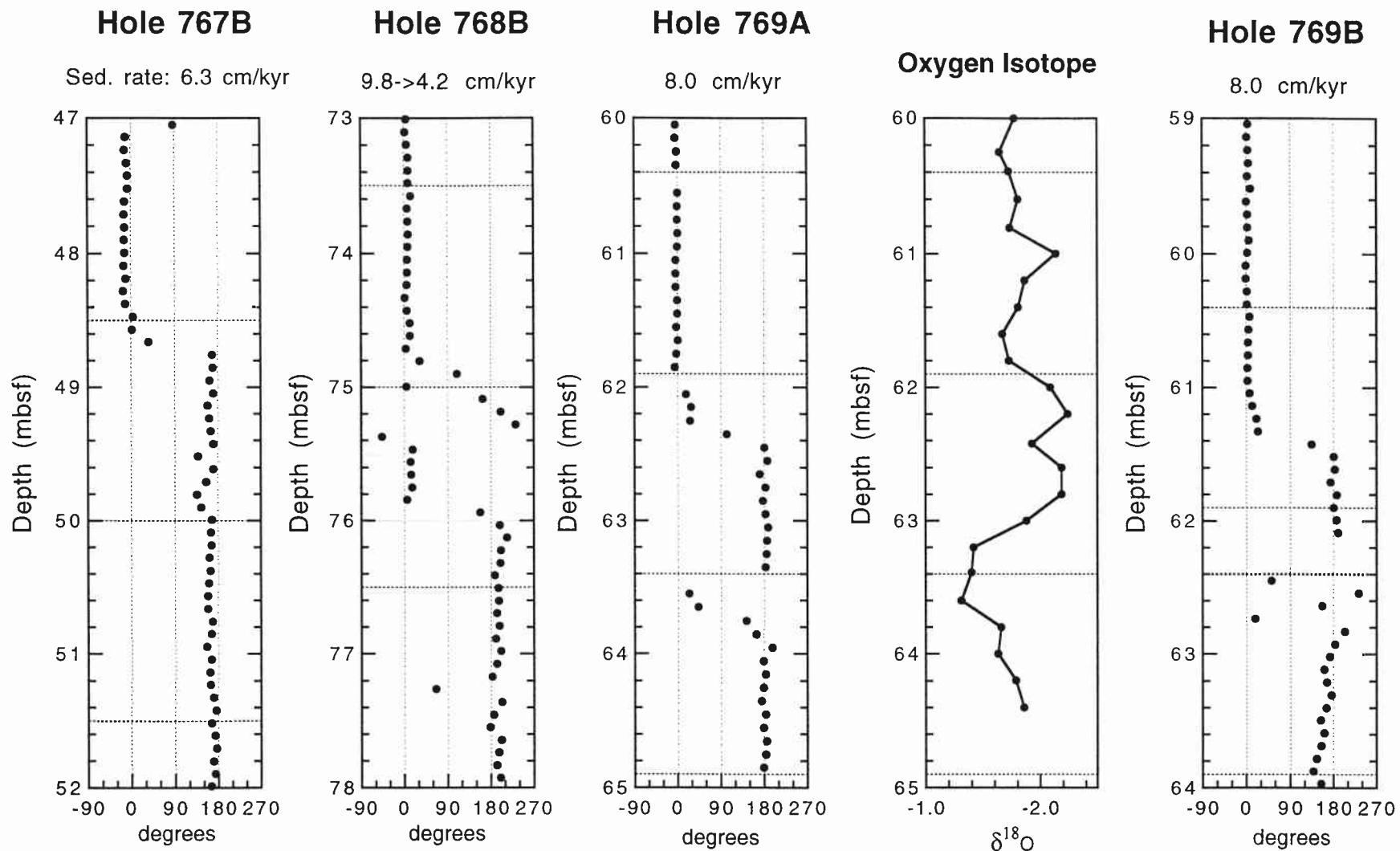


Fig. 20. Depth plot of declination for pass-through data of Holes 767B, 768B, 769A and 769B after 10mT AF demagnetization. For Hole 769B below 62.4mbsf, paleomagnetic results of 15mT were used. Horizontal thick dotted line and thin dotted lines show breaks of Core and Sections, respectively. Note the short reversal below the Brunhes/Matuyama boundary recognizable in Holes 768B, 769A and 769B. Oxygen isotope record from Hole 769A by Linsley and von Breyman (1991) are also shown.

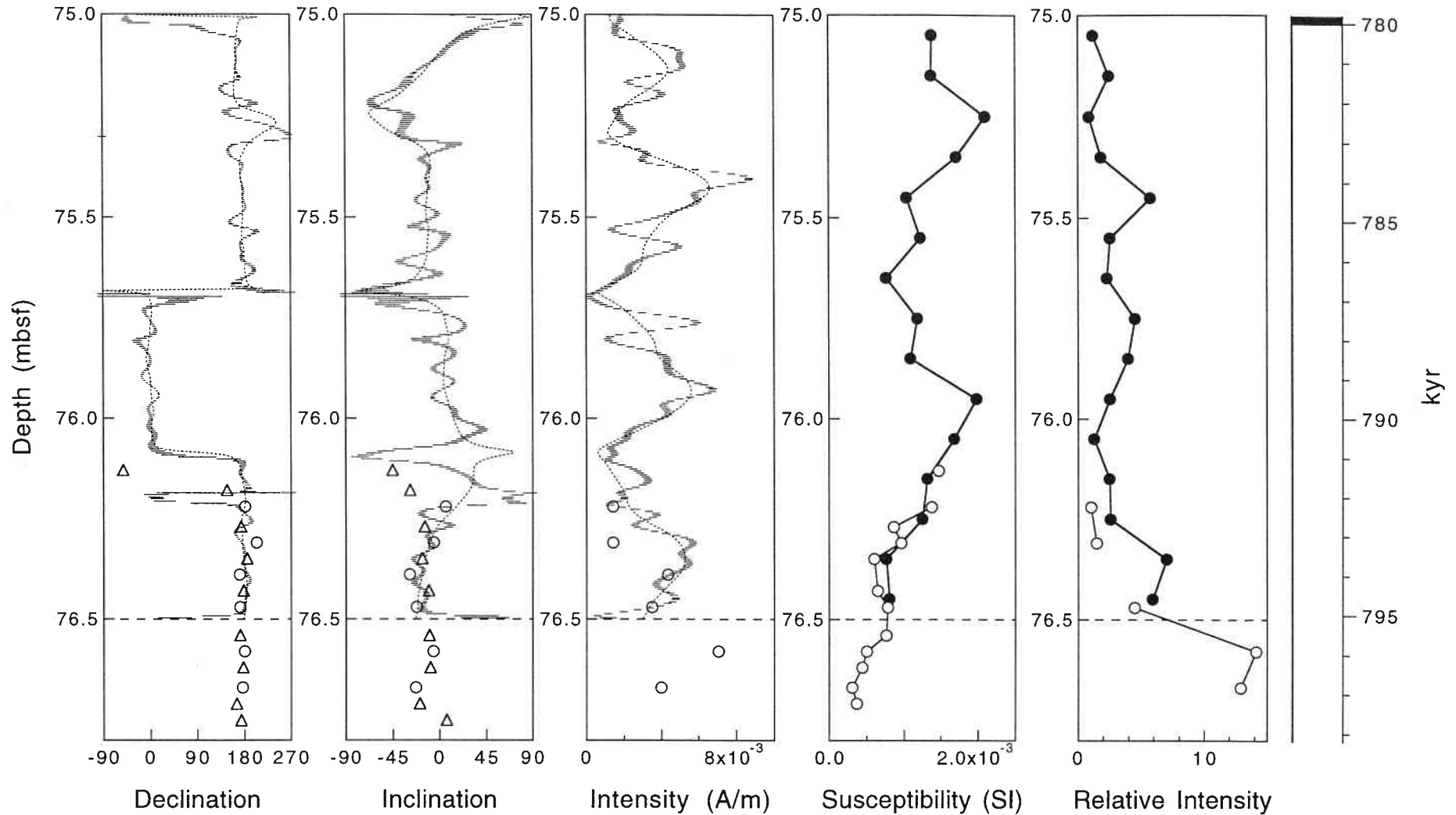


Fig. 21. Paleomagnetic results of a short reversal precursor to Brunhes/Matuyama polarity transition for Hole 768B (768B-9H4 and 768B-9H5) are shown. Horizontal broken lines represent the boundary of the sections. Brunhes/Matuyama boundary is assumed to be at the top of the Section. Declination, inclination, intensity, susceptibility and relative intensity are plotted versus depth with a time scale estimated by assuming constant sedimentation rate of 9.8 cm/kyr. Captions are same as in Fig. 12.

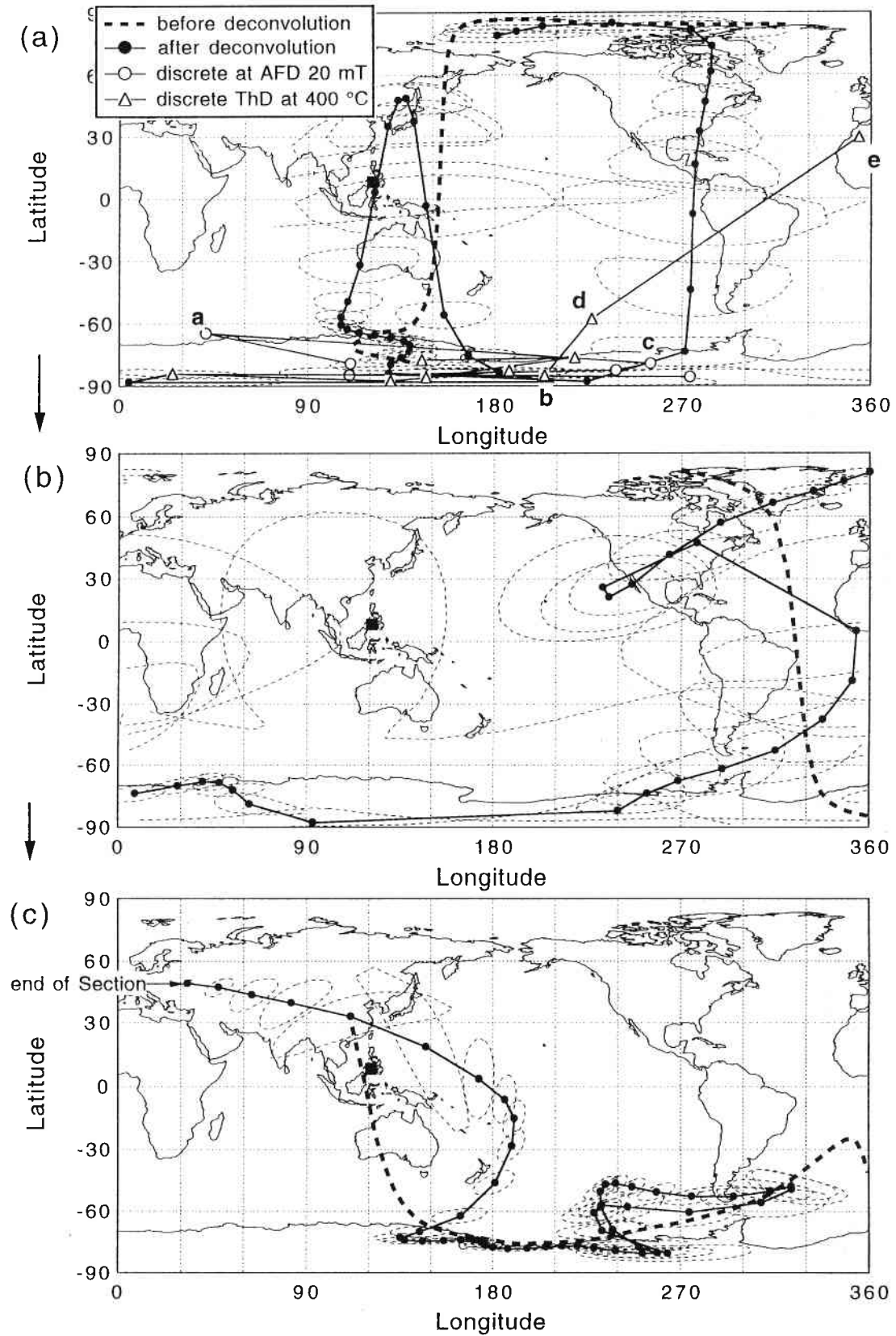
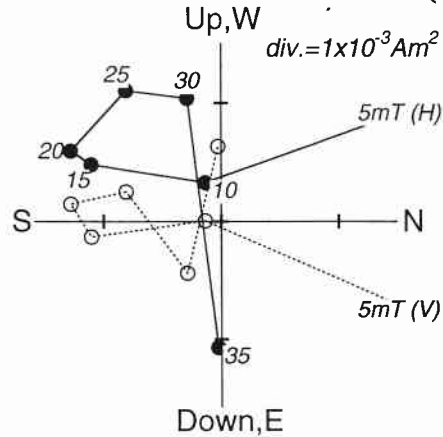


Fig. 22. VGP paths from Hole 768B are plotted for (a) onset and (b) termination of the short reversal, and (c) near the end of the core (possibly around Brunhes/Matuyama boundary). Location of the site is indicated by solid rectangles. Thick broken line show the VGP path for the pass-through data before deconvolution. Solid lines with small solid circles represent the VGP path for pass-through data after deconvolution with thin broken lines of 95% confidence ovals. Open circles and open triangles represent VGPs of cube samples after 20 mT AF demagnetization and thermal demagnetization of 400°C. Bold alphabets from a to e represent cube samples showing transitional directions.

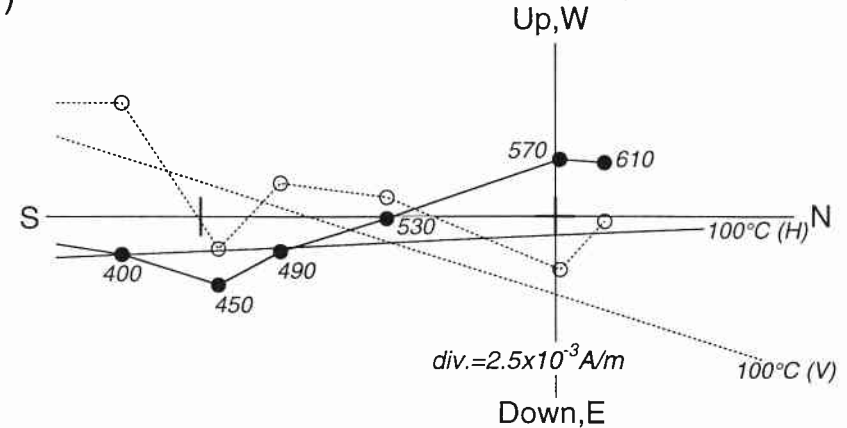
plotted according to the three phases of polarity change recognized in the record (Fig. 22). First is a very rapid swing over Australia and east Asia (Fig. 22a), of which duration is about 500 years assuming constant sedimentation rate of 9.8 cm/kyr. Second is reversed to normal polarity change over America (Fig. 22a), and the duration is very short of about 300 yr. Third is normal to reversed polarity change over America (Fig. 22b).

Discrete samples were not collected within the short reversal of normal polarity. Samples below the first phase of the normal polarity (Fig. 23a, b) and around the first phase (Fig. 23c, d) does not show normal polarity. Sample "e" between the first phase and the second phase slightly show an indication of remanent magnetization of normal polarity above 400°C (Fig. 23e).

(a) 768B-9H4, 131-133cm; 76.31 mbsf (AFD)

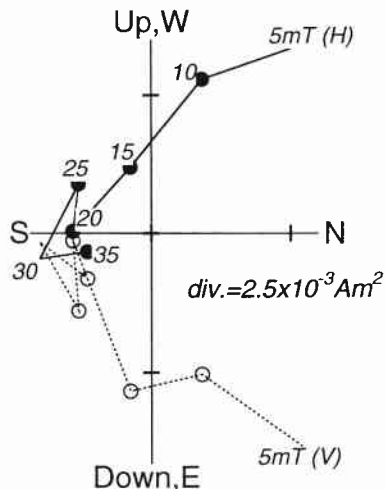


(b) 768B-9H4, 127-129cm; 76.27 mbsf (ThD)



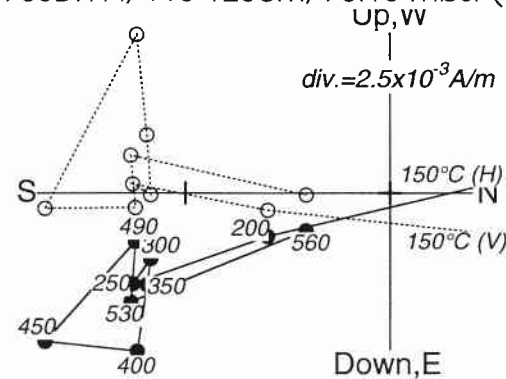
(c)

768B-9H4, 122-124; 76.22 mbsf (AFD)



(d)

768B9H4, 118-120cm; 76.18 mbsf (ThD)



(e)

768B-9H4, 113-115cm; 76.13 mbsf (ThD)

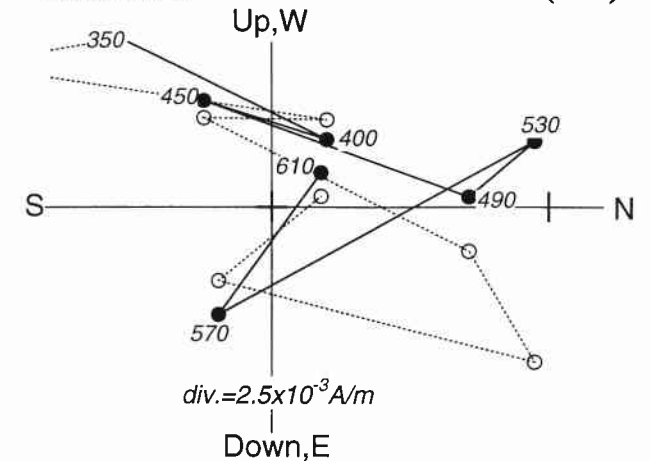


Fig. 23. Vector endpoint diagrams of progressive demagnetization experiments for cube samples from onset of the short reversal for Hole 768B. Alphabets a~e on Fig. 17 correspond to (a)~(e). Samples a and c were AF demagnetized and samples b, d and e were subjected to thermal demagnetization experiments.

5. Discussions

5.1. VGP paths of Brunhes/Matuyama polarity transition

The VGP paths of the Brunhes/Matuyama polarity transition obtained from Holes 767B, 769A and 769B are plotted on Fig. 24. The VGPs of Brunhes/Matuyama from Holes 769A (dotted line) and 769B (broken line) show excellent agreement with each other. Although the VGP paths for Hole 767B (solid line) is less stable, it seems to be in rough agreement with the results of Holes 769A and 769B. There are several important aspects of the transitional VGPs.

The first feature is the two cusps or small loops recognized over south of New Zealand, and central to south Pacific. These two intermediate VGP position obtained by deconvolution of pass-through data were confirmed by discrete samples of Hole 769B both by ThD (Fig. 19a, c) and AFD experiments (Fig. 19b, d). Although the behavior against stepwise demagnetization is not so stable, the agreement between the magnetization by deconvolution of pass-through data from the archive half and discrete sample from working half of Hole 769B, and between the magnetization of Hole 769A and 769B, strongly support that the true geomagnetic feature is recorded in the sediment. The records from Hole 767B is less stable and the error angle after deconvolution is quite large (up to 30°), however, the initial swing to Africa may correspond to the first cusp (loop) of the VGPs from Site 769.

The second remarkable feature is a large eastward swing from central-southern Pacific to northern Atlantic touching Green Land to Alaska found for the records from Holes 769A and 769B. It has been claimed that the transitional VGPs can be explained by a smoothing effect of intermediate directions just before and after the polarity reversal (Langereis et al., 1992; Rochette, 1990; Weeks et al., 1992; Quidelleur and Valet, 1994). However, it is quite difficult to produce this kind of large eastward swing by a smoothing artifact. Thus this

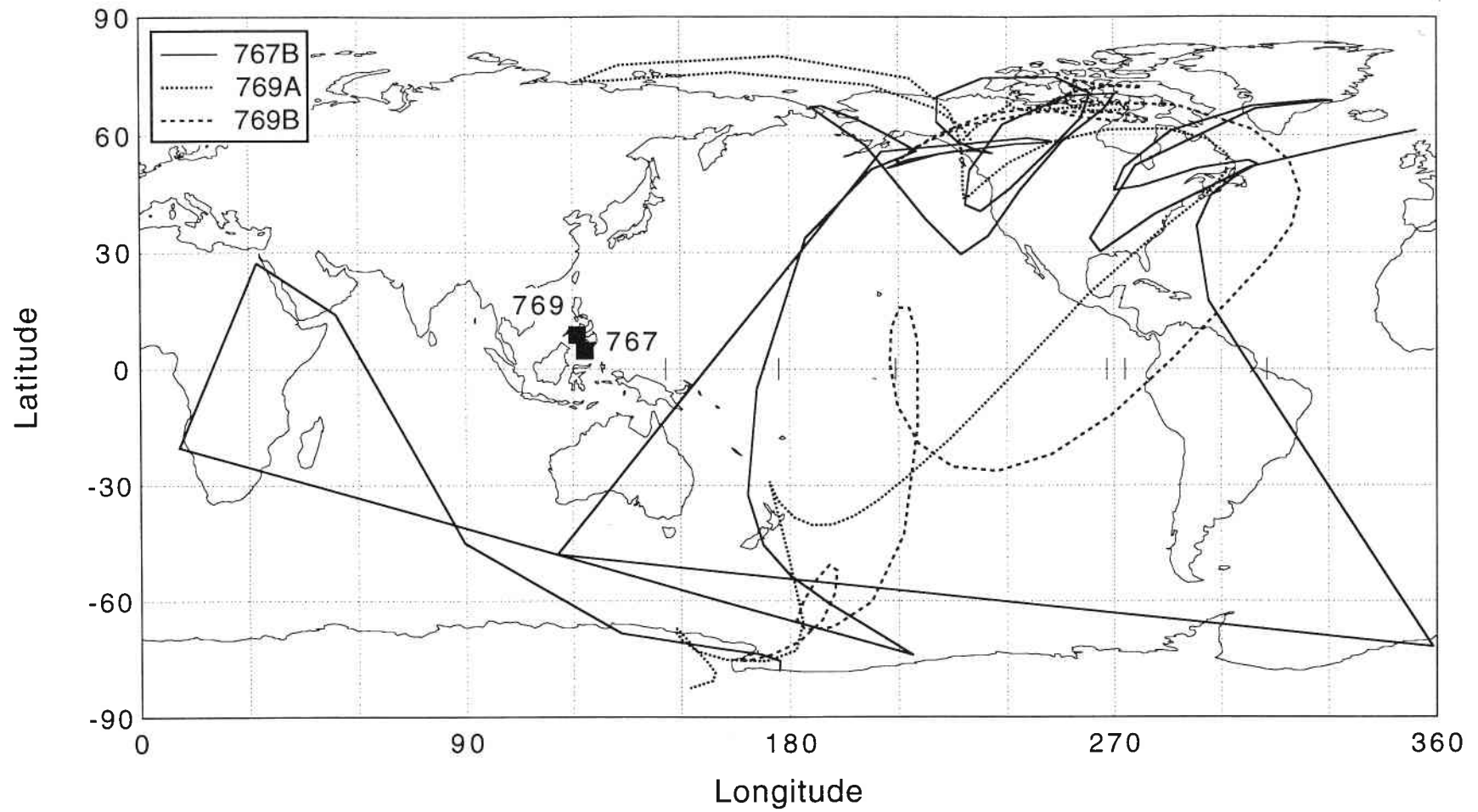


Fig. 24. VGP paths of Brunhes/Matuyama polarity transition for Sites 767 and 769 obtained in this study. Solid line, dotted line and broken line represent VGP paths for Hole 767B, 769A and 769B, respectively.

large eastward swing can be understood as a real geomagnetic feature possibly caused by a drifting non-dipole field during absence of the main dipole field. Even this feature can be smoothed by sediment and resolution limit of deconvolution, and real geomagnetic feature may be more complicated. The reason that this geomagnetic feature is not clearly recognized in the record of Hole 767B may be understood as the instability of sediment magnetization, because the sediment environment of the Celebes Sea (Site 767) is different from the Sulu Sea (Rangin and Silver, 1990).

The third important feature of the VGPs is that the polarity reversal is followed by a steady state of high northern latitude (50-70°N) around Alaska to north Canada for about 2000-3000 yr. It may be quite difficult to think that the rapidly changing transitional field is locked-in by an unrecognized turbidite effect to produce an intermediate direction, because the record from two different basins show the same character.

The transitional VGPs from Boso Peninsula is one of the most detailed record of Brunhes/Matuyama boundary (Niitsuma, 1971; Okada and Niitsuma, 1989). Okada and Niitsuma (1989) obtained the Brunhes/Matuyama transition records from the three sections of Boso Peninsula (Fig. 25) and reported that the main phase of the Brunhes/Matuyama transition is preceded by two short reversals at about 500 yr (A') lasting 40 yr and at 1600 yr lasting about 300 yr before the last swing of VGP at the transition. Besides, they recognized three stages for the transitional VGPs of the Brunhes/Matuyama transition. The first stage (D) is the clustering of VGPs between Australia and Antarctica (40-70°S) after the short reversal of A' and the last swing of Brunhes/Matuyama lasting 500 yr. The second (B) is the clustering at high northern latitude (50-70°N) around Siberia lasting 130 yr. The VGPs finally settle close to the north directing

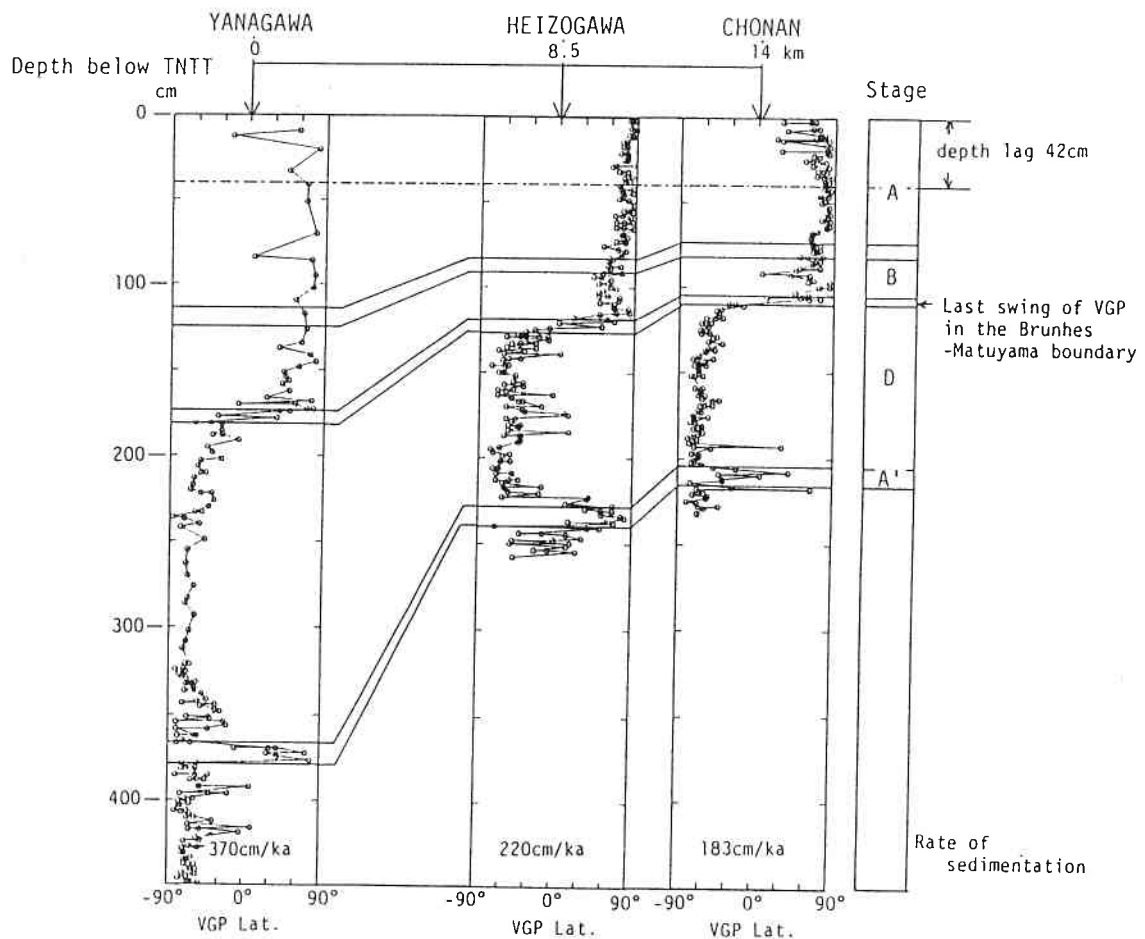


Fig. 25. VGP latitude records of the Brunhes/Matuyama polarity transition from three river sections of Boso Peninsula (Yanagawa, Heizogawa and Chonan). The top of the figure is adjusted to the TNTT horizon (vaocanic ash layer). The horizontal axis represents the distance between the three sites in km and the vertical axis show depths in cm below TNTT in the three sections. Redrawn from Okada and Niitsuma (1989).

axial dipole position (A).

The VGPs positions of this study and those from Boso Peninsula can be correlated with each other; Short reversal A' from Boso Peninsula to segment 1 of this study, stage D of Boso Peninsula to segment 2 of this study, and stage B from Boso Peninsula to segment 4 of this study. However, there is a discrepancy between the VGP longitude of equator crossing from Boso Peninsula (nearly same as the longitude of Boso Peninsula) and this study (central Pacific).

Durations of the polarity transition are also calculated for the Brunhes/Matuyama transition from the directional data by adopting VGPs between latitude of $\pm 45^\circ$ or $\pm 60^\circ$ as transitional (Table 6). The duration for the Brunhes/Matuyama is calculated as 1000 yr in average. Considering the smoothing effect of sediment, the true geomagnetic field may be more rapid. Coe and Prévot (1989) suggested the possibility of extremely rapid field variation (3° per day) during geomagnetic reversals from the Steens Mountain record. It is possible that the field variation during geomagnetic reversal when the main dipole field is absent may be very rapid reflecting instability at the top of the outer core.

Table 6. List of durations calculated for Brunhes/Matuyama polarity transition of Holes 767B, 769A and 769B. Durations were calculated from transition length by assuming constant sedimentation rates. Transition lengths were measured by VGPs between $\pm 45^\circ$ and between $\pm 60^\circ$ of latitude.

Hole	Transition length (cm)		Sedimentation rate (cm/kyr)	Duration (kyr)	
	$\pm 45^\circ$	$\pm 60^\circ$		min.	max.
767B	5	7.5	6.3	0.8	1.2
769A	7	9	8.0	0.9	1.1
769B	8	9	8.0	1.0	1.1

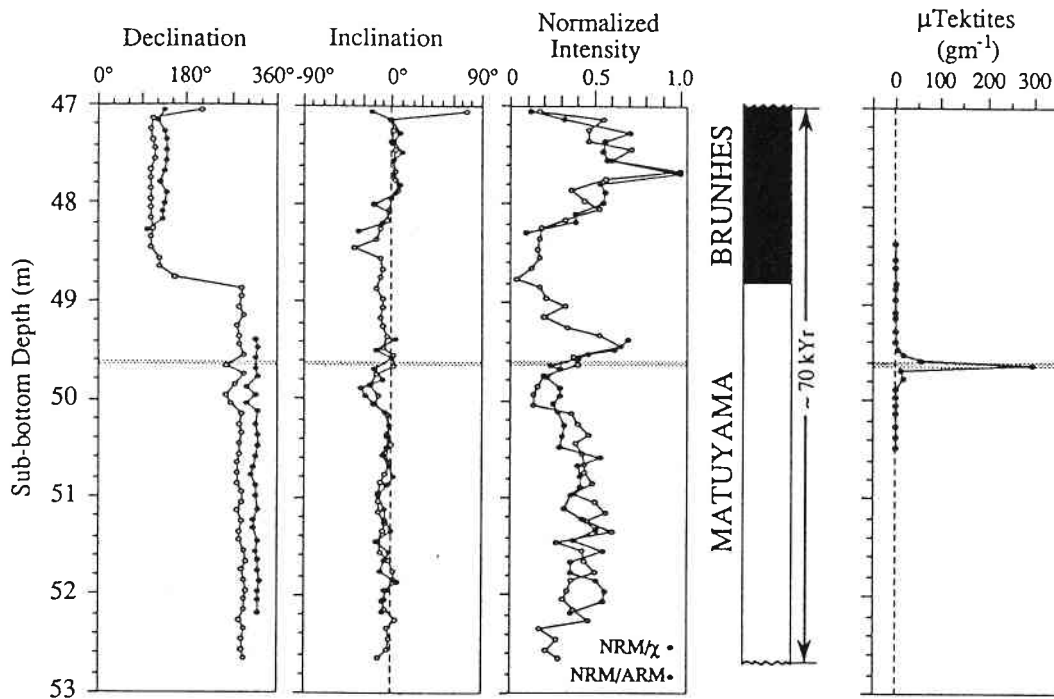
5.2. Short reversal

The results from Hole 768B show the short reversal precursor to the main phase of the Brunhes/Matuyama transition. The same short reversal can be recognized in the pass-through record of 769A (63.5-65.7 mbsf) and 769B (63.6-63.8 mbsf). Schneider et al. (1992) also measured paleomagnetic cube samples from Hole 767B and 769A (Fig. 26). Their results for Hole 769A (Fig. 26b) support the existence of the short reversal, however, there is only a slight deflection in declination and inclination at around 50 mbsf for Hole 767B (Fig. 26a). They also reported micro tektite layer with 200-300 counts per gram for Holes 767B (Fig. 26a; 49.63 mbsf) and 769A (Fig. 26b; 63.31 mbsf). This layer can be used as a stratigraphic marker. The micro tektite layer of Hole 769A is about 20 cm above the short reversal and the corresponding time interval should be 2500 yr assuming constant sedimentation rate. The corresponding depth interval for Hole 767B is 16 cm and the short reversal should be around 49.8 cm. The directional data of deconvolution show large fluctuation, which may be an indication of mixing of the short reversal by bioturbation.

At Hole 769A the termination of the short reversal is 120 cm below the last swing of Brunhes/Matuyama and the time interval can be calculated as 15 kyr assuming constant sedimentation rate of 8.0 cm/kyr. The time interval between termination of the short reversal and the last swing of Brunhes/Matuyama boundary of this study significantly differ from that for the Boso Peninsula by Okada and Niitsuma (1989). Oxygen isotope record was obtained for Hole 769A by Linsley and von Breyman (1991) , and the short reversal correspond to the oxygen isotope stage 20 (Fig. 20).

(a)

ODP 767B



(b)

ODP 769A

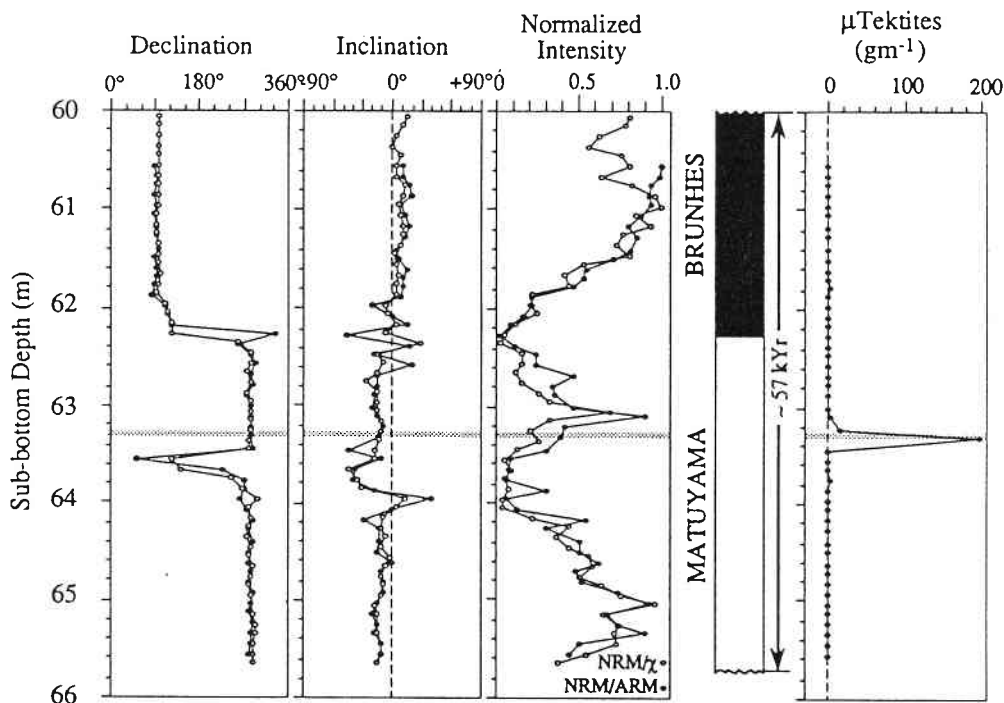


Fig. 26. Paleomagnetic results and microtektite layers identified from Holes 767B (a) and 769A (b). Solid points indicate results from discrete samples and open points indicate results of pass-through measurements after AFD at 10 mT at intervals of 10 cm. Discrete sample directions are determined by fitting progressive alternating field demagnetization trajectories. Declinations are given with respect to the double fiducial line on the working half sections. Intensity is normalized by ARM magnetization (for discrete measurements) and by low-field susceptibility (for continuous measurements). Microtektite abundance data reflect the number of microtektites in the $> 125 \mu\text{m}$ size fraction picked. Redrawn from Schneider et al. (1992).

5.3. Test for the preferred longitudinal bands

Preferred longitudinal distribution over America, and east Asia and western Australia are proposed for transitional VGPs by Laj et al. (1991). To test their hypothesis, longitudinal distribution of VGPs of Brunhes/Matuyama record was calculated for the transitional VGPs obtained in this study .

Equator crossings (EC) are used by Laj et al. (1991) to measure the transitional VGPs as a representative value of longitudinal distribution. The ECs are calculated as a simple average of longitude of VGPs lying latitude between $\pm 60^\circ$. Valet et al. (1992) proposed alternative way to represent the longitude of transitional VGPs by the mean value of longitude (MVL). They thought that each VGP_i should be weighted by the cosine of its latitude ($\cos \lambda_i$). This is achieved by projecting the unit directional vector (x_i, y_i, z_i) associated with every VGP position on the equatorial plane as

$$\text{MVL} = \tan^{-1} \left(\frac{\sum_{i=1}^n y_i}{\sum_{i=1}^n x_i} \right), \quad \delta = \cos^{-1} \left(\frac{R}{\sum_{i=1}^n \cos \lambda_i} \right)$$

$$\text{where } R = \sqrt{\left(\sum_{i=1}^n x_i \right)^2 + \left(\sum_{i=1}^n y_i \right)^2}$$

Mean value of longitude with weight of its error (WMVL) were also calculated. These values calculated for the transitional VGPs of 767B, 769A and 769B are listed in Table. 7. The average value of EC, MVL and WMVL are 210° , 210° and 231° . The preferred longitudinal bands of transitional VGPs calculated by McFadden et al. (1993) using 60° rotating sectors are $266^\circ\text{E}-325^\circ\text{E}$ and $86^\circ\text{E}-145^\circ\text{E}$. The longitude representative of the transitional VGPs of Celebes and Sulu Seas is

Table 7. Results of calculation representative of longitudinal distribution of transitional VGPs. ECs (equator crossings) are calculated by simply averaging longitude within transition zones. MVLs (mean value of longitude) were calculated by averaging vectors of transitional VGPs projected on an equatorial plane (See text). Weighted version of MVLs were also calculated with weight by error of each data point.

Hole	Number of VGPs	EC	MVL	MVL(weighted)
767B	16	157°±67°	170°±64°	207°±61°
769A	19	224°±48°	217°±45°	225°±48°
769B	19	250°±44°	244°±42°	261°±52°
average		210°	210°	231°

outside the preferred bands of transitional VGPs.

McFadden et al. (1993) calculated the preferred bands for the sites recording transitional VGPs as 26°W-33°E and 147°W-154°E. They conducted statistical tests according to the independence of preferred longitudinal bands and preferred longitudinal distribution of the sites. Their conclusion is that the VGPs are likely to distribute $\pm 90^\circ$ away from the site and that the data obtained from sites that fall well outside the preferred site bands are strongly needed. The longitude of Sites 767 and 769 is about 120°E and the angle between EC and site longitude can be calculated as about 90°. This may support the distribution of VGPs $\pm 90^\circ$ away from the sites suggested by McFadden et al. (1993). They proposed possible mechanism for this distribution as nonlinearity of the VGP transformation or increased inclination errors in sediments at low field intensity.

5.4. Relative intensity

Relative intensity was calculated for the pass-through data after deconvolution of Holes 767B, 769A and 769B by normalizing with the volume magnetic susceptibility (Fig. 27). The relative intensity for the three holes show quite similar pattern. At the Brunhes/Matuyama boundary the relative intensity show very small value of about 0.5 for all the Holes. The zone of low relative intensity (less than 2) was recognized lasting about 4000 yr between 778 ka and 782 ka. The relative intensity outside the low intensity zone is relatively stable with values between 2-5. This middle intensity zone continue for 17 kyr between 771 ka and 788 ka including low intensity zone mentioned above. The relative intensity increases further outside the middle intensity zone with peak values at around 763 ka and 791 ka.

The time scale was determined by assuming the constant sediment accumulation rate of 6.3 cm/kyr (767B) and 8.0 cm/kyr (769A and 769B), because the sedimentation rate for these Holes are almost constant from present to upper Jaramillo polarity transition (Fig. 3). The constant sedimentation rate can be supported by the Australasian micro tektite layer reported by Schneider et al. (1992) from Hole 767B and 769A (Fig. 26). The layers of micro tektite are at 49.63 mbsf for Hole 767B and 63.31 mbsf for Hole 769A. The Brunhes/Matuyama boundaries obtained for this study are at 48.71 mbsf for Hole 767B and 62.25 mbsf for Hole 769A. The depth intervals are 92 cm and 106 cm for Holes 767B and 769A. The corresponding time interval for Holes 767B and 769A are 14.6 kyr and 13.3 kyr assuming constant sedimentation rate. As the difference is not so large, the sedimentation rate values of 6.3 cm/kyr and 8.0 cm/kyr adopted for Holes 767B, and 769A and 769B are appropriate.

The relative intensity record obtained from Holes 767B, 769A and 769B show quite similar pattern. Schneider et al. (1992) also measured

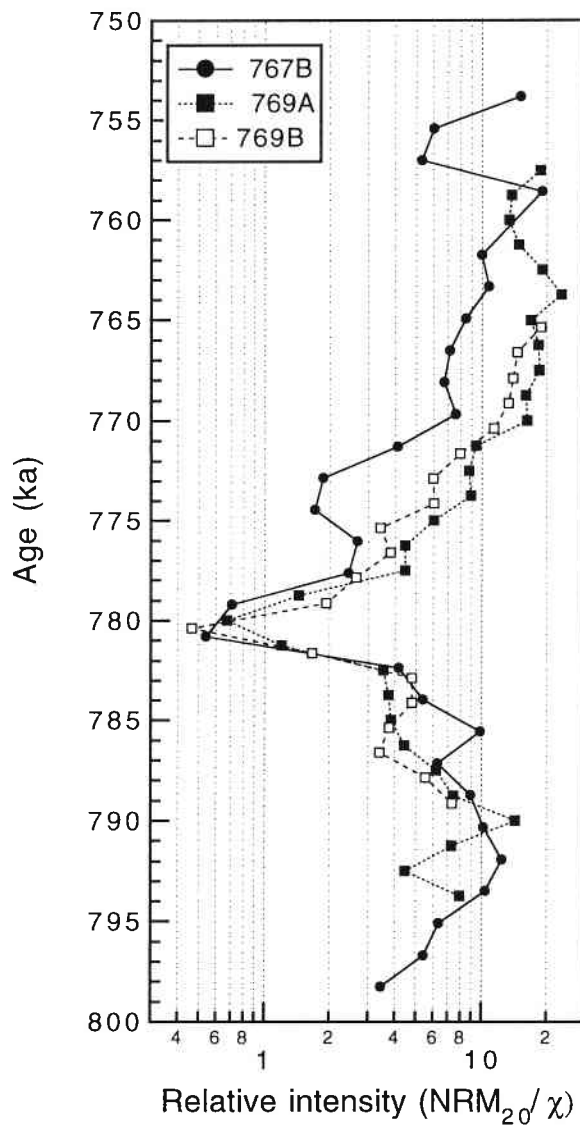


Fig. 27. Relative paleointensities for Holes 767B, 769A and 769B are plotted versus age. Relative intensities were calculated by dividing the intensity of magnetization after deconvolution (AFD at 20 mT) by susceptibility. Ages are calculated by assuming the age of Brunhes/Matuyama boundary as 780 ka and constant sedimentation rate of 6.3 cm for Hole 767B, and 8.0 cm/kyr for Holes 769A and 769B.

paleomagnetic results from Holes 767B and 769A, and obtained the relative intensity normalized both by volume magnetic susceptibility and ARM of the samples. Their results for susceptibility-normalized and ARM-normalized relative intensity show quite similar pattern in large scale (Fig. 28). These two records seems to show negative correlation in smaller scale of about 2500 yr (~ 20 cm). Thus the longer term change as low and middle intensity zone can be considered as a real geomagnetic change.

The low intensity zone is also recognized in the record of Boso Peninsula lasting 5400 yr showing reduction in intensity to about 40% of outside the transition zone (Okada and Niitsuma, 1989). The duration of low intensity zone identified in this study and from Boso Peninsula agree very well with each other.

Valet et al. (1994) obtained relative paleointensity across the Brunhes/Matuyama transition from sediments of Atlantic, Indian and Pacific Oceans. They calculated relative paleointensity by normalizing the magnetization intensity by ARM and susceptibility. Their results from three deep-sea sediment also show reduced intensity between 770 ka and 790 ka with several minor fluctuation inside. This may be correlated to the zone of middle intensity of this study.

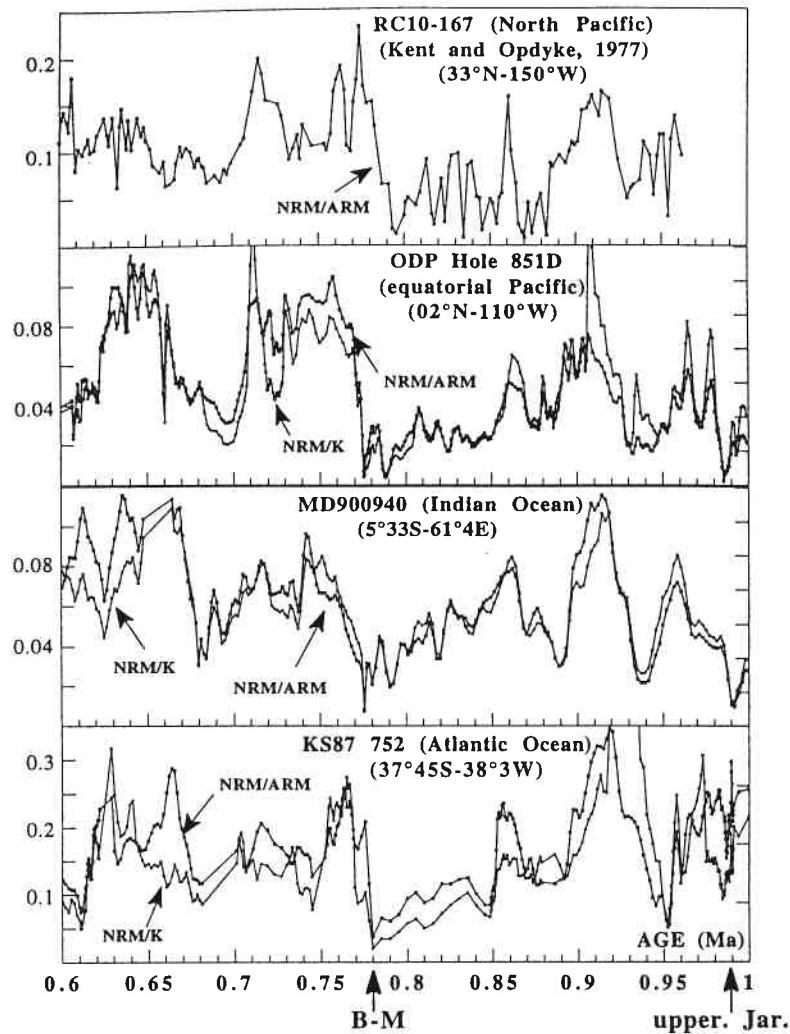


Fig. 28. Variations of relative paleointensities versus age in ODP Hole 851D, and in Cores KS752 and MD900940 across the Brunhes/Matuyama boundary. Relative paleointensities were obtained by normalizing NRM (natural remanent magnetization) both by ARM (anhysteretic remanent magnetization) and K (susceptibility). Core RC10-167 obtained from discrete samples were also shown for comparison. Ages are constrained by Brunhes/Matuyama and upper Jaramillo transition. Note the reduction in relative intensity at the Brunhes/Matuyama boundary to about 20-25 % of the intensity before and after the transition. Redrawn from Valet et al. (1994).

6. Conclusions

High resolution Brunhes/Matuyama transition records were obtained from Holes 767B, 769A and 769B of ODP Leg 124. Several important results were obtained about the detailed structure of Brunhes/Matuyama polarity transition.

The record of Holes 769A and 769B indicate the presence of two cusps of VGPs around south of New Zealand and central-south Pacific prior to the equatorial crossing of VGPs. The record of 769A and 769B show eastward swing of VGPs just after the equator crossing. The records of Holes 767B, 769A and 769B all show steady state of high northern latitude (50-70°N) around Alaska to north Canada for about 2000-3000 yr after the polarity transition. The intermediate directions are comparative to the stage "B" of Okada and Niitsuma (1989) after the last swing of Brunhes/Matuyama transition recorded in the sediments of Boso Peninsula.

Duration of Brunhes/Matuyama polarity reversal calculated from the directional change is very short about 1000 yr.

The average longitude of transitional VGPs were also calculated to test the preferred longitudinal bands. The average VGP longitude (MVL) value of 210° and the site location outside the preferred site band enforces the distribution of VGPs $\pm 90^\circ$ away from the sites.

Relative paleointensity across the Brunhes/Matuyama transition was also calculated. The results shows that the low intensity zone persisted for about 4000 yr during the reversal. This is very consistent with the duration of low intensity zone (5400 yr) calculated for the reversal record from Boso Peninsula (Okada and Niitsuma, 1989).

References

- Baksi, A. K., Concordant sea-floor spreading rates obtained from geochronology, astrochronology and space geodesy, *Geophys. Res. Lett.*, **21**, 133-136, 1994.
- Baksi, A. K., V. Hsu, M. O. McWilliams and E. Farrar, $^{40}\text{Ar}/^{39}\text{Ar}$ dating of the Brunhes-Matuyama geomagnetic field reversal, *Science*, **256**, 356-357, 1992.
- Berger, W. H., M. K. Yasuda, T. Bichert, G. Wefer and T. Takayama, Quaternary time scale for the Ontong Java Plateau: Milankovitch template for Ocean Drilling Program Site 806, *Geology*, **22**, 463-467, 1994.
- Berggren, W. A., D. V. Kent, J. J. Flynn and J. A. van Couvering, Cenozoic geochronology, *Bull. Geol. Soc. Am.*, **96**, 1407-1418, 1985.
- Bogue, S. W. and R. S. Coe, Successive paleomagnetic reversal records from Kauai, *Nature*, **295**, 399-401, 1982.
- Bogue, S. W. and R. S. Coe, Transitional paleointensities from Kauai, Hawaii, and geomagnetic reversal models, *J. Geophys. Res.*, **89**, 10341-10354, 1984.
- Brown, L., J. Pickens and B. Singer, Matuyama-Brunhes transition recorded in lave flows of the Chilean Andes: Evidence for dipolar fields during reversals, *Geology*, **22**, 299-302, 1994.
- Cande, S. C. and D. V. Kent, A new geomagnetic polarity time scale for the late Cretaceous and Cenozoic, *J. Geophys. Res.*, **97**, 13917-13952, 1992.
- Chauvin, A., P. Roperch and R. A. Duncan, Records of geomagnetic reversals from volcanic Islands of French Polynesia. 2. Paleomagnetic study of a flow sequence (1.2-0.6 Ma) from the island of Tahiti and discussion of reversal models, *J. Geophys. Res.*, **95**, 2727-2752, 1990.
- Clement, B. M., Geographical distribution of transitional VGPs : evidence

- for non-zonal equatorial symmetry during the Matuyama-Brunhes geomagnetic reversal, *Earth Planet. Sci. Lett.*, **104**, 48-58, 1991.
- Clement, B. M. and D. V. Kent, A detailed record of the lower Jaramillo polarity transition from a southern hemisphere, deep-sea sediment core, *J. Geophys. Res.*, **89**, 1049-1058, 1984.
- Clement, B. M. and D. V. Kent, Geomagnetic polarity transition records from five hydraulic piston core sites in the North Atlantic, *Init. Rep. DSDP*, **94**, 831-852, 1986.
- Clement, B. M. and D. V. Kent, A southern hemisphere record of the Matuyama-Brunhes polarity reversal, *Geophys. Res. Lett.*, **18**, 81-84, 1991.
- Clement, B. M., D. V. Kent and N. D. Opdyke, Brunhes-Matuyama polarity transition in three deep-sea sediment cores, *Phil. Trans. R. Soc. Lond.*, **A306**, 113-119, 1982.
- Coe, R. S. and M. Prévot, Evidence suggesting extremely rapid field variation during a geomagnetic reversal, *Earth Planet. Sci. Lett.*, **92**, 292-298, 1989.
- Dagley, P. and E. Lawley, Paleomagnetic evidence for the transitional behavior of the geomagnetic field, *Geophys. J. R. astron. Soc.*, **36**, 577-598, 1974.
- deMenocal, P. B., W. F. Ruddiman and D. V. Kent, Depth of post-depositional remanence acquisition in deep-sea sediments: a case study of the Brunhes-Matuyama reversal and oxygen isotopic Stage 19.1, *Earth Planet. Sci. Lett.*, **99**, 1-13, 1990.
- DeMets, C., R. G. Gordon, D. F. Argus and S. Stein, Effect of recent revisions to the geomagnetic reversal time scale on estimates of current plate motions, *Geophys. Res. Lett.*, **21**, 2191-2194, 1994.
- Dodson, R., J. R. Dunn, M. Fuller, I. Williams, H. Ito, V. A. Schmidt and Y.-M. Wu, Palaeomagnetic record of a late Tertiary field reversal, *Geophys. J. R. astr. Soc.*, **53**, 373-412, 1978.

- Fuller, M., I. Williams and K. A. Hoffman, Paleomagnetic records of geomagnetic field reversals and the morphology of the transitional fields, *Rev. Geophys. Space Phys.*, 1979.
- Hammond, S. R., S. M. Seyb and F. Theyer, Geomagnetic polarity transitions in two oriented sediment cores from the northwest Pacific, *Earth Planet. Sci. Lett.*, **44**, 167-175, 1979.
- Harland, W. B., R. L. Armstrong, A. V. Cox, L. E. Craig, A. G. Smith and D. G. Smith, *A geologic time scale 1989*, Cambridge, England, Cambridge University Press, 1990.
- Hilgen, F. J., Astronomical calibration of Gauss to Matuyama sapropels in the Mediterranean and implication for the geomagnetic polarity time scale, *Earth Planet. Sci. Lett.*, **104**, 226-244, 1991.
- Hillhouse, J. and A. Cox, Brunhes-Matuyama polarity transition, *Earth Planet. Sci. Lett.*, **29**, 51-64, 1976.
- Hoffman, K. A., Quantitative description of the geomagnetic field during the Matuyama-Brunhes polarity transition, *Phys. Earth Planet. Int.*, **24**, 229-235, 1981.
- Hoffman, K., Long-lived transitional states of the geomagnetic field and the two dynamo families, *Nature*, **354**, 273-277, 1991.
- Hoffman, K., Dipolar reversal states of the geomagnetic field and core-mantle dynamics, *Nature*, **359**, 789-794, 1992.
- Hoffman, K. A., Polarity transition records and the geomagnetic dynamo, *Science*, **196**, 1329-1332, 1977.
- Izett, G. A. and J. D. Obradovich, $^{40}\text{Ar}/^{39}\text{Ar}$ age constraints for the Jaramillo normal subchron and the Matuyama-Brunhes geomagnetic boundary, *J. Geophys. Res.*, **99**, 2925-2934, 1994.
- Johnson, R. G., Brunhes-Matuyama magnetic reversal dated at 790,000 yr B.P. by marine-astronomical correlations, *Quaternary Research*, **17**, 135-147, 1982.
- Kawai, N. and Y. Otofujii, Paleomagnetic study of deep-sea sediments

- using thin sections, *J. Geomag. Geoelectr.*, **28**, 395-412, 1976.
- Laj, C., S. Guitton, C. Kissel, and A. Mazaud, Complex behavior of the geomagnetic field during three successive polarity reversals, 11-12 m.y. B.P., *J. Geophys. Res.*, **93**, 11655-11666, 1988.
- Laj, C., A. Mazaud, R. Weeks, M. Fuller and E. Herrero-Bervera, Geomagnetic reversal paths, *Nature*, **351**, 447, 1991.
- Laj, C., A. Mazaud, R. Weeks, M. Fuller and E. Herrero-Bervera, Geomagnetic reversal paths, *Nature*, **359**, 111-112, 1992a.
- Laj, C., A. Mazaud, R. Weeks, M. Fuller and E. Herrero-Bervera, Statistical assessment of the preferred longitudinal bands for recent geomagnetic reversal records, *Geophys. Res. Lett.*, **19**, 2003-2006, 1992b.
- Langereis, C. G., A. A. M. van Hoof and P. Rochette, Longitudinal confinement of geomagnetic reversal paths as a possible sedimentary artifact, *Nature*, **358**, 226-233, 1992.
- Linsley, B. K. and M. T. von Breyman, Stable isotopic and geochemical record in the Sulu Sea during the last 7500 k.y.: Assessment of surface water variability and paleoproductivity changes, in *Proc. ODP, Sci. Results.*, **124**, 379-396, ed. Silver, E. A., C. Rangin, M. T. von Breyman et al., Ocean Drilling Program, College Station, TX, 1991.
- Linssen, J. H., Preliminary results of a study of four successive sedimentary geomagnetic reversal records from the Mediterranean (upper Thvera, lower and upper Sidufjall, and Lower Nunivak), *Phys. Earth Planet. Inter.*, **52**, 207-231, 1988.
- Mankinen, E. A., M. Prévot, C.S. Gromme, and R.S. Coe, The Steens Mountain (Oregon) geomagnetic polarity transition : 1. Directional history, duration of episodes, and rock magnetism, *J. Geophys. Res.*, **90**, 10393-10416, 1985.
- Mankinen, E. A. and G. B. Dalrymple, Revised geomagnetic polarity time scale for the interval 0-5 m.y. B.P., *J. Geophys. Res.*, **84**, 615-626,

1979.

- McFadden, P. L., C. E. Barton and R. T. Merrill, Do virtual geomagnetic pole follow preferred paths during geomagnetic reversals?, *Nature*, **361**, 342-344, 1993.
- Moskowitz, B. M., Methods for estimating Curie temperatures of titanomaghemites from experimental Js-T data, *Earth Planet. Sci. Lett.*, **53**, 84-88, 1981.
- Niitsuma, N., Detailed study of the sediments recording the Matuyama-Brunhes geomagnetic reversal, *Tohoku Univ. Sci. Rept 2nd Ser. (Geology)*, **43**, 1-39, 1971.
- Nishitani, T. and M. Kono, Curie temperature and lattice constant of oxidized titanomagnetite, *Geophys. J. R. astr. Soc.*, **74**, 585-600, 1983.
- Obradovich, J. D. and G. A. Izett, The geomagnetic polarity time scale (GPTS) and the astronomical time scale (ATS) now in near accord, *EOS Trans. AGU*, **73** (43), 630-631, 1992.
- Okada, M. and N. Niitsuma, Detailed paleomagnetic records during the Brunhes-Matuyama geomagnetic reversal, and a direct determination of depth lag for magnetization in marine sediments, *Phys. Earth Planet. Inter.*, **56**, 133-150, 1989.
- Opdyke, N. D., D. V. Kent and W. Lowrie, Details of magnetic polarity transitions recorded in a high deposition rate deep-sea core, *Earth Planet. Sci. Lett.*, **20**, 315-324, 1973.
- Otofuji, Y., I. Katsura and S. Sasajima, Decay of a post-depositional remanent magnetization in wet sediments due to the effect of drying, *Geophys. J. R. astr. Soc.*, **70**, 191-203, 1982.
- Prévot, M. and P. Camps, Absence of preferred longitude sectors for poles from volcanic records of geomagnetic reversals, *Nature*, **366**, 53-56, 1993.
- Prévot, M., E. A. Mankinen, C. S. Gromme and R. S. Coe, How the

- geomagnetic field vector reverses polarity, *Nature*, **316**, 230-234, 1985.
- Quidelleur, X. and J.-P. Valet, Paleomagnetic records of excursions and reversals: possible biases caused by magnetization artefacts, *Phys. Earth Planet. Inter.*, **82**, 27-48, 1994.
- Rangin, C., E. A. Silver and M. T. von Breymann et. al., *Proc. ODP, Init. Repts.*, **124**, 1990.
- Rochette, P., Rationale of geomagnetic reversals versus remanence recording processes in rocks : a critical review, *Earth Planet. Sci. Lett.*, **98**, 33-39, 1990.
- Roperch, P., and R.A. Duncan, Records of geomagnetic reversals from volcanic Islands of French Polynesia. 1. Paleomagnetic study of a polarity transition in a lava sequence from the island of Huahine, *J. Geophys. Res.*, **95**, 2713-2726, 1990.
- Schneider, D. A., D. V. Kent and G. A. Mello, A detailed chronology of the Australasian impact event, the Brunhes-Matuyama geomagnetic polarity reversal, and global climate change, *Earth Planet. Sci. Lett.*, **111**, 395-405, 1992.
- Shackleton, N. J., A. Berger and W. R. Peltier, An alternative astronomical calibration of the lower Pleistocene timescale based on ODP Site 677, *Trans. Royal Soc. Edinburgh: Earth Sciences*, **81**, 251-261, 1990.
- Shaw, J., Strong geomagnetic fields during a single Icelandic polarity transition, *Geophys. J. R. astron. Soc.*, **40**, 345-350, 1975.
- Shyu, J.-P., D. Merrill, V. Hsu, M. A. Kaminski, C. M. Müller, A. J. Nederbragt, R. P. Scherer and H. Shibuya, Biostratigraphic and magnetostratigraphic synthesis of the Celebes and Sulu Seas, Leg 124, in *Proc. ODP, Sci. Results.*, **124**, 11-35, ed. Silver, E. A., C. Rangin and M. T. von Breymann et al., Ocean Drilling Program, College Station, TX, 1991.

- Spell, T. L. and I. McDougall, Revisions to the age of the Brunhes-Matuyama boundary and the Peistocene geomagnetic polarity timescale, *Geophys. Res. Lett.*, **19**, 1181-1184, 1992.
- Tauxe, L., A. D. Deino, A. K. Behrensmeyer and R. Potts, Pinning down the Brunhes/Matuyama and upper Jaramillo boundaries: a reconciliation of orbital and isotopic time scales, *Earth Planet. Sci. Lett.*, **109**, 561-572, 1992.
- Theyer, F., E. Herrero-Bervera and V. Hsu, The zonal harmonic model of polarity transitions : A test using successive reversals, *J. Geophys. Res.*, **90**, 1963-1982, 1985.
- Tric, E., C. Laj, C. Jehanno, J.-P. Valet, C. Kissel, A. Mazaud and S. Iaccarino, High-resolution record of the Upper Olduvai transition from Po Valley (Italy) sediments : support for dipolar transition geometry?, *Phys. Earth Planet. Inter.*, **65**, 319-336, 1991.
- Valet, J.-P., C. Laj, and P. Tucholka, High-resolution sedimentary record of a geomagnetic reversal, *Nature*, **322**, 27-32, 1986.
- Valet, J.-P., L. Tauxe, and B.M. Clement, Equatorial and mid-latitude records of the last geomagnetic reversal from the Atlantic Ocean, *Earth Planet. Sci. Lett.*, **94**, 371-384, 1989.
- Valet, J.-P., C. Laj and C. G. Langereis, Sequential geomagnetic reversals recorded in upper Tortonian marine clays in western Crete (Greece), *J. Geophys. Res.*, **93**, 1131-1151, 1988.
- Valet, J.-P., P. Tucholka, V. Courtillot and L. Meynadier, Paleomagnetic constraints on the geometry of the geomagnetic field during reversals, *Nature*, **356**, 400-407, 1992.
- Valet, J.-P., L. Meynadier, F. C. Bassinot and F. Garnier, Relative paleointensity across the last geomagnetic reversal from sediments of the Atlantic, Indian and Pacific Oceans, *Geophys. Res. Lett.*, **21**, 485-488, 1994.
- Weeks, R., M. Fuller, C. Laj, A. Mazaud and E. Herrero-Bervera,

Sedimentary records of reversal transitions - magnetization smoothing artifact of geomagnetic field behavior?, *Geophys. Res. Lett.*, **19**, 2007-2010, 1992.

Williams, I. and M. Fuller, Zonal harmonic models of reversal transition fields, *J. Geophys. Res.*, **86**, 11657-11665, 1981.

Williams, I., R. Weeks and M. Fuller, A model for transition fields during geomagnetic reversals, *Nature*, **332**, 719-720, 1988.